School of Electrical Engineering, Computing and Mathematical Sciences

Two-centre Convergent Close-Coupling Approach to Positron and Positronium Scattering

Charlie Michael Rawlins

This thesis is presented for the Degree of
Doctor of Philosophy
of
Curtin University

October 2018

Declaration

To the best of my knowledge and belief this thesis contains no material previously published by any other person except where due acknowledgment has been made.

This thesis contains no material which has been accepted for the award of any other degree or diploma in any university.

Signature 

Date 4.10.18

Contents

Summary

This thesis presents theoretical investigations of antihydrogen formation via positronium-antiproton collisions using the two-centre convergent close-coupling (CCC) method. It also presents the extension to the CCC method to positron scattering on charged targets, more specifically, the singly-charged helium ion.

The thesis is organised in the following way:

The Introduction (Chapter 1) covers the motivation for the study and the current status of the antihydrogen formation and positron-He^+ scattering problems. Other theoretical methods for positron and positronium scattering on charged targets are reviewed and their limitations are indicated. The application of the two-centre CCC method to positron scattering on a one-electron charged target is presented in Chapter 2. The derivations of the scattering equations and transition matrix elements are given in detail. The results of the two-centre CCC calculations for antihydrogen formation are compared to available experiment and results of other calculations in Chapter 3. The results of positron scattering on He^+ are compared with the results of other calculations in Chapter 4. Finally, in Chapter 5, we draw conclusions arising from this work and indicate future directions this research may take.

Main results of this work

- The two-centre convergent close-coupling method is generalised to positron scattering on one-electron, charged targets.
- Matrix elements for rearrangement transitions in positron scattering on positive helium ion has been derived and implemented.
- Subtraction method for integrating over the complex singularity due to the momentum-space Coulomb wave functions was developed and applied to relevant integrals in Ps-formation matrix elements.
- Antihydrogen-formation cross sections for excited states of Ps are obtained at collision energies down to 10^{-5} eV for the first time. This allowed for observation of expected threshold laws, and for cross sections to be represented in terms of simple algebraic expressions.
- Positron-He^+ scattering cross sections, free from pseudo-resonances, are obtained for all major channels of interest and over a wide range of scattering energies.

List of publications

Five peer-reviewed papers have been published on the results presented in this thesis. The author contributed to the development of the research ideas, methods, data analysis and preparation of all chapters within this manuscript and the associated publications. They are listed below in chronological order.

- A. S. Kadyrov, C. M. Rawlins, A. T. Stelbovics, I. Bray and M. Charlton, **Antihydrogen formation via antiproton scattering with excited positronium.** Phys. Rev. Lett., **114**, 183201 (2015).

- C. M. Rawlins, A. S. Kadyrov, A. T. Stelbovics, I. Bray and M. Charlton, **Calculation of antihydrogen formation via antiproton scattering with excited positronium.** Phys. Rev. A, **93**, 012709 (2016).

- C. M. Rawlins, A. S. Kadyrov and I. Bray, **Two-center convergent close-coupling approach to positron–helium-ion collisions.** Phys. Rev. A, **97**, 012707 (2018).

- C. M. Rawlins, A. S. Kadyrov and I. Bray, **Convergent close-coupling approach to positron scattering on He^+.** Eur. Phys. J. D, **72**, 77 (2018).

- A. S. Kadyrov, C. M. Rawlins, M. Charlton, I. I. Fabrikant and I. Bray, **Antihydrogen formation in low-energy antiproton collisions with**

excited-state positronium atoms. Hyperfine Interact., **239**, 42 (2018).

Statement of Contribution of Others

The contents of Chapter 2, "Positron scattering on one-electron targets", are based on the methodology presented in the publication **Two-center convergent close-coupling approach to positron-helium-ion collisions** by Rawlins et al.. The work is largely based on the work of A. S. Kadyrov and I. Bray for positron scattering on neutral targets. When explicit consideration of the long-range Coulomb interaction is required, in particular the rearrangement matrix elements in Section 2.3.3, the work was developed by the author.

The contents of Chapter 3, "Antihydrogen formation", are based on the results presented in the publications **Antihydrogen formation via antiproton scattering with excited positronium** by A. S. Kadyrov et al., **Calculation of antihydrogen formation via antiproton scattering with excited positronium** by Rawlins et al. and **Antihydrogen formation in low-energy antiproton collisions with excited-state positronium atoms** by A. S. Kadyrov et al. For these publications the cross section data for positronium scattering on antiprotons was produced by I. Bray, A. S. Kadyrov and A. T. Stelbovics. M. Charton provided valuable insight when discussing the experimental applications of these results which are briefly touched on in this thesis. More detailed discussion of the experimental work is given in the above publications and the references therein. I. Fabrikant provided valuable insight into the

near threshold behaviour of the positronium-proton system, without which the work of Section 3.2 may not have been possible. The production of the figures, least-squares fit tables and subsequent discussion was performed by the author.

The contents of Chapter 4, "Positron scattering on He^+", are based on the results presented in the publications **Two-center convergent close-coupling approach to positron-helium-ion collisions** by Rawlins et al. and **Convergent close-coupling approach to positron scattering on He^+** by Rawlins et al.. The cross section data for various processes present in positron scattering on He^+, the figures of these cross sections and the resulting discussion was produced by the author. Discussion of these results was aided by A. S. Kadyrov and I. Bray.

(Signature of Candidate)

(Signature of Supervisor)

Acknowledgements

I would like to thank my supervisor, Professor Alisher Kadyrov for providing me with such an interesting and challenging topic. His supervision and support throughout my PhD was extremely valuable, without it this thesis would not be possible.

I would also like to thank my co-supervisor, Professor Igor Bray, for providing his expertise and advice.

I am grateful to the Curtin Physics Department for providing such a warm and welcoming environment to work in.

For financial and technical support I acknowledge the Australian Government Research Training Program Scholarship, the Australian National Computing Infrastructure Facility and the Pawsey Supercomputing Centre.

Finally, I would like to thank my family and friends for hearing about my project and providing distractions when I got too obsessed.

With special thanks to my parents, for supporting me throughout my studies. Without their unwavering support I would not have developed the abilities and confidence to pursue my interests.

Chapter 1

Introduction

Antimatter has been a subject of great interest since its proposed existence by Dirac [1] in 1928. Antimatter particles were predicted to have an equal mass and opposite charge when compared with their matter counterparts. Experimental verification of the existence of antiparticles arrived in 1932 with the discovery of the antielectron, the positron. In 1955 the antiproton was observed for the first time, making it easy to conceive that every particle of matter would have a corresponding antimatter particle. And when a particle of matter would collide with its antimatter particle they would destroy each other producing energy in a process now referred to as annihilation.

Decades later, much is still unknown about antimatter. In the current model of the Big Bang it is proposed that matter and antimatter were initially created in equal amounts by pair production, the reverse of annihilation. However, the overwhelming amount of matter in the observable universe compared to the small amount of antimatter created in nuclear decay processes makes this seem unlikely. Models have been proposed to allow for this observed matter-antimatter asymmetry, but these require the violation of the charge-parity-time (CPT) symmetry [2–5]. This potential violation can be investigated by examining the spectroscopic properties of antimatter atoms, or antiatoms.

Gravitational behaviour of antimatter is another area of interest. The weak-equivalence principle (WEP) states that gravity does not depend on the internal structure of the object it acts upon [6]. According to general relativity this should include antimatter as well as matter. However, current theories of gravity run into problems at very small scales, implying that these theories are incomplete. Therefore, experimental investigations of antimatter are the best way to verify that the WEP extends to antimatter. In order to reduce the effects of stray electric and magnetic fields, the antimatter in question must be neutral.

An ideal form of antimatter for testing both spectroscopic properties and gravitational behaviour would be an antimatter equivalent to hydrogen (H), antihydrogen ($\bar{\mathrm{H}}$).

1.1 Proposed antimatter experiments

The formation and testing of $\bar{\mathrm{H}}$ have been an experimental focus for decades. $\bar{\mathrm{H}}$ was first produced and detected in 2002 by the ATHENA collaboration [7]. The formation was based on the reaction involving an antiproton ($\bar{p}$) and two positrons (e^+):

$$e^+ + e^+ + \bar{p} \rightarrow \bar{\mathrm{H}} + e^+. \tag{1.1}$$

The ATHENA collaboration evolved into the ALPHA collaboration which went on to develop an apparatus for containing $\bar{\mathrm{H}}$ for experiments. The trap is capable of holding antiatoms with kinetic energies, in temperature units, of less than 0.5 K for around 1000 seconds [8, 9] This has allowed for the most accurate measurement of the 1S-2S transition for $\bar{\mathrm{H}}$ [10]. The Atomic Spectroscopy And Collisions Using Slow Antiprotons (ASACUSA) collaboration have plans to perform measurements on the ground state hyperfine transition [11]. This will aim to make use of a polarised antiatomic beam to remove potential line-width

broadening usually found in traps [12]. However, $\bar{\mathrm{H}}$ atoms formed by reaction (1.1) can be in various states and do not lend themselves to beam-like geometry.

Another promising mechanism involves scattering of antiprotons on a bound system of an electron and positron, positronium (Ps), where the rearrangement processes

$$\mathrm{Ps}(n_{\mathrm{Ps}}, l_{\mathrm{Ps}}) + \bar{p} \rightarrow e^{-} + \bar{\mathrm{H}}(n_{\bar{\mathrm{H}}}, l_{\bar{\mathrm{H}}}) \tag{1.2}$$

are potential outcomes, where n and l are the principle and orbital angular momentum quantum numbers respectively for the bound system. This was first proposed in 1986 for ground state Ps on antiprotons to produce $\bar{\mathrm{H}}$ [13, 14]. The use of excited states of Ps was later proposed in 1990 with the observation that classically, the cross sections for $\bar{\mathrm{H}}$ formation should scale as n_{Ps}^4, where n_{Ps} is the principle quantum number of the Ps atom[15, 16]. Experimental evidence of $\bar{\mathrm{H}}$ production by this method was produced in 2004[17]. This has better directionality from the colliding $\bar{p}$ than reaction (1.1). Also, the states of the formed $\bar{\mathrm{H}}$ are dependent on the initial states of Ps used. The selection of the initial Ps state is possible through laser excitation as proposed in 2011 by Cialdi *et al.* [18]. Excitation to Ps($n = 2$) [19–22] and Ps($n = 3$) [23] is regularly performed as an initial step for excitation to Rydberg levels.

The Antihydrogen Experiment: gravity, Interferometry and Spectroscopy (AEgIS) group have plans to produce a $\bar{\mathrm{H}}$ beam by this mechanism to aid with experimental measurements [24, 25]. For this case Rydberg Ps ($n_{\mathrm{Ps}} = 20 - 50$) is required, since this leads to the production of Rydberg $\bar{\mathrm{H}}$, where the large electric dipole can be used to aid the beam formation. It is also possible to model Rydberg Ps scattering using classical mechanics. By using a classical interpretation of this scattering problem, the rearrangement cross sections have been found to scale as n_{Ps}^4. By passing this beam through a Moiré deflector it

is then possible to measure the gravity acting on the $\bar{\mathrm{H}}$ beam.

An alternative approach to gravitational measurements comes from the Gravitational Behaviour of Antihydrogen at Rest (GBAR) group [6, 26–29]. They plan to produce ultracold $\bar{\mathrm{H}}$ and perform free-fall measurements. In order to reduce the effect of the initial $\bar{\mathrm{H}}$ velocity, it must be cooled down. The aim is less than 1 m/s, or 20 μK, but H has a cooling limit of 1.3 mK. If H is similar to $\bar{\mathrm{H}}$ in this respect then this is nearly 2 orders of magnitude too high. To get around this, it was proposed by Walz and Hänsch [30] to collide the $\bar{\mathrm{H}}$, formed by reaction (1.2), with the remaining Ps to form the antihydrogen ion ($\bar{\mathrm{H}}^+$) by the rearrangement reaction:

$$\mathrm{Ps}(n_{\mathrm{Ps}}, l_{\mathrm{Ps}}) + \bar{\mathrm{H}}(n_{\mathrm{H}}, l_{\mathrm{H}}) \rightarrow e^- + \bar{\mathrm{H}}^+(1s, 1s). \tag{1.3}$$

The newly formed $\bar{\mathrm{H}}^+$ ions can then be cooled through interactions with positively charged ions to the required temperatures. The excess positron is then photo-detached leaving the neutral $\bar{\mathrm{H}}$ to free-fall.

Reaction (1.2) is seen to be the way forward for $\bar{\mathrm{H}}$ formation[31]. The experiments pose significant technical challenges though. Thus, it would be useful to have accurate scattering cross sections for reaction (1.2) (and possibly reaction (1.3)) for as many initial Ps and final $\bar{\mathrm{H}}$ states as possible. However, few investigations for reactions (1.2) and (1.3) have been performed at very low energies ($< 10^{-2}$eV), which are required for accurate measurements. Of those that do investigate this energy region, they typically only consider Ps($1s$), possibly Ps($n = 2$). These methods will be explored in more detail in the proceeding section.

Positronium scattering on antiprotons is the charge-conjugate reaction of positronium scattering on protons. To form hydrogen by a similar process to

reaction (1.2) is simply the reverse of positron scattering on hydrogen

$$e^+ + \mathrm{H}(n_\mathrm{H}, l_\mathrm{H}) \rightarrow \mathrm{Ps}(n_\mathrm{Ps}, l_\mathrm{Ps}) + p. \tag{1.4}$$

The problem of positron scattering on hydrogen is the simplest three-body system where all three particles are different. However, the possibility for Ps formation means that the system has two natural centres, the atomic target and Ps.

The same principle can be applied to reaction (1.3), as this is simply the reverse process of positron scattering on the hydrogen ion

$$e^+ + \mathrm{H}^-(1s, 1s) \rightarrow \mathrm{Ps}(n_\mathrm{Ps}, l_\mathrm{Ps}) + \mathrm{H}(n_\mathrm{H}, l_\mathrm{H}). \tag{1.5}$$

This is a four-body problem, which adds extra complexity to the proceedings. Also, unlike reaction (1.4), there is a residual long-range Coulomb interaction between the incoming positron and the target. Therefore, it would be advantageous to look into a 3-body problem with this interaction before starting with the more complex 4-body problem. For this, the problem of positron scattering on the singly-charged helium ion (He^+) will be examined.

Next we briefly review the current theoretical methods for positron scattering on hydrogen-like targets.

1.2 Current theoretical methods for positron scattering on hydrogen-like targets

Several existing methods have been extended from hydrogen targets to include hydrogen-like ions such as He^+. So for brevity the discussion focuses on methods which have been used for Ps formation with a hydrogen and He^+ target when applicable. In several cases the system of Ps-p and Ps-$\bar{p}$ are treated identically, so any change between the two systems is usually by the authors choice.

1.2.1 Variational methods

One of the most successful methods applied to the low-energy e^+-atom scattering problem is the Kohn variational method. This is typically used for energies where only elastic scattering is possible or when the number of final states is very limited. Initially developed for nuclear scattering problems in 1948 [32], it was later used for the e^++H scattering system, including Ps formation, as early as 1984.

The method involves expressing the total wave function in terms of the initial and final bound states and trial functions. The trial functions are guesses of what form of the wave function would generate the correct scattering phaseshift in terms of limited linear parameters. Through iterative calculations these trial functions are systematically improved and fitted to a convergence function to extrapolate to the exact values.

For elastic scattering the number of trial functions is relatively small and requires few partial waves. Incorporating Ps($1s$) formation increased the size of these calculations. The s-, p- and d-wave results for e^++H from this method were presented in 1984-5[33–35]. These results were converged to within 10 % and were believed to be highly accurate. From these sets of calculations, Ps-$\bar{p}$ results were produced near the threshold for ground-state Ps forming ground-state $\bar{\text{H}}$ in 1987 [36]. In 1997, the e^++H calculations were superceded by Humberston *et al.* [37] which examined the threshold region in more detail (> 0.05eV). The follow-up Ps-$\bar{p}$ results had not been published but kindly provided to us [38] and is presented in Chapter 3. The Kohn variational method is capable of generating very accurate results for elastic scattering and rearrangement but only between ground states. Incorporation of excited states is expected to increase the number of trial functions too much to be feasible.

The Kohn variational method has been applied to various e^++ion systems including He^+ [39]. For these calculations the trial functions used do not include interelectronic co-ordinates. Instead, a basis of functions centred on the nucleus are used, effectively making the problem single-centred. For the calculations only elastic scattering phase shifts and annihilation parameters were considered. For He^+, excitation occurs before Ps formation so the $He^+(n = 2)$ states would have to first be incorporated before considering the Ps centre. Using just the ground-state target functions for hydrogenlike ions still entails large-scale calculations, so excitation and, therefore, Ps formation have not yet been incorporated into this method.

The same problems can be considered with the Harris-Nesbit variational method. In 1967, Harris [40] proposed a new variational method allowing for efficient multichannel expansion. This was developed further by Nesbet [41] in the elastic scattering region and later to inelastic collisions for electron scattering [42, 43]. The method expresses the total scattering wave functions as target waves and scattered waves, constructing the scattered wave functions as trial functions composed of the spherical Neumann functions. Then variational methods similar to those used by Kohn are used until the level of desired convergence is achieved. In 1992, s-, p-, and later on, d-wave phase shifts were calculated by Liu and Gien [44] and Gien and Liu [45] using this methodology for elastic and Ps($1s$) formation in e^++H collisions. These results were consistent with the methods available at the time. These calculations typically used a six-state basis with H($n = 1, 2$) and Ps($n = 1, 2$), with further calculations performed for partial waves up to $L = 6$ [46]. These results were improved with the addition of a H($3p$) pseudostate [47] and later a Ps($3p$) pseudostate [48]. These additional states were included to correct the deficiency for the polarisability of the ground states.

The eight-pseudostate coupling scheme was used for positron-He^+ calculations [49]. In this case the spherical Neumann functions are replaced by Coulomb-type functions to better represent the positron-ion system[50]. This also considers the elastic scattering region only, but for partial waves up to $L = 6$. While these methods do not allow for direct testing of rearrangement processes for He^+, they can be used for indirect tests like internal consistency checks in Section 4.2.

1.2.2 Continuum distorted-wave method

The Continuum distorted-wave (CDW) approximation was first proposed in 1964[51] for proton scattering on hydrogen and was found to be in fairly good agreement with experiment for high energies. For light projectiles such as positrons the Continuum distorted-wave final-state (CDW-FS) model was developed by Fojón *et al.* [52] in 1996 to study Ps formation by positron capture from light hydrogen-like ions. This model expresses the initial and final channels using the Coulomb wave functions for the asymptotic states. On the same basis, the model has been adapted to four-body problems, such as positron on metastable helium [53]. For charged targets in the entrance channel, care is required to ensure the perturbative potential remains short-ranged. This model also takes into account distortions in the final channel due to the residual Coulomb interaction. When applied to a neutral target like hydrogen the initial channel Coulomb wave function reduces to a plane wave. The distortions in the final channel relate to the Coulomb continuum state of the positron and electron in the field of the residual proton.

The GBAR group, which has interest in producing both $\bar{H}$ and $\bar{H}^+$, have used this model to aid in experimental development [54, 55]. Cross sections for $\bar{H}$ and $\bar{H}^+$ formation were generated for various Ps and $\bar{H}$ states. The model

provides convenient results but is typically only valid at intermediate Ps energies (> 1 eV), lacking the accuracy required for near-threshold calculations. However, it does provide qualitative information.

The CDW-FS method was originally designed for the He^+ target, naturally taking the residual Coulomb interaction into account [52, 56]. Therefore, Ps formation results are available with this method but only for transitions between ground-state He^+ and Ps. The method is still problematic for low energies, therefore used only for high positron energies.

For a better description of scattering at low energies, the eikonal final-state continuum distorted-wave (EFS-CDW) method was developed in 1995 for impact of bare ions on hydrogen[57]. This method uses eikonal phases instead of the Coulomb waves to distort the final state. Since these phases are properly normalised they do not suffer the same problem the Coulomb wave functions do at lower energies. This was applied to e^++H in 2004 with Ps formation in mind [58, 59]. The total Ps formation cross sections from these calculations was consistent with available experiments across a wide range of energies. The method was later improved in 2011 to allow for formation of Ps in arbitrary states in Jiao *et al.* [60].

The EFS-CDW method has been applied to hydrogen-like ions, including He^+ [61]. Inclusion of excited Ps states was presented in [62]. The total Ps formation cross section agreed with that produced by scaling laws, however it still appeared to overestimate at intermediate positron impact energies (60-150 eV). Whether this represents an issue in previous calculations or in the method used is hard to determine without experimental results.

1.2.3 Monte Carlo method

The classical trajectory Monte Carlo (CTMC) method treats each particle classically and obtains their trajectories using the Newtonian equations of motion. Originally developed to calculate capture and ionisation cross sections for proton-hydrogen collisions [63] in 1966, it has been extended to collisions between other ions from 1981[64]. This method has been used to calculate cross sections for the scattering and production of Rydberg-level Ps and $\bar{\mathrm{H}}$, respectively, in 1998[65]. This takes advantage of the classical scaling law for positronium scattering on (anti)protons[15, 66]. The cross section for Ps interactions would be expected to be proportional to the size of the Ps atom. The radius of a Ps atom is proportional to the square of the principle quantum number n_{Ps}, meaning the cross sections would be proportional n_{Ps}^4. Therefore, Rydberg level Ps would be expected to produce very large cross sections in a classical interpretation of the problem. The advantage this classical method has over quantum mechanical methods is that it is easier to introduce dynamics present in real experimental set-ups, such as magnetic fields [67–69]. This allows for important tests on potential dampening or enhancements due to the presence of a magnetic field. Currently there is no quantum mechanical method which considers an external magnetic field in the calculations. However, due to the nature of the 3-body system at low energies, this classical treatment is inaccurate for calculations involving ground state or low-lying excited states. This was recently shown in Naginey *et al.* [70] where the total Ps formation cross section produced does not go to zero at the threshold as expected. Threshold corrections and energy constraints have been shown to improve the behaviour for lower impact energies [71]. However, numerical violations of energy conservation places limits on how low the positron impact energy can be.

This method has been applied to the problem of positron scattering on He^+ [71]. However, when applied to proton on He^+ there was a notable difference between the calculated results and experimental results so the same could be expected for positron scattering. Without experimental results for positron scattering on ions this is difficult to confirm. Especially, it is not clear why the increase in nuclear charge would affect a classical method and requires further investigation.

1.2.4 Close-coupling method

The most sophisticated and commonly used method is the close-coupling (CC) formalism, which is based on the expansion of the total wave function using target state wave functions. Substitution of this expansion into the Schrödinger equation yields coupled integro-differential equations in coordinate space, or Lippmann-Schwinger integral equations for the T-matrix in momentum space. By solving these equations the transition amplitudes are obtained for all open channels.

For positron-hydrogen (or conversely, Ps-proton) collisions a two-centre expansion is required to investigate rearrangement. Such a treatment readily incorporates the required boundary conditions having bound atomic and Ps channels but may potentially have double counting of the continuum. In any case the formalism results in a highly ill-conditioned system of equations.

The size of close-coupling calculations is represented with the notation CC($N, \bar{M}$), when N is the number of atomic states, M is the number of Ps states and a bar indicates pseudostates in place of eigenstates. In 1991 Higgins and Burke [72] used the CC(1,1) model across a wide range of energies and found giant spurious resonances near 40 eV positron energy. Larger calculations such

as CC($\bar{9}, \bar{9}$) [73] in 1995 and CC(3,3) [74] in 1996 found these resonances to be unphysical, but numerical artifacts. While the resonances disappeared for these larger calculations new ones appeared above the ionisation threshold. These results were superseded by CC($\bar{30}, 3$) [75] which showed smoother results.

Considerable progress in the description of the e^++H scattering problem has been made by Mitroy [76]. Using the methodology proposed in 1993 [76], several early calculations used eigenstates on both centres, typically CC(3,3) [74, 77, 78] but later CC(6,6) [79]. Along with these calculations, the inclusion of pseudostates was also considered, with increasing number of states included as the methodology became more efficient and supercomputers were more able to handle the demands of these types of calculations. CC($\bar{12}, \bar{8}$) in 1994[80], which were then superceeded by CC($\bar{13}, \bar{8}$) in 1995 [81, 82], produced elastic and Ps($1s$) formation phase shifts which were found to be in good agreement with benchmark variational calculations [33]. The largest set of calculations CC($\bar{28}, 3$) in 1997 [83–85] were found to have good agreement with the available experiments for ionisation, total scattering and positronium formation cross sections. Where possible, close-coupling calculations for Ps($1s$) $-$ $\bar{p}$ scattering were performed, with $\bar{\text{H}}$ ($1s$) formation cross sections being in good agreement with other available methods. However, modelling Ps$-\bar{p}$ scattering with few positronium states is unlikely to be accurate. This also makes the use of excited states of Ps in the entrance channel difficult.

Later, the p-Ps system was examined with a large number of calculations with the unitarised Born approximation (UBA) [82, 86, 87]. The UBA is the first Born approximation to the K-matrix, a real matrix which can be then converted into the complex T-matrix from the Lippmann-Schwinger equations. This provided a valuable check for the numerical integrity of the CC method but was unreliable for the low energies required for formation of ultra cold $\bar{\text{H}}$.

These methods typically involve solving the momentum-space Lippmann-Schwinger equation. An alternative approach taken by Bransden and Noble [88] was to leave the coupled integro-differential equations in coordinate space and solve the resulting set of equations. In this approach the inclusion of the residual Coulomb forces is much easier than in the momentum-space formalism. This is one of the reasons why one of the only calculations for e^++He^+ scattering to include Ps formation involves this type of set-up [89]. However, similar to Kernoghan *et al.* [75], the largest model used for the e^++He^+ scattering calculations only includes the $1s, 2s$ and $2p$ Ps states to remove double-counting issues. Therefore, it is possible that some information is lost near between the ionisation and Ps($n = 3$) formation thresholds where more Ps states are open. This is examined in Section 4.3 by comparing the resuilts of Bransden *et al.* [89] with our results which used a larger basis on both centres.

1.2.5 Hyperspherical coupled-channel method

The hyperspherical coupled-channel (HSCC) method was applied to atomic physics in 1968 to study doubly excited states of He [90]. The method involves writing the co-ordinate system of the particles in terms of hyperspherical variables, in order to treat the entire wave function for some hyperspherical radius R and various hyperangles.

It was first applied to e^++H in 1990 in the s-wave model [91]. For Ps($1s$) formation the calculated cross sections had good qualitative agreement with the variational calculations of Humberston [33]. While they did underestimate the variational results by around 20%, they had the best agreement with the results than other calculations had at the time. The method was developed further to include more partial waves in 1994 [92, 93]. The elastic and Ps($1s$) formation cross sections were in good agreement with the variational calculations but was

restricted to the Ore gap energy range (between the Ps($1s$) formation and H($n = 2$) excitation thresholds). With the introduction of improved numerical methods, calculations up to the H($n = 4$) excitation threshold were made possible [94].

Results for $\bar{\mathrm{H}}$ formation by Ps-$\bar{p}$ collisions have been determined using this method for initial Ps with $n_{\mathrm{Ps}} \leq 2$ and final $\bar{\mathrm{H}}$ with $n_{\bar{\mathrm{H}}} \leq 4$ [95]. The results are for Ps energies as low as 0.1 eV and provide evidence to support the use of excited states of Ps to maximise the $\bar{\mathrm{H}}$ formation yield. When compared with Mitroy and Stelbovics [86] UBA results a qualitative similarity can be observed, but for the lowest energies in the calculations the cross sections exhibit very different behaviours. Further work has not been performed to extend these calculations to lower energies or for higher n_{Ps} values to see if the increase of $\bar{\mathrm{H}}$ formation cross sections continues for increasing n_{Ps}.

This method has been applied to the e^++He^+ in order to examine s-wave resonances in 1997 [96] and, later in 2004, p-wave resonances [97]. Despite the success of these investigations, there has not been any further development for this system.

1.2.6 Faddeev equations

When working with three-body systems, typically different sets of local co-ordinates are required to account for the asymptotic behaviour of the total wave function. In a lot of cases this mixing of co-ordinates makes the Schrödinger equation difficult to solve. In order to make the calculations more manageable, in 1993 it was proposed to divide the total wave function into Faddeev components, such that each component would contain one set of co-ordinates[98].

This method was applied to $e^{\pm}$+H scattering for the s-wave model in 1995

[99]. The elastic scattering phase shifts were found to be in very good agreement with previous calculations. The same can be said of Ps($1s$) formation within the Ore gap. The method was further developed to include more angular momentum states in 1999 for e^++H [100]. This mainly considered the Ore gap energy range so only elastic scattering and Ps($1s$) formation channels are available, but the resulting cross sections were in good agreement with the available methods. However, they also examined the case for Ps($1s$)+p beyond the Ore gap to investigate the formation of H in $n_{\mathrm{H}} = 2$ excited states compared to in the ground state. It was observed that as Ps energy increased, the H formation in excited states becomes more favoured. This was only observed over a small energy region just above H($n = 2$) formation where a sharp increase in these cross sections is expected.

Investigations into antihydrogen formation via this sort of mechanism began in 2001 for Ps($1s$) [101] and later for Ps($n = 2$) [102]. Much of the focus was on differential cross sections rather than total cross sections.

1.2.7 Time-dependent coupled-channel method

For many early e^++H calculations involving a two-centre close-coupling expansion, unphysical resonances at intermediate energies were cause for concern. These were removed in [75] and [83] by including only the $1s, 2s$ and $2p$ Ps states to avoid the double-counting issues. However, at intermediate energies where more Ps states are open, this treatment misses important details.

A close-coupling treatment which overcomes this overcompleteness issue is the time-dependent coupled-channel (TDCC) method developed in 1981[103]. In this approach the relative motion of the fragments in the three-body system is described by a wave packet. This wave packet is time evolved on a lattice of

the two-dimensional radial space [104]. An advantage of this treatment is that no asymptotic boundary conditions are required for the total wave function, meaning that Ps formation and ionisation channels do not need to be treated separately. However, it was not applied to positron scattering until 1998 [105] using distorted waves. These results were consistent with other close-coupling methods but were only valid for intermediate energies (> 30 eV). Calculations close to the Ps($1s$) formation threshold were performed by Yamanaka and Kino [104] in 2001. The total Ps formation cross sections produced by these calculations was found to be consistent with previous experiments and theories. Total $\bar{\mathrm{H}}$ formation cross sections with this method typically favoured CC($2\bar{8}$,3)[85] results with some corrections [106, 107]. However, individual transitions have not been presented and the results that have been presented only go as low as 3.2 eV.

1.3 Convergent close-coupling method

The convergent close-coupling (CCC) method is also based on the close-coupling scheme. The total wave function is expanded using a sufficiently large orthogonal Laguerre basis in order to obtain converged amplitudes for the possible scattering processes. Initially developed for the problem of electron scattering on hydrogen [108] in 1992. It has also achieved great success with the problem of positron scattering on hydrogen [109].

The full two-centre CCC formalism allows for both centres to be treated equally, unlike calculations by Kernoghan *et al.* [75] which only used 3 Ps states. This produced cross sections for Ps formation in excited states with no oscillatory behaviour. However, the underlying equations are highly ill-conditioned and require careful application of numerical techniques to deal with the issues arising

from this ill-conditioning. Cross sections for the scattering of Ps($1s$) to form $\bar{\text{H}}$ ($1s$) were produced with the CCC method for the zeroth partial wave [110]. The results agreed with those of Mitroy [81, 82] obtained using a similar basis size. They were also able to extend the results to a region 2 orders of magnitude lower in terms of Ps energy. This was enough to observe the expected $1/k$ behaviour predicted by Wigner [111], where k is the linear momentum of the Ps atom. Therefore, it is expected that the inclusion of more partial waves and states on both centres would allow for the accurate calculation of $\bar{\text{H}}$ formation.

The CCC method has been extended to include positron scattering on other neutral targets such as helium [112–114], magnesium [115], alkalis [116–118] and most recently, molecular hydrogen [119]. A review of the work performed for these targets is given in Kadyrov and Bray [120]. However, it has not been applied to charged targets due to the residual Coulomb interaction having never been implemented for Ps-formation channels. The CCC method has been used for charged targets such as He^+ for electron scattering [121, 122]. Therefore, new matrix elements for Ps formation are the only requirements for solving the problem of positron scattering on a charged target like He^+.

The aim of this project is to produce accurate $\bar{\text{H}}$ formation cross sections close to the threshold for various incoming Ps and newly formed $\bar{\text{H}}$ states. Along with these results we present a generalised CCC formalism for positron scattering on charged targets with results from positron on a He^+ target given. This way we can determine if such a formalism could also work on H^- and in time, allow us to generate accurate $\bar{\text{H}}^+$ cross sections.

Chapter 2

Positron scattering on one-electron targets

The two-centre CCC method is based on expanding the total wavefunction of the scattering system using the bases of target and Ps states. Using this two-centre expansion in the Schrödinger equation transforms it into a set of momentum-space Lippmann-Schwinger equations. The solution of these equations yields the scattering amplitude for all open channels.

For positron scattering on the hydrogenlike ion He^+ much of the theory is the same as for the hydrogen atom. The following is, therefore, written in terms of a hydrogenlike target with a nuclear charge Z. The formalism will be developed for arbitrary Z, but when necessary, and possible, Z will be set equal to 1 allowing for direct comparison with e^+-H equations as stated in Ref. [109]. Much of the formalism of the close-coupling equations and direct transition matrix elements share common ideas from e^--He^+ [122] and e^+-H [109]. However, rearrangement transition matrix elements presented in Section 2.3.3 are new to the e^+-He^+ CCC method [123]. Atomic units are used throughout unless otherwise specified.

2.1 Formalism

Consider a system of three particles, positron (1), the target nucleus (2) and an electron (3). Index α (β) will denote a quantum state in which the positron (nucleus) is free and the other two form a bound state. With this notation the total scattering wave function of the three-body system at a total energy E may be written as

$$(E - H)\Psi = 0, \tag{2.1}$$

where

$$H = H_0 + v_1 + v_2 + v_3 \equiv H_0 + v, \tag{2.2}$$

and H_0 is the free-three-particle Hamiltonian, and v_i is the Coulomb interaction between particles j and k ($i, j, k = 1, 2, 3$; $i \neq j \neq k$). The free three-particle Hamiltonian can be written in equivalent forms for each channel:

$$\begin{aligned} H_0 =& -\frac{1}{2M_1}\nabla^2_{\boldsymbol{\rho}_1} - \frac{1}{2\mu_1}\nabla^2_{\boldsymbol{r}_1} \\ =& -\frac{1}{2M_2}\nabla^2_{\boldsymbol{\rho}_2} - \frac{1}{2\mu_2}\nabla^2_{\boldsymbol{r}_2}, \end{aligned} \tag{2.3}$$

where M and μ are the reduced mass of the fragments and the bound pair, respectively. For positron scattering on an atomic target $M_1 = 1, M_2 = 2, \mu_1 = 1, \mu_2 = 1/2$. The total Hamiltonian can be expressed in the following ways

$$\begin{aligned} H =& H_1 - \frac{1}{2M_1}\nabla^2_{\boldsymbol{\rho}_1} + v_2 + v_3 \\ =& H_2 - \frac{1}{2M_2}\nabla^2_{\boldsymbol{\rho}_2} + v_1 + v_3, \end{aligned} \tag{2.4}$$

where the bound pair Hamiltonians are given by

$$H_1 = -\frac{1}{2\mu_1}\nabla^2_{\boldsymbol{r}_1} + v_1 \tag{2.5}$$

$$H_2 = -\frac{1}{2\mu_2}\nabla^2_{\boldsymbol{r}_2} + v_2. \tag{2.6}$$

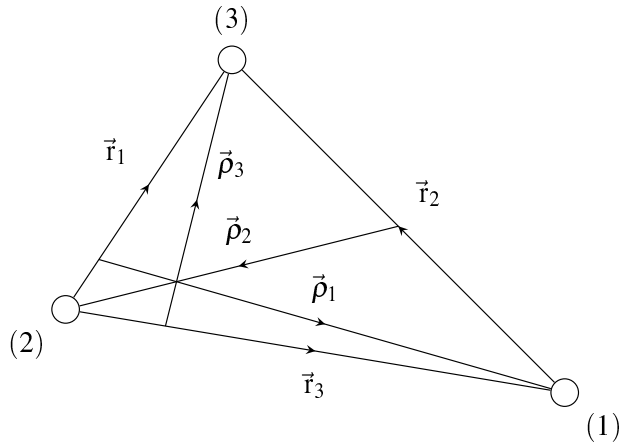

Figure 2.1: Jacobi coordinates for the system of three particles: positron (1), the target nucleus (2), and electron (3).

The Jacobi variable $\boldsymbol{r}_{jk}$ is the position of particle j relative to k and $\boldsymbol{\rho}_i$ is the position of the particle i relative to the centre of mass (c.m.) of pair jk $(i, j, k = 1, 2, 3; i \neq j \neq k)$. Since j and k are the particles excluding i, we can simplify and set $\boldsymbol{r}_{jk} = \boldsymbol{r}_i$. See Fig. 2.1. For these three particles, the potential reactions channels for positron scattering on the α bound state include:

$$1 + (2 + 3) \rightarrow \begin{cases} 1 + (2 + 3) \text{ (Elastic)} \\ 1 + (2 + 3)^* \text{ (Excitation)} \\ 1 + 2 + 3 \text{ (Breakup)} \\ (1 + 3) + 2 \text{ (Rearrangement.)} \end{cases} \tag{2.7}$$

Expanding the total scattering wave function Ψ in terms of the two-body pseudostate wave functions describing the target atom (T) and the Ps subspaces yields:

$$\Psi = \sum_{\alpha=1}^{N_{\mathrm{T}}} F_\alpha(\boldsymbol{\rho}_1)\psi_\alpha(\boldsymbol{r}_1) + \sum_{\beta=1}^{N_{\mathrm{Ps}}} F_\beta(\boldsymbol{\rho}_2)\psi_\beta(\boldsymbol{r}_2). \tag{2.8}$$

The pseudostates are introduced subject to conditions:

$$\langle \psi_{\gamma'} | \psi_\gamma \rangle = \delta_{\gamma'\gamma} \tag{2.9}$$

$$\langle \psi_{\gamma'} | H_\gamma | \psi_\gamma \rangle = \delta_{\gamma'\gamma}\epsilon_{\gamma'}. \tag{2.10}$$

Substituting Eq. (2.8) into Eq. (2.1)

$$(E-H)\left(\sum_{\alpha=1}^{N_{\rm T}} F_\alpha(\boldsymbol{\rho}_1)\psi_\alpha(\boldsymbol{r}_1)+\sum_{\beta=1}^{N_{\rm Ps}} F_\beta(\boldsymbol{\rho}_2)\psi_\beta(\boldsymbol{r}_2)\right)=0, \tag{2.11}$$

and rearranging Eq. (2.11) we get

$$\begin{aligned}(E-H_1+\frac{1}{2M_1}\nabla^2_{\boldsymbol{\rho}_1})\sum_{\alpha=1}^{N_{\rm T}} F_\alpha(\boldsymbol{\rho}_1)\psi_\alpha(\boldsymbol{r}_1) =&(H-E)\sum_{\beta=1}^{N_{\rm Ps}} F_\beta(\boldsymbol{\rho}_2)\psi_\beta(\boldsymbol{r}_2)\\ &+(v_2+v_3)\sum_{\alpha=1}^{N_{\rm T}} F_\alpha(\boldsymbol{\rho}_1)\psi_\alpha(\boldsymbol{r}_1)\\ (E-H_2+\frac{1}{2M_2}\nabla^2_{\boldsymbol{\rho}_2})\sum_{\beta=1}^{N_{\rm Ps}} F_\beta(\boldsymbol{\rho}_2)\psi_\beta(\boldsymbol{r}_2) =&(H-E)\sum_{\alpha=1}^{N_{\rm T}} F_\alpha(\boldsymbol{\rho}_1)\psi_\alpha(\boldsymbol{r}_1)\\ &+(v_1+v_3)\sum_{\beta=1}^{N_{\rm Ps}} F_\beta(\boldsymbol{\rho}_2)\psi_\beta(\boldsymbol{r}_2).\end{aligned} \tag{2.12}$$

Following Ref. [122] we introduce an arbitrary distorting potential U_i. The choice of U_i will be considered near the end of this section. Subtracting the distorting potential from both sides of the equations we obtain

$$\begin{aligned}&(E-H_1+\frac{1}{2M_1}\nabla^2_{\boldsymbol{\rho}_1}-U_1)\sum_{\alpha=1}^{N_{\rm T}} F_\alpha(\boldsymbol{\rho}_1)\psi_\alpha(\boldsymbol{r}_1)\\ &=(H-E)\sum_{\beta=1}^{N_{\rm Ps}} F_\beta(\boldsymbol{\rho}_2)\psi_\beta(\boldsymbol{r}_2)+(v_2+v_3-U_1)\sum_{\alpha=1}^{N_{\rm T}} F_\alpha(\boldsymbol{\rho}_1)\psi_\alpha(\boldsymbol{r}_1)\\ &(E-H_2+\frac{1}{2M_2}\nabla^2_{\boldsymbol{\rho}_2}-U_2)\sum_{\beta=1}^{N_{\rm Ps}} F_\beta(\boldsymbol{\rho}_2)\psi_\beta(\boldsymbol{r}_2)\\ &=(H-E)\sum_{\alpha=1}^{N_{\rm T}} F_\alpha(\boldsymbol{\rho}_1)\psi_\alpha(\boldsymbol{r}_1)+(v_1+v_3-U_2)\sum_{\beta=1}^{N_{\rm Ps}} F_\beta(\boldsymbol{\rho}_2)\psi_\beta(\boldsymbol{r}_2).\end{aligned} \tag{2.13}$$

Projecting from the left side on the target states $\psi_{\alpha'}$ (Ps states $\psi_{\beta'}$) and making use of Eqs. (2.9)-(2.10) the following equations for the expansion functions of

$F_{\alpha'}$ and $F_{\beta'}$ are obtained

$$\begin{aligned}(E-\epsilon_{\alpha'}+\frac{1}{2M_{\alpha'}}\nabla^2_{\boldsymbol{\rho}_1}-U_1)F_{\alpha'}(\boldsymbol{\rho}_1) =&\langle\psi_{\alpha'}|U_{12}\sum_{\beta=1}^{N_{\rm Ps}}|\psi_\beta\rangle F_\beta(\boldsymbol{\rho}_2)\\ &+\langle\psi_{\alpha'}|U_{11}\sum_{\alpha=1}^{N_{\rm T}}|\psi_\alpha\rangle F_\alpha(\boldsymbol{\rho}_1) \qquad (2.14)\\ (E-\epsilon_{\beta'}+\frac{1}{2M_{\beta'}}\nabla^2_{\boldsymbol{\rho}_2}-U_2)F_{\beta'}(\boldsymbol{\rho}_2) =&\langle\psi_{\beta'}|U_{21}\sum_{\alpha=1}^{N_{\rm T}}|\psi_\alpha\rangle F_\alpha(\boldsymbol{\rho}_1)\\ &+\langle\psi_{\beta'}|U_{22}\sum_{\beta=1}^{N_{\rm Ps}}|\psi_\beta\rangle F_\beta(\boldsymbol{\rho}_2), \qquad (2.15)\end{aligned}$$

where the channel potentials are given by

$$\begin{aligned}U_{11} =&v-v_1-U_1,\ U_{22}=v-v_2-U_2,\\ U_{12} =&U_{21}=H-E. \qquad (2.16)\end{aligned}$$

We can write equations (2.14) and (2.15) in the following way by combining α and β into a single index γ

$$\left(E-\epsilon_{\gamma'}-\hat{K}_{\gamma'}\right)\tilde{F}_{\gamma'}=\sum_\gamma Z_{\gamma'\gamma}\tilde{F}_\gamma. \qquad (2.17)$$

It can be seen that

$$\begin{aligned}&\text{if } \gamma'=\alpha' \text{ and } \gamma=\alpha \text{ then} \qquad (2.18)\\ &\quad \epsilon_\gamma=\epsilon_\alpha,\ \tilde{F}_\gamma=F_\alpha,\ \hat{K}_\gamma=\frac{-1}{2M_1}\nabla^2_{\boldsymbol{\rho}_1}+U_1,\ Z_{\alpha'\alpha}=\langle\psi_{\alpha'}|U_{11}|\psi_\alpha\rangle,\\ &\text{if } \gamma'=\beta' \text{ and } \gamma=\beta \text{ then}\\ &\quad \epsilon_\gamma=\epsilon_\beta,\ \tilde{F}_\gamma=F_\beta,\ \hat{K}_\gamma=\frac{-1}{2M_2}\nabla^2_{\boldsymbol{\rho}_2}+U_2,\ Z_{\alpha'\alpha}=\langle\psi_{\beta'}|U_{22}|\psi_\beta\rangle,\\ &\text{if } \gamma'=\beta \text{ and } \gamma=\alpha \text{ then } Z_{\beta,\alpha}=\langle\psi_\beta|U_{21}|\psi_\alpha\rangle.\end{aligned}$$

By defining the operator of the Green's function

$$\hat{\mathcal{G}}_\gamma=(E-\epsilon_\gamma-\hat{K}_\gamma)^{-1}, \qquad (2.19)$$

we can write the formal solution of the differential equation (2.17) in the form of

$$\tilde{F}_{\gamma'} = \tilde{F}_0 + \hat{\mathcal{G}}_{\gamma'} \sum_{\gamma} Z_{\gamma'\gamma} \tilde{F}_{\gamma}, \tag{2.20}$$

where $\tilde{F}_0$ is a solution of Eq. (2.17) when the right hand side is 0, i.e. $\hat{\mathcal{G}}_{\gamma'}^{-1}\tilde{F}_0 = 0$. For arbitrary distorting potentials U_1 and U_2 the solution $\tilde{F}_0$ is given as a distorted wave $|\boldsymbol{q}_\gamma^{(\pm)}\rangle$ of relative motion which satifies

$$\mathcal{G}_\gamma^{-1}|\boldsymbol{q}_\gamma^{(\pm)}\rangle = (E - \epsilon_\gamma - q_\gamma^2/(2M_\gamma))|\boldsymbol{q}_\gamma^{(\pm)}\rangle, \tag{2.21}$$

and is normalised according to

$$\langle \boldsymbol{q}_{\gamma'}^{(\pm)}|\boldsymbol{q}_\gamma^{(\pm)}\rangle = (2\pi)^3\delta(\boldsymbol{q}_{\gamma'} - \boldsymbol{q}_\gamma). \tag{2.22}$$

Therefore we can write

$$\mathcal{G}_{\gamma'}^{(\pm)} = \int \frac{d\boldsymbol{q}_{\gamma''}}{(2\pi)^3} \frac{|\boldsymbol{q}_{\gamma''}^{(\pm)}\rangle\langle \boldsymbol{q}_{\gamma''}^{(\pm)}|}{E - \epsilon_{\gamma'} - q_{\gamma''}^2/(2M_{\gamma'}) \pm i0}. \tag{2.23}$$

The above integral contains a singular point at $q_{\gamma''}^2/2M_{\gamma'} = E - \epsilon_{\gamma'}$. The addition of $\pm i0$ defines the integration path around the singularity point at $q_{\gamma'} = \sqrt{2M_{\gamma'}(E^+ - \epsilon_{\gamma'})}$ and, depending on its sign, corresponds to outgoing $(+)$ or incoming $(-)$ boundary conditions.

The formal solution of Eq. (2.20) is

$$|\tilde{F}_{\gamma'}\rangle = |\boldsymbol{q}_{\gamma'}^{(+)}\rangle + \sum_{\gamma} \int \frac{d\boldsymbol{q}_{\gamma''}}{(2\pi)^3} \frac{|\boldsymbol{q}_{\gamma''}^{(+)}\rangle}{E - \epsilon_{\gamma'} - q_{\gamma''}^2/(2M_{\gamma'}) + i0} \langle \boldsymbol{q}_{\gamma''}^{(+)}|Z_{\gamma'\gamma}|\tilde{F}_\gamma\rangle. \tag{2.24}$$

For the collision channel with initial target state i and incoming wave $|\boldsymbol{q}_i^{(+)}\rangle$ the outgoing (with $+i0$) asymptotes of $F_\gamma(x)$ (where x is ρ_1 for α channels and ρ_2 for β channels) at $x \to \infty$ must be

$$\tilde{F}_{\gamma'}(x) \overset{x\to\infty}{=} \delta_{\gamma',i} e^{i\boldsymbol{q}_i\boldsymbol{x} + i\eta\ln(q_i x - \boldsymbol{q_i x})} + f(\boldsymbol{q}_\gamma, \boldsymbol{q}_i) \frac{e^{iq_{\gamma'}x - i\eta\ln|2q_{\gamma'}x|}}{x}, \tag{2.25}$$

where $f(\boldsymbol{q}_\gamma, \boldsymbol{q}_i)$ is the scattering amplitude, η is the Sommerfeld parameter (where η is $z_1(z_2+z_3)/q$ for α channels and $z_2(z_1+z_3)/q$ for β channels) and $q_{\gamma'} = \sqrt{2M_\gamma(E-\epsilon_{\gamma'})}$.

The asymptotic form of Eq. (2.24) can be expressed as

$$\tilde{F}_{\gamma'}(x) \overset{x\to\infty}{=} \delta_{\gamma',i} e^{i\boldsymbol{q}_i\boldsymbol{x}+i\eta\ln(q_i x-\boldsymbol{q_i x})} + \sum_\gamma \int \frac{d\boldsymbol{q}_{\gamma''}}{(2\pi)^3} \frac{e^{i\boldsymbol{q}_{\gamma''}\boldsymbol{x}+i\eta\ln(q_{\gamma''}x-\boldsymbol{q_{\gamma''}.x})}}{E-\epsilon_{\gamma'}-q^2_{\gamma''}/(2M_{\gamma'})+i0}\langle \boldsymbol{q}^{(+)}_{\gamma''}|Z_{\gamma'\gamma}|\tilde{F}_\gamma\rangle, \quad (2.26)$$

where we can calculate the integral with a singularity at $\frac{q^2_{\gamma''}}{2M_{\gamma'}} = E-\epsilon_{\gamma'}$ by using the contour integration technique. Utilising the result [124]

$$e^{i\boldsymbol{q}\boldsymbol{x}+i\eta\ln(qx-\boldsymbol{q}\boldsymbol{x})} \overset{x\to\infty}{\sim} \frac{2\pi}{iqx}\left(e^{iqx-i\eta\ln|2qx|}\delta(\hat{\boldsymbol{q}}-\hat{\boldsymbol{x}}) - e^{-iqx+i\eta\ln|2qx|}\delta(\hat{\boldsymbol{q}}+\hat{\boldsymbol{x}})\right), \quad (2.27)$$

we get

$$\tilde{F}_{\gamma'}(x) \overset{x\to\infty}{=} \delta_{\gamma',i} e^{i\boldsymbol{q}_i\boldsymbol{x}+i\eta\ln(q_i x-\boldsymbol{q_i x})} - \sum_\gamma \frac{M_{\gamma'}}{2\pi}\frac{e^{iq_{\gamma'}x-i\eta\ln|2q_{\gamma'}x|}}{x}\langle q^{(+)}_{\gamma'}|Z_{\gamma'\gamma}|\tilde{F}_\gamma\rangle, \quad (2.28)$$

where $\langle q^{(+)}_{\gamma'}|$ is the distorted wave function when $q_{\gamma'}$ and x are aligned. Comparing this result with Eq. (2.25) we find that

$$f_{\gamma' i}(\boldsymbol{q}_{\gamma'}, \boldsymbol{q}_i) = -\frac{M_{\gamma'}}{2\pi}\sum_\gamma \langle q^{(+)}_{\gamma'}|Z_{\gamma'\gamma}|\tilde{F}_\gamma\rangle. \quad (2.29)$$

From the definition of the on-shell T-matrix

$$T_{\gamma'\gamma}(\boldsymbol{q}_\gamma, \boldsymbol{q}_\gamma) = -\frac{1}{(2\pi)^2 M_{\gamma'}} f_{\gamma'\gamma}(\boldsymbol{q}_\gamma, \boldsymbol{q}_\gamma), \quad (2.30)$$

it follows that

$$T_{\gamma' i}(\boldsymbol{q}_{\gamma'}, \boldsymbol{q}_i) = \frac{1}{(2\pi)^3}\sum_\gamma \langle q^{(+)}_{\gamma'}|Z_{\gamma'\gamma}|\tilde{F}_\gamma\rangle. \quad (2.31)$$

Therefore, Eq. (2.24) can be written as

$$|\tilde{F}_{\gamma'}\rangle = |\boldsymbol{q}^{(+)}_i\rangle + \int d\boldsymbol{q}_{\gamma''}\frac{|\boldsymbol{q}^{(+)}_{\gamma''}\rangle}{E-\epsilon_{\gamma'}-q^2_{\gamma''}/(2M_{\gamma'})+i0}T_{\gamma''\gamma}(\boldsymbol{q}_{\gamma''}, \boldsymbol{q}_\gamma). \quad (2.32)$$

Using Eq. (2.32) in Eq. (2.24) we get the Lippmann-Schwinger type equations for the T-matrices

$$T_{\gamma'\gamma}(\boldsymbol{q}_{\gamma'},\boldsymbol{q}_{\gamma}) = \langle \boldsymbol{q}_{\gamma'}^{(+)}|Z_{\gamma',\gamma}|\boldsymbol{q}_{\gamma}^{(+)}\rangle + \sum_{\gamma''=1}\int \frac{d\boldsymbol{q}''}{(2\pi)^3}\frac{\langle \boldsymbol{q}_{\gamma'}^{(+)}|Z_{\gamma'\gamma''}|\boldsymbol{q}_{\gamma''}^{(+)}\rangle}{E-\epsilon_{\gamma'}-q_{\gamma''}^2/(2M_{\gamma''})+i0}T_{\gamma''\gamma}(\boldsymbol{q}_{\gamma''},\boldsymbol{q}_{\gamma}). \quad (2.33)$$

Denoting the effective potential matrix elements $V_{\gamma'\gamma}$

$$V_{\gamma'\gamma}(\boldsymbol{q}_{\gamma'},\boldsymbol{q}_{\gamma}) = \langle \boldsymbol{q}_{\gamma'}^{(+)}|Z_{\gamma',\gamma}|\boldsymbol{q}_{\gamma}^{(+)}\rangle, \quad (2.34)$$

we get

$$T_{\gamma'\gamma}(\boldsymbol{q}_{\gamma'},\boldsymbol{q}_{\gamma}) = V_{\gamma'\gamma'}(\boldsymbol{q}_{\gamma'},\boldsymbol{q}_{\gamma'}) + \sum_{\gamma''=1}^{N_{\rm T}+N_{\rm Ps}}\int \frac{d\boldsymbol{q}_{\gamma''}}{(2\pi)^3}V_{\gamma'\gamma''}(\boldsymbol{q}_{\gamma'},\boldsymbol{q}_{\gamma''})G_{\gamma''}(q_{\gamma''}^2)T_{\gamma''\gamma}(\boldsymbol{q}_{\gamma''},\boldsymbol{q}_{\gamma}), \quad (2.35)$$

Where $\gamma = \alpha, \beta$ and $\boldsymbol{q}_{\gamma}$ is the momentum of the free particle relative to c.m. of the bound pair in channel γ. The effective two-body free Green's function are defined by

$$G_{\gamma}(q_{\gamma}^2) = (E-\epsilon_{\gamma}-q_{\gamma}^2/(2M_{\gamma})+i0)^{-1}. \quad (2.36)$$

However, these coupled equations are defined in terms of some arbitrary distorting potential U and are, therefore, non-physical. In order to extract physical observables a relationship between the distorted $T_{\gamma'\gamma}$ with the physical $T_{\gamma'\gamma}^{\rm P}$ must be established. This is done by using

$$T_{\gamma'\gamma}^{\rm P}(\boldsymbol{q}_{\gamma'},\boldsymbol{q}_{\gamma}) = T_{\gamma'\gamma}(\boldsymbol{q}_{\gamma'},\boldsymbol{q}_{\gamma}) + \delta_{\gamma'\gamma}\langle \boldsymbol{q}_{\gamma'}^{(+)}|U_i|\boldsymbol{q}_{\gamma}\rangle, \quad (2.37)$$

where $|\boldsymbol{q}_{\gamma}\rangle$ refers to the Coulomb function for charged targets or a plane wave for neutral targets [122]. The second term of Eq. (2.37) is referred to as the Rutherford term. For neutral targets the U_i is typically selected to be short-ranged and, therefore, asymptotically zero. However, for charged targets there

is a long-range term due to the residual charge, meaning the second term in Eq. (2.37) becomes infinite. Since this only effects the elastic cross sections this term is not calculated, but it is stated in the discussion of Chapter 4 that the relevant integrated cross sections should be infinite. The elastic and total cross sections determined without this term have no physical interpretation but makes convergence tests possible to perform for these values.

For the hydrogen atom and the helium ion the distorting potentials U_1 and U_2 only represent the residual long-range Coulomb interation as expressed by $U_1 = z_1(z_2 + z_3)/\rho_1 = (Z-1)/\rho_1$ and $U_2 = z_2(z_1 + z_3)/\rho_\beta = 0$. For hydrogen $U_1 = U_2 = 0$, so the plane wave representation of the projectile is used in both centres. For He^+ $U_1 = 1/\rho_1$ and $U_2 = 0$, so the Coulomb wave representation is used for the projectile in the He^+ centre but the Ps centre keeps the plane wave representation.

The equations derived in this section are valid for other types of distorting potentials as well, such as those required for targets with electrons in an inner shell. However, the effective potentials $V_{\gamma',\gamma}(\boldsymbol{q}_{\gamma'}, \boldsymbol{q}_\gamma)$ presented in the following section are valid only for the Coulombic distorting potentials.

The Hamiltonian in Eq. (2.2) conserves the total angular momentum J. Therefore, it is practical to solve Eq. (2.35) for a given J. To achieve this we use a partial-wave expansion in the total orbital angular momentum J according to

$$V_{\gamma'\gamma}(\boldsymbol{q}_{\gamma'}, \boldsymbol{q}_\gamma) = \sum_{L'M'LMJK} Y_{L'M'}(\widehat{\boldsymbol{q}}_{\gamma'}) C^{JK}_{L'M'l'm'} \mathcal{V}^{L'L}_{\gamma'\gamma}(q_{\gamma'}, q_\gamma) C^{JK}_{LMlm} Y^*_{LM}(\widehat{\boldsymbol{q}}_\gamma). \quad (2.38)$$

The same expansion is also used for $T_{\gamma'\gamma}$. With this Eq. (2.35) can be written

as (for each J)

$$\mathcal{T}^{L'L}_{\gamma'\gamma}(q_{\gamma'},q_{\gamma}) = \mathcal{V}^{L'L}_{\gamma'\gamma'}(q_{\gamma'},q_{\gamma'}) + \sum_{L''}\sum_{\gamma''=1}^{N_{\rm T}+N_{\rm Ps}} \int \frac{d\boldsymbol{q}_{\gamma''}}{(2\pi)^3} \mathcal{V}^{L'L}_{\gamma'\gamma''}(q_{\gamma'},q_{\gamma''}) G_{\gamma''}(q^2_{\gamma''}) \mathcal{T}^{L'L}_{\gamma''\gamma}(q_{\gamma''},q_{\gamma}). \tag{2.39}$$

Details for solving Eq. 2.39 are given in Section 2.4. The effective potentials in the representation of the total angular momentum are given by

$$\mathcal{V}^{L'L}_{\gamma'\gamma}(q_{\gamma'},q_{\gamma}) = \sum_{m'mM'M} \int\int d\widehat{\boldsymbol{q}}_{\gamma'} d\widehat{\boldsymbol{q}}_{\gamma} Y^*_{L'M'}(\widehat{\boldsymbol{q}}_{\gamma'}) C^{JK}_{L'M'l'm'} V_{\gamma'\gamma}(\boldsymbol{q}_{\gamma'},\boldsymbol{q}_{\gamma}) \times C^{JK}_{LMlm} Y_{LM}(\widehat{\boldsymbol{q}}_{\gamma}). \tag{2.40}$$

The angular momentum of pair $\gamma(\gamma')$ is $l(l')$, and M, m, K are the projections of L, l, J, respectively. Accordingly, $K = M + m = M' + m'$.

2.2 Target atom and positronium structure

The H, He^+ and Ps structures can all be written as

$$\psi_{\gamma}(\boldsymbol{r}) = R_{nl}(r) Y_{lm}(\widehat{\boldsymbol{r}}), \tag{2.41}$$

where index γ denotes a full set of quantum numbers describing the target (α) or the Ps (β) states. The radial part of the wave function is represented as a linear combination of N Laguerre functions

$$R_{nl}(r) = \sum_{k=1}^{N} B^l_{nk} \xi_{kl}(r). \tag{2.42}$$

The Laguerre functions are defined as

$$\xi_{kl}(r) = \left(\frac{\lambda_l (k-1)!}{(2l+1+k)!}\right)^{1/2} (\lambda_l r)^{l+1} e^{-\lambda_l r/2} L^{2l+2}_{k-1}(\lambda_l r). \tag{2.43}$$

For rearrangement transitions momentum-space pseudostate wave functions and pseudo-form-factors are required. The analytic forms of these equations are given in Ref. [109].

2.3 Effective potentials

In order to solve Eq. 2.39 the effective potentials $\mathcal{V}^{L'L}_{\gamma'\gamma}(q_{\gamma'}, q_\gamma)$ need to be calculated for various initial and final conditions. Given below is the derivation of these matrix elements for the three possible interactions in a positron-ion system.

2.3.1 Direct atom-atom transitions

For transitions between atomic states we have

$$\begin{aligned} V_{\alpha'\alpha}(\boldsymbol{q}_{\alpha'}, \boldsymbol{q}_\alpha) \equiv & \langle \boldsymbol{q}_{\alpha'} | \langle \psi_{\alpha'} | U_{11} | \psi_\alpha \rangle | \boldsymbol{q}_\alpha \rangle \\ = & \int\int d\boldsymbol{\rho}_1 d\boldsymbol{r}_1 \psi^{*C}_{\boldsymbol{q}_{\alpha'},\eta'}(\boldsymbol{\rho}_1) \psi^*_{\alpha'}(\boldsymbol{r}_1) U_{\alpha\alpha} \psi_\alpha(\boldsymbol{r}_1) \psi^C_{\boldsymbol{q}_\alpha,\eta}(\boldsymbol{\rho}_1), \end{aligned} \tag{2.44}$$

where $\psi^{\rm C}_{\boldsymbol{q}_\alpha,\eta}(\boldsymbol{\rho_1})$ is the Coulomb wave function representing the motion of the electron in the field of the He^{2+} ion, $\eta = (Z-1)/q_\alpha$ in a.u. where Z is the charge of the nucleus. This will be left general for direct comparison with the e^++H system where $Z = 1$. In the case of He^+, $Z = 2$. How this will differ from the neutral target case will be examined in what follows.

Expanding the Coulomb waves of relative motion yields

$$\widetilde{\psi}^{\rm C}_{\boldsymbol{q}_\alpha,\eta}(\boldsymbol{\rho}_1) = 4\pi \sum_{LM} i^L Y^*_{LM}(\widehat{\boldsymbol{q}}_\alpha) Y_{LM}(\widehat{\boldsymbol{\rho}_1}) \frac{F_L(\eta, q_\alpha \rho_1)}{q_\alpha \rho_1}, \tag{2.45}$$

where F_L is the regular Coulomb wave function. Note that the complex phase factor $e^{i\sigma_L} = \mathrm{Arg}\Gamma(i\eta + L + 1)$ is not included in this expansion. This allows for $V_{\gamma',\gamma}$ to be solved using real arithmetic and is further elaborated on in Section 2.4.

Substituting Eq. (2.44) into Eq. (2.40) and using Eq. (2.45) we get

$$\mathcal{V}^{L'L}_{\alpha'\alpha}(q_{\alpha'},q_\alpha) =(4\pi)^2 i^{L-L'} \sum_{m',m,M',M} C^{L'l'J}_{M'm'K} C^{LlJ}_{MmK} \int\int d\boldsymbol{\rho}_1 d\boldsymbol{r}_1 \psi^*_{\alpha'}(\boldsymbol{r}_1) U_{11} \psi_\alpha(\boldsymbol{r}_1) \times \frac{F_{L'}(\eta',q_{\alpha'}\rho_1)}{q_{\alpha'}\rho_1} Y^*_{L'M'}(\widehat{\boldsymbol{\rho}}_1) \frac{F_L(\eta,q_\alpha\rho_1)}{q_\alpha\rho_1} Y_{LM}(\widehat{\boldsymbol{\rho}}_2). \tag{2.46}$$

Using the approximation $\boldsymbol{r}_3 \approx \boldsymbol{\rho}_1$ (atomic c.m. assumed to be at the target nucleus) and expanding

$$U_{11} =v_3 + v_2 - U_1 = \frac{Z}{r_3} - \frac{1}{r_2} - \frac{Z-1}{\rho_1} = \frac{1}{\rho_1} - \frac{1}{r_2}, \tag{2.47}$$

in partial waves we get

$$U_{11} = 4\pi \sum_{\lambda\mu} (2\lambda+1)^{-1} \mathcal{U}^\lambda_{11}(\rho_1,r_1) Y^*_{\lambda\mu}(\widehat{\boldsymbol{\rho}}_1) Y_{\lambda\mu}(\widehat{\boldsymbol{r}}_1), \tag{2.48}$$

where

$$\mathcal{U}^\lambda_{11}(\rho_1,r_1) = \begin{cases} \frac{\delta_{\lambda 0}}{\rho_1} - \frac{\rho_1^\lambda}{r_1^{\lambda+1}} & \text{if } \rho_1 < r_1 \\ \frac{\delta_{\lambda 0}}{\rho_1} - \frac{r_1^\lambda}{\rho_1^{\lambda+1}} & \text{otherwise} \end{cases} . \tag{2.49}$$

It then follows that

$$\mathcal{V}^{L'L}_{\alpha'\alpha}(q_{\alpha'},q_\alpha) =\frac{(4\pi)^{5/2}}{q_{\alpha'}q_\alpha} i^{L-L'} \sum_{\substack{m',m,\\ M',M}} C^{L'l'J}_{M'm'K} C^{LlJ}_{MmK} \int_0^\infty d\rho_1 F_{L'}(\eta',q_{\alpha'}\rho_1) F_L(\eta,q_\alpha\rho_1) \times \int d\boldsymbol{r}_1 \psi^*_{\alpha'}(\boldsymbol{r}_1)\psi_\alpha(\boldsymbol{r}_1) \sum^{(2)}_\lambda \frac{[L']}{[L\lambda]} C^{L'\lambda L}_{M'\mu M} C^{L'\lambda L}_{000} \mathcal{U}^\lambda_{11}(\rho_1,r_1) Y_{\lambda\mu}(\widehat{\boldsymbol{r}}_1), \tag{2.50}$$

where $[l] = \sqrt{2l+1}$ and $\mu = M - M'$. We take the configuration-space bound state wavefunction in the form $\psi_\alpha(\boldsymbol{r}_1) = i^l R_{nl}(r_1) Y_{lm}(\widehat{\boldsymbol{r}}_1)$, with $R_{nl}(r_1)$ being the square-integrable radial part. Then we obtain

$$\mathcal{V}^{L'L}_{\alpha'\alpha}(q_{\alpha'},q_\alpha) =(4\pi)^2 i^{L-L'+l-l'} \sum_{\substack{m',m,\\ M',M}} C^{L'l'J}_{M'm'K} C^{LlJ}_{MmK} \sum^{(2)}_\lambda \frac{[L']}{[L]} C^{L'\lambda L}_{M'\mu M} C^{L'\lambda L}_{000} \frac{[l]}{[l']} \times C^{l\lambda l'}_{m\mu m'} C^{l\lambda l'}_{000} I^\lambda_{\alpha'\alpha}(q_{\alpha'},q_\alpha), \tag{2.51}$$

where all radial information is contained in the integral

$$I^{\lambda}_{\alpha'\alpha}(q_{\alpha'},q_{\alpha}) = \frac{1}{q_{\alpha'}q_{\alpha}}\int_0^{\infty} d\rho_1 F_{L'}(\eta',q_{\alpha'}\rho_1)F_L(\eta,q_{\alpha}\rho_1) \times \int_0^{\infty} dr_1 r_1^2 R_{n'l'}(r_1)\,\mathcal{U}^{\lambda}_{11}(\rho_1,r_1)R_{nl}(r_1). \tag{2.52}$$

Summing over the angular momenta projections one finally arrives at

$$\mathcal{V}^{L'L}_{\alpha'\alpha}(q_{\alpha'},q_{\alpha}) = (4\pi)^2(-1)^{J+(L'+L+l'+l)/2}[L'l]\sum_{\lambda}{}^{(2)} C^{L'\lambda L}_{000}C^{l\lambda l'}_{000}\left\{\begin{array}{ccc} L' & \lambda & L \\ l & J & l' \end{array}\right\} \times I^{\lambda}_{\alpha'\alpha}(q_{\alpha'},q_{\alpha}), \tag{2.53}$$

where the braces denote a $6j$-symbol. Step 2 of the sum points to the fact that only the terms corresponding to λ of the same parity as the one of $l'+l$ (or, identically, of $L'+L$) survive.

Setting $Z=1$ and effectively $\eta'=\eta=0$ the radial integral reduces to

$$I^{\lambda}_{\alpha'\alpha}(q_{\alpha'},q_{\alpha}) = \int_0^{\infty} d\rho_1 \rho_1^2 j_{L'}(q_{\alpha'}\rho_1)j_L(q_{\alpha}\rho_1) \times \int_0^{\infty} dr_1 r_1^2 R_{n'l'}(r_1)\,\mathcal{U}^{\lambda}_{11}(\rho_1,r_1)R_{nl}(r_1), \tag{2.54}$$

which is the same as for e^+-H [109].

2.3.2 Direct Ps-Ps transitions

Effective potentials for $\beta\to\beta'$ transitions (Ps→Ps) are defined as

$$V_{\beta'\beta}(\boldsymbol{q}_{\beta'},\boldsymbol{q}_{\beta}) \equiv \langle \boldsymbol{q}_{\beta'}|\langle\psi_{\beta'}|U_{22}|\psi_{\beta}\rangle|\boldsymbol{q}_{\beta}\rangle = \int\int d\boldsymbol{\rho}_2 d\boldsymbol{r}_2 e^{-i\boldsymbol{q}_{\beta'}\boldsymbol{\rho}_2}\psi^*_{\beta'}(\boldsymbol{r}_2)U_{22}\psi_{\beta}(\boldsymbol{r}_2)e^{i\boldsymbol{q}_{\beta}\boldsymbol{\rho}_2}. \tag{2.55}$$

Repeating the procedure used in Section 2.3.1 we get

$$\mathcal{V}^{L'L}_{\beta'\beta}(q_{\beta'},q_{\beta}) = (4\pi)^2(-1)^{J+(L'+L+l'+l)/2}[L'l]\sum_{\lambda}{}^{(2)} C^{L'\lambda L}_{000}C^{l\lambda l'}_{000}\left\{\begin{array}{ccc} L' & \lambda & L \\ l & J & l' \end{array}\right\} \times I^{\lambda}_{\beta'\beta}(q_{\beta'},q_{\beta}), \tag{2.56}$$

where $I^{\lambda}_{\beta'\beta}(q_{\beta'}, q_{\beta})$ is the same as for neutral targets but with $\mathcal{U}^{\lambda}_{22}(\rho_2, r_2)$ in Eq. (2.54) defined as

$$\mathcal{U}^{\lambda}_{22}(\rho_2, r_2) = Z(1-(-1)^{\lambda}) \begin{cases} \frac{2^{\lambda+1}\rho_2^{\lambda}}{r_2^{\lambda+1}} & \text{if } \rho_2 < r_2/2 \\ \frac{r_2^{\lambda}}{2^{\lambda}\rho_2^{\lambda+1}} & \text{otherwise} \end{cases} \tag{2.57}$$

since

$$U_{22} \equiv \frac{Z}{r_3} - \frac{Z}{r_1} = \frac{Z}{|\boldsymbol{\rho}_2 + \boldsymbol{r}_2/2|} - \frac{Z}{|\boldsymbol{\rho}_2 - \boldsymbol{r}_2/2|}. \tag{2.58}$$

As Ps is neutral the only change when moving from a proton to He^{2+} is the charge Z.

2.3.3 Rearrangement

The effective potentials for the rearrangement transitions (e^++He^+ →He^{2+}+Ps) have an identical starting form to neutral atom→Ps transitions, except the incoming plane wave of the positron is replaced by the Coulomb wave function. It is convenient to perform the replacements $\boldsymbol{\rho}_2 \to -\boldsymbol{\rho}_2$ and $\boldsymbol{q}_{\beta} \to -\boldsymbol{q}_{\beta}$. Now vector $\boldsymbol{\rho}_2$ is the position and $\boldsymbol{q}_{\beta}$ is the momentum of positronium relative to the He^{2+} ion. With these changes the effective potentials for rearrangement read as

$$\begin{aligned} V_{\beta\alpha}(\boldsymbol{q}_{\beta}, \boldsymbol{q}_{\alpha}) \equiv & \langle \boldsymbol{q}_{\beta} | \langle \psi_{\beta} | U_{21} | \psi_{\alpha} \rangle | \boldsymbol{q}_{\alpha} \rangle \\ = & \int\int d\boldsymbol{\rho}_1 d\boldsymbol{r}_1 e^{-i\boldsymbol{q}_{\beta}\boldsymbol{\rho}_2} \psi^*_{\beta}(\boldsymbol{r}_2)(H_0 + v - E)\psi_{\alpha}(\boldsymbol{r}_1)\psi^{\mathrm{C}}_{\boldsymbol{q}_{\alpha},\eta}(\boldsymbol{\rho}_{\boldsymbol{1}}). \end{aligned} \tag{2.59}$$

Eq. (2.59) is split into two parts according to

$$\begin{aligned} V_{\beta\alpha}(\boldsymbol{q}_{\beta}, \boldsymbol{q}_{\alpha}) = & \int\int d\boldsymbol{\rho}_1 d\boldsymbol{r}_1 e^{-i\boldsymbol{q}_{\beta}\boldsymbol{\rho}_2} \psi^*_{\beta}(\boldsymbol{r}_2)(H_0 - E + v_1 + v_2)\psi_{\alpha}(\boldsymbol{r}_1)\psi^{\mathrm{C}}_{\boldsymbol{q}_{\alpha},\eta}(\boldsymbol{\rho}_{\boldsymbol{1}}) \\ & + \int\int d\boldsymbol{\rho}_1 d\boldsymbol{r}_1 e^{-i\boldsymbol{q}_{\beta}\boldsymbol{\rho}_2} \psi^*_{\beta}(\boldsymbol{r}_2) v_3 \psi_{\alpha}(\boldsymbol{r}_1)\psi^{\mathrm{C}}_{\boldsymbol{q}_{\alpha},\eta}(\boldsymbol{\rho}_{\boldsymbol{1}}) \\ = & V^{(I)}_{\beta\alpha}(\boldsymbol{q}_{\beta}, \boldsymbol{q}_{\alpha}) + V^{(II)}_{\beta\alpha}(\boldsymbol{q}_{\beta}, \boldsymbol{q}_{\alpha}). \end{aligned} \tag{2.60}$$

Then the first part can be written as

$$V^{(I)}_{\beta\alpha}(\boldsymbol{q}_\beta,\boldsymbol{q}_\alpha)=\int\frac{d\boldsymbol{q}}{(2\pi)^3}\widetilde{\psi}^{\rm C}_{\boldsymbol{q},\eta}(\boldsymbol{q})\left[\mathcal{E}(\boldsymbol{q}_\beta,\boldsymbol{q})\widetilde{\psi}^*_\beta(\boldsymbol{p}'_\beta)\widetilde{\psi}_\alpha(\boldsymbol{p}'_\alpha)-Z\widetilde{\psi}^*_\beta(\boldsymbol{p}'_\beta)\widetilde{g}_\alpha(\boldsymbol{p}'_\alpha)\right.$$
$$\left.-\widetilde{g}^*_\beta(\boldsymbol{p}'_\beta)\widetilde{\psi}_\alpha(\boldsymbol{p}'_\alpha)\right], \tag{2.61}$$

where $\mathcal{E}(\boldsymbol{q}_\beta,\boldsymbol{q})=q^2_\beta/4+p'^2_\beta-E\equiv q^2/2+p'^2_\alpha/2-E$,

$$\boldsymbol{p}'_\beta=\boldsymbol{q}_\beta/2-\boldsymbol{q}\quad\text{and}\quad\boldsymbol{p}'_\alpha=\boldsymbol{q}_\beta-\boldsymbol{q}, \tag{2.62}$$

and $\widetilde{\psi}^{\rm C}_{\boldsymbol{q},\eta}(\boldsymbol{q})$ is the Coulomb wavefunction in momentum space. The second term may be written as

$$V^{(II)}_{\beta\alpha}(\boldsymbol{q}_\beta,\boldsymbol{q}_\alpha)=\int\frac{d\boldsymbol{q}}{(2\pi)^3}Z\widetilde{g}^{\rm C}_{\boldsymbol{q}_\alpha,\eta}(\boldsymbol{q})\widetilde{\psi}^*_\beta(\boldsymbol{p}'_\beta)\widetilde{\psi}_\alpha(\boldsymbol{p}'_\alpha), \tag{2.63}$$

where $\widetilde{g}^{\rm C}_{\boldsymbol{q}_\alpha,\eta}(\boldsymbol{q})$ is Coulomb form factor in momentum space.

Transform $V^{(I)}_{\beta\alpha}(\boldsymbol{q}_\beta,\boldsymbol{q}_\alpha)$ into the representation of total angular momentum J according to Eq. (2.40). After then separating the radial parts of the momentum-space pseudostates and pseudo-form-factors according to $\widetilde{\psi}_\alpha(\boldsymbol{p})=\widetilde{R}_{nl}(p)Y_{lm}(\widehat{\boldsymbol{p}})$ and $\widetilde{g}_\alpha(\boldsymbol{p})=\widetilde{u}_{nl}(p)Y_{lm}(\widehat{\boldsymbol{p}})$ and using the following expansion for the Coulomb wavefunction

$$\widetilde{\psi}^{\rm C}_{\boldsymbol{q}_\alpha,\eta}(\boldsymbol{q})=2\pi\sum_{L''M''}Y^*_{L''M''}(\widehat{\boldsymbol{q}}_\alpha)Y_{L''M''}(\widehat{\boldsymbol{q}})\widetilde{\psi}^{\rm C}_{q_\alpha,\eta,L''}(q), \tag{2.64}$$

we get

$$\mathcal{V}^{L'L(I)}_{\beta\alpha}(q_\beta,q_\alpha)=\frac{1}{(2\pi)^2}\sum_{\substack{m',m,\\M',M}}C^{JK}_{L'M'l'm'}C^{JK}_{LMlm}\int_0^\infty dqq^2\widetilde{\psi}^{\rm C}_{q_\alpha,\eta,L}(q)$$
$$\times\int d\widehat{\boldsymbol{q}}_\beta\int d\widehat{\boldsymbol{q}}Y^*_{L'M'}(\widehat{\boldsymbol{q}}_\beta)Y_{LM}(\widehat{\boldsymbol{q}})Y^*_{l'm'}(\widehat{\boldsymbol{p}'}_\beta)Y_{lm}(\widehat{\boldsymbol{p}'_\alpha})$$
$$\times\left[\mathcal{E}(\boldsymbol{q}_\beta,\boldsymbol{q})\widetilde{R}^*_{n'l'}(p'_\beta)\widetilde{R}_{nl}(p'_\alpha)-Z\widetilde{R}^*_{n'l'}(p'_\beta)\widetilde{u}_{nl}(p'_\alpha)\right.$$
$$\left.-\widetilde{u}^*_{n'l'}(p'_\beta)\widetilde{R}_{nl}(p'_\alpha)\right]. \tag{2.65}$$

Decomposing the spherical harmonics of the direction of the relative motion in pairs α and β one gets

$$\begin{aligned}\mathcal{V}_{\beta\alpha}^{L'L(I)}(q_\beta,q_\alpha) =&\frac{1}{\pi}\sum_{\substack{m',m,\\M',M}} C^{JK}_{L'M'l'm'}C^{JK}_{LMlm}\int_0^\infty dqq^2\widetilde{\psi}^{\rm C}_{q_\alpha,\eta,L}(q)\sum_{l'_1,m'_1,m'_2} C^{l'm'}_{l'_1m'_1l'_2m'_2}\\ &\times\frac{[l'!]}{[l'_1!l'_2!]}q_\beta^{l'_1}(-q)^{l'_2}2^{-l'_1}\sum_{l_1,m_1,m_2}C^{lm}_{l_1m_1l_2m_2}\frac{[l!]}{[l_1!l_2!]}q_\beta^{l_1}(-q)^{l_2}\\ &\times\int\int d\widehat{\boldsymbol{q}}_\beta d\widehat{\boldsymbol{q}}Y^*_{L'M'}(\widehat{\boldsymbol{q}}_\beta)Y_{LM}(\widehat{\boldsymbol{q}})Y_{l_1m_1}(\widehat{\boldsymbol{q}}_\beta)Y^*_{l'_1m'_1}(\widehat{\boldsymbol{q}}_\beta)\\ &\times Y_{l_2m_2}(\widehat{\boldsymbol{q}})Y^*_{l'_2m'_2}(\widehat{\boldsymbol{q}})F^{(I)}(\boldsymbol{q}_\beta,\boldsymbol{q}).\end{aligned}\tag{2.66}$$

Here

$$F^I(\boldsymbol{q}_\beta,\boldsymbol{q}) =\mathcal{E}(\boldsymbol{q}_\beta,\boldsymbol{q})\frac{\widetilde{R}^*_{n'l'}(p'_\beta)\widetilde{R}_{nl}(p'_\alpha)}{p'^{l'}_\alpha p'^{l}_\alpha}-Z\frac{\widetilde{R}^*_{n'l'}(p'_\beta)\widetilde{u}_{nl}(p'_\alpha)}{p'^{l'}_\beta p'^{l}_\alpha}-\frac{\widetilde{u}^*_{n'l'}(p'_\beta)\widetilde{R}_{nl}(p'_\alpha)}{p'^{l'}_\beta p'^{l}_\alpha},\tag{2.67}$$

and $[l!]=\sqrt{[2l+1]!}$. Combining two spherical harmonics of the same relative motion in channels α and β, after some algebra we get

$$\begin{aligned}\mathcal{V}_{\beta\alpha}^{L'L(I)}(q_\beta,q_\alpha) =&\frac{1}{(2\pi)^2}\sum_{\substack{m',m,\\M',M}} C^{JK}_{L'M'l'm'}C^{JK}_{LMlm}\sum_{l'_1,m'_1,m'_2} C^{l'm'}_{l'_1m'_1l'_2m'_2}\frac{[l'!]}{[l'_1!l'_2!]}q_\beta^{l'_1}(-1)^{l'_2}2^{-l'_1}\\ &\times\sum_{l_1,m_1,m_2}C^{lm}_{l_1m_1l_2m_2}\frac{[l!]}{[l_1!l_2!]}q_\beta^{l_1}(-1)^{l_2}\sum_{l''_1m''_1}\frac{[l_1l'_1]}{[l''_1]}C^{l''_1m''_1}_{l_1m_1l'_1m'_1}C^{l''_10}_{l_10l'_10}\\ &\times\sum_{l''_2m''_2}\frac{[l_2l'_2]}{[l''_2]}C^{l''_2m''_2}_{l_2m_2l'_2m'_2}C^{l''_20}_{l_20l'_20}(-1)^{m'_2+m_1}\int_0^\infty dqq^{l_2+l'_2+2}\widetilde{\psi}^{\rm C}_{q_\alpha,\eta,L}(q)\\ &\times\int\int d\widehat{\boldsymbol{q}}_\beta d\widehat{\boldsymbol{q}}F^{(I)}(\boldsymbol{q}_\beta,\boldsymbol{q})Y^*_{L'M'}(\widehat{\boldsymbol{q}}_\beta)Y_{LM}(\widehat{\boldsymbol{q}})Y^*_{l''_1m''_1}(\widehat{\boldsymbol{q}}_\beta)Y_{l''_2m''_2}(\widehat{\boldsymbol{q}}).\end{aligned}\tag{2.68}$$

Now we expand $F^{(I)}(\boldsymbol{q}_\beta,\boldsymbol{q})$ as

$$F^{(I)}(\boldsymbol{q}_\beta,\boldsymbol{q})=2\pi\sum_{\lambda,\mu}\mathcal{F}^{(I)}_\lambda(q_\beta,q)Y^*_{\lambda\mu}(\widehat{\boldsymbol{q}}_\beta)Y_{\lambda\mu}(\widehat{\boldsymbol{q}}),\tag{2.69}$$

where the expansion coefficients are given by

$$\mathcal{F}^{(I)}_\lambda(q_\beta,q)=\int_{-1}^1 dzF^{(I)}(\boldsymbol{q}_\beta,\boldsymbol{q})P_\lambda(z),\tag{2.70}$$

and $z = \widehat{\boldsymbol{q}}_\beta.\widehat{\boldsymbol{q}}$.

Then integrating over the angular momenta we get

$$\begin{aligned}
\mathcal{V}^{L'L(I)}_{\beta\alpha}(q_\beta,q_\alpha) =& \frac{1}{8\pi^2}\sum_{\substack{m',m,\\ M',M}} C^{JK}_{L'M'l'm'}C^{JK}_{LMlm}\sum_{l'_1,m'_1,m'_2} C^{l'm'}_{l'_1m'_1l'_2m'_2}\frac{[l'!]}{[l'_1!l'_2!]}q_\beta^{l'_1}(-1)^{l'_2}2^{-l'_1}\\
&\times\sum_{l_1,m_1,m_2} C^{lm}_{l_1m_1l_2m_2}\frac{[l!]}{[l_1!l_2!]}q_\beta^{l_1}(-1)^{l_2}\sum_{l''_1m''_1}\frac{[l_1l'_1]}{[l''_1]}C^{l''_1m''_1}_{l_1m_1l'_1m'_1}C^{l''_10}_{l_10l'_10}\\
&\times\sum_{l''_2m''_2}\frac{[l_2l'_2]}{[l''_2]}C^{l''_2m''_2}_{l_2m_2l'_2m'_2}C^{l''_20}_{l_20l'_20}(-1)^{m_1+m''_1+m'_2+m''_2}\sum_{\lambda,\mu}\frac{[L'\lambda]}{[l''_1]}\frac{[L\lambda]}{[l''_2]}\\
&\times C^{l''_1m''_1}_{L'M'\lambda\mu}C^{l''_10}_{L'0\lambda0}C^{l''_2m''_2}_{LM\lambda\mu}C^{l''_20}_{L0\lambda0}\int_0^\infty dqq^{l_2+l'_2+2}\widetilde{\psi}^{\rm C}_{q_\alpha,\eta,L}(q)\mathcal{F}^{(I)}_\lambda(q_\beta,q)\\
=&\sum_{l'_1}\frac{[l'!]}{[l'_1!l'_2!]}q_\beta^{l'_1}2^{-l'_1-1}\sum_{l_1}\frac{[l!]}{[l_1!l_2!]}q_\beta^{l_1}\sum_{l''_1}\frac{[l_1l'_1]}{[l''_1]}C^{l''_10}_{l_10l'_10}\sum_{l''_2}\frac{[l_2l'_2]}{[l''_2]}\\
&\times C^{l''_20}_{l_20l'_20}\sum_\lambda\frac{[L'\lambda]}{[l''_1]}C^{l''_10}_{L'0\lambda0}\frac{[L\lambda]}{[l''_2]}C^{l''_20}_{L0\lambda0}I^{\lambda(I)}_{\beta,\alpha}(q_\beta,q_\alpha)\sum_{\substack{m',m,M',M,m'_1,m'_2,\\ m_1,m_2,m''_1,m''_2,\mu}}\\
&\times(-1)^{m_1+m''_1+m'_2+m''_2+l'_2+l_2}C^{JK}_{L'M'l'm'}C^{JK}_{LMlm}\\
&\times C^{l'm'}_{l'_1m'_1l'_2m'_2}C^{lm}_{l_1m_1l_2m_2}C^{l''_1m''_1}_{l_1m_1l'_1m'_1}C^{l''_2m''_2}_{l_2m_2l'_2m'_2}C^{l''_1m''_1}_{L'M'\lambda\mu}C^{l''_2m''_2}_{LM\lambda\mu},
\end{aligned}\tag{2.71}$$

where

$$I^{\lambda(I)}_{\beta,\alpha}(q_\beta,q_\alpha)=\frac{1}{(2\pi)^2}\int_0^\infty dqq^{l_2+l'_2+2}\widetilde{\psi}^{\rm C}_{q_\alpha,\eta,L}(q)\mathcal{F}^{(I)}_\lambda(q_\beta,q).\tag{2.72}$$

Summing over all projections of the angular momenta leads to

$$\begin{aligned}
\mathcal{V}^{L'L(I)}_{\beta\alpha}(q_\beta,q_\alpha) =&\frac{1}{4\pi^2}[l'lL'Ll'!l!](-1)^{J+L'}\sum_{l'_1}\frac{[l'_1l'_2]}{[l'_1!l'_2!]}2^{-l'_1-1}\sum_{l_1}\frac{[l_1l_2]}{[l_1!l_2!]}q_\beta^{l_1+l'_1}\sum_{l''_1}\\
&\times C^{l''_10}_{l_10l'_10}\sum_{l''_2}C^{l''_20}_{l_20l'_20}\sum_\lambda[\lambda]^2C^{l''_10}_{L'0\lambda0}C^{l''_20}_{L0\lambda0}\left\{\begin{array}{cccc} l_1 & l & J & l'\\ l_2 & L & L' & l'_1\\ l'_2 & l''_2 & \lambda & l''_1\end{array}\right\}\\
&\times I^{\lambda(I)}_{\beta,\alpha}(q_\beta,q_\alpha).
\end{aligned}\tag{2.73}$$

Next we transform $V^{(II)}_{\beta\alpha}(\boldsymbol{q}_\beta,\boldsymbol{q}_\alpha)$, i.e. we need to calculate

$$\mathcal{V}^{L'L(II)}_{\beta\alpha}(q_\beta,q_\alpha) = \frac{1}{(2\pi)^3}\sum_{\substack{m',m,\\ M',M}} C^{JK}_{L'M'l'm'}C^{JK}_{LMlm}\int\int d\widehat{\boldsymbol{q}}_\beta d\widehat{\boldsymbol{q}}_\alpha Y^*_{L'M'}(\widehat{\boldsymbol{q}}_\beta)Y_{LM}(\widehat{\boldsymbol{q}}_\alpha) \times \int d\boldsymbol{q} Z\widetilde{g}^{\rm C}_{\boldsymbol{q}_\alpha,\eta}(\boldsymbol{q})\widetilde{\psi}^*_\beta(\boldsymbol{p}'_\beta)\widetilde{\psi}_\alpha(\boldsymbol{p}'_\alpha). \tag{2.74}$$

Again, separating out the radial components of the momentum-space pseudostates and pseudo-form-factors and expanding the momentum-space Coulomb form factor according to

$$\widetilde{g}^{\rm C}_{\boldsymbol{q}_\alpha,\eta}(\boldsymbol{q}) = 2\pi\sum_{L''M''} Y^*_{L''M''}(\widehat{\boldsymbol{q}}_\alpha)Y_{L''M''}(\widehat{\boldsymbol{q}})\widetilde{u}^{\rm C}_{q_\alpha,\eta,L''}(q), \tag{2.75}$$

we get

$$\mathcal{V}^{L'L(II)}_{\beta\alpha}(q_\beta,q_\alpha) = \frac{1}{(2\pi)^2}\sum_{\substack{m',m,\\ M',M}} C^{JK}_{L'M'l'm'}C^{JK}_{LMlm}\int d\widehat{\boldsymbol{q}}_\beta\int d\widehat{\boldsymbol{q}}Y^*_{L'M'}(\widehat{\boldsymbol{q}}_\beta)Y_{LM}(\widehat{\boldsymbol{q}}) \times Y^*_{l'm'}(\widehat{\boldsymbol{p}'}_\beta)Y_{lm}(\widehat{\boldsymbol{p}'_\alpha})\int_0^\infty dq q^2\widetilde{u}^{\rm C}_{q_\alpha,\eta,L}(q)Z\widetilde{R}^*_{n'l'}(p'_\beta)\widetilde{R}_{nl}(p'_\alpha). \tag{2.76}$$

The latter has the same form as Eq. (2.65), the only differences being the partial-wave Coulomb wavefunction $\widetilde{\psi}^{\rm C}_{q_\alpha,\eta,L}(q)$ is replaced by the form factor $\widetilde{u}^{\rm C}_{q_\alpha,\eta,L}(q)$ and $F^{(II)}$ is given as

$$F^{II}(\boldsymbol{q}_\beta,\boldsymbol{q}) = Z\frac{\widetilde{R}^*_{n'l'}(p'_\beta)\widetilde{R}_{nl}(p'_\alpha)}{p'^{l'}_\alpha p'^{l}_\alpha}. \tag{2.77}$$

Combining all results together, for the rearrangement transitions we have

$$\mathcal{V}^{L'L(I)}_{\beta\alpha}(q_\beta,q_\alpha) = [l'lL'Ll'!l!](-1)^{J+L'}\sum_{l'_1}\frac{[l'_1l'_2]}{[l'_1!l'_2!]}2^{-l'_1-1}\sum_{l_1}\frac{[l_1l_2]}{[l_1!l_2!]}q_\beta^{l_1+l'_1}\sum_{l''_1}C^{l''_10}_{l_10l'_10} \times\sum_{l''_2}C^{l''_20}_{l_20l'_20}\sum_\lambda[\lambda]^2C^{l''_10}_{L'0\lambda0}C^{l''_20}_{L0\lambda0}\begin{Bmatrix} l_1 & l & J & l'\\ l_2 & L & L' & l'_1\\ l'_2 & l''_2 & \lambda & l''_1\end{Bmatrix} \times I^\lambda_{\beta\alpha}(q_\beta,q_\alpha), \tag{2.78}$$

where

$$I^{\lambda}_{\beta,\alpha}(q_\beta,q_\alpha) = \frac{1}{(2\pi)^2}\int_0^\infty dq q^{l_2'+l_2+2}\left[\widetilde{\psi}^{\rm C}_{q_\alpha,\eta,L}(q)\mathcal{F}^I_\lambda(q_\beta,q)+\widetilde{u}^{\rm C}_{q_\alpha,\eta,L}(q)\mathcal{F}^{II}_\lambda(q_\beta,q)\right]. \tag{2.79}$$

According to [125] the Coulomb wavefunction in partial waves is given by

$$\begin{aligned}\widetilde{\psi}^{\rm C}_{q_\alpha,\eta,L}(q) &= \int_{-1}^{+1} dz P_L(z)\widetilde{\psi}^{\rm C}_{\boldsymbol{q},\eta}(\boldsymbol{q}) \\ &= -\frac{4\pi e^{\pi\eta/2}}{qq_\alpha}\lim_{\gamma\to+0}\frac{d}{d\gamma}\left[\left[\frac{q^2-(q_\alpha+i\gamma)^2}{2qq_\alpha}\right]^{i\eta}(\zeta^2-1)^{-i\eta/2}Q_L^{i\eta}(\zeta)\right],\end{aligned} \tag{2.80}$$

where $\zeta = (q^2+q_\alpha^2+\gamma^2)/2qq_\alpha$. The Coulomb form factor has a similar form, however in this case there is no need for $-d/d\gamma$. The function $Q_L^{i\eta}$ is complex due to the phase factor $e^{i\sigma_L}$. Therefore, both $\widetilde{\psi}^{\rm C}_{q_\alpha,\eta,L}(q)$ and $\widetilde{u}^{\rm C}_{q_\alpha,\eta,L}(q)$ are complex similar to the Coulomb function in co-ordinate space. By ignoring this complex phase factor the equations can be solved using real arithmetic for both the rearrangement and the direct atom-atom transitions in Section 2.3.1.

If we set $Z=1$, and hence $\eta=0$, the Coulomb wave function becomes

$$\begin{aligned}\widetilde{\psi}^{\rm C}_{q_\alpha,0,L}(q) = &-4^2\pi\frac{\pi\delta(q\pm q_\alpha)}{(q\mp q_\alpha)^2}(L+1)\left[Q_{L+1}\left(\frac{q^2+q_\alpha^2}{2qq_\alpha}\right)\right. \\ &\left.-\left(\frac{q^2+q_\alpha^2}{2qq_\alpha}\right)Q_L\left(\frac{q^2+q_\alpha^2}{2qq_\alpha}\right)\right].\end{aligned} \tag{2.81}$$

At the same time the form factor becomes

$$\widetilde{u}^{\rm C}_{q_\alpha,0,L}(q) = \frac{4\pi}{qq_\alpha}Q_L\left(\frac{q^2+q_\alpha^2}{2qq_\alpha}\right). \tag{2.82}$$

Substituting this back into Eq. (2.79) gives

$$\begin{aligned} I^{\lambda}_{\beta,\alpha}(q_\beta,q_\alpha) =& \frac{-1}{\pi}\int_0^\infty dq q^{l_2'+l_2+2}\frac{4\pi\delta(q\pm q_\alpha)}{(q\mp q_\alpha)^2}(L+1) \\ & \times\left[Q_{L+1}\left(\frac{q^2+q_\alpha^2}{2qq_\alpha}\right)-\left(\frac{q^2+q_\alpha^2}{2qq_\alpha}\right)Q_L\left(\frac{q^2+q_\alpha^2}{2qq_\alpha}\right)\right]\mathcal{F}^I_\lambda(q_\beta,q) \\ & \times -\frac{q_2'^{+l_2+2}}{qq_\alpha}Q_L\left(\frac{q^2+q_\alpha^2}{2qq_\alpha}\right)\mathcal{F}^{II}_\lambda(q_\beta,q) \\ =& q_\alpha^{l_2'+l_2}\mathcal{F}^I_\lambda(q_\beta,q_\alpha)+\frac{1}{\pi q_\alpha}\int_0^\infty dq q^{l_2'+l_2+1}\times Q_L\left(\frac{q^2+q_\alpha^2}{2qq_\alpha}\right)\mathcal{F}^{II}_\lambda(q_\beta,q). \end{aligned} \tag{2.83}$$

Since $\lim_{x\to1} Q_{L+1}(x) - xQ_L(x) = -1/(L+1)$, this reduces to the result obtained for neutral targets [109].

2.4 Numerical methods

A useful feature of the CCC method is that the method for solving the set of coupled equations (2.39) is effectively independent of the target. The method used for hydrogen [109] can be applied to the helium ion provided the effective potentials given by Eqs. (2.53) (2.56) and (2.78) can be determined to high precision.

Rewrite Eq. (2.39) as

$$\begin{aligned} \mathcal{T}^{L'L}_{\gamma'\gamma}(q_{\gamma'},q_\gamma) =& \mathcal{V}^{L'L}_{\gamma'\gamma}(q_{\gamma'},q_\gamma)+\sum_{L''}\Bigg[\sum_{\gamma''}^{N_{\rm T}+N_{\rm Ps}}\mathcal{P}\int\frac{dq_{\gamma''}q_{\gamma''}^2}{(2\pi)^3}\mathcal{V}^{L'L''}_{\gamma'\gamma''}(q_{\gamma'},q_{\gamma''})\omega_{\gamma''}(q^2_{\gamma''}) \\ & \times\mathcal{T}^{L''L}_{\gamma''\gamma}(q_{\gamma''},q_\gamma)+i\pi\sum_{\gamma''}^{N^{(o)}}q^{(o)}_{\gamma''}\mathcal{V}^{L'L''}_{\gamma'\gamma''}(q_{\gamma'},q_{\gamma''})\mathcal{T}^{L''L}_{\gamma''\gamma}(q_{\gamma''},q_\gamma)\Bigg], \end{aligned} \tag{2.84}$$

where the $\mathcal{P}$ symbol indicates that the integral is of the principal value type,

$$\omega_{\gamma''}(q^2_{\gamma''}) = \left(E-\frac{q^2_{\gamma''}}{2M_{\gamma''}}-\epsilon_{\gamma''}\right)^{-1}, \tag{2.85}$$

is a real function, and $q^{(o)}_{\gamma''}$ is defined for $\gamma'' \leq N^{(o)} \leq (N_{\rm T} + N_{\rm Ps})$ for which

$$q^{(o)}_{\gamma''} = \sqrt{2M_{\gamma''}(E - \epsilon_{\gamma''})}, \tag{2.86}$$

is real. In this case the channel γ'' is called open. Channels for which $\epsilon_{\gamma''} \geq E$ are called closed channels.

We can solve our equations using real arithmetic by introducing the K-matrix as defined by

$$\mathcal{K}^{L'L}_{\gamma'\gamma}(q_{\gamma'}, q_\gamma) = \sum_{L''} \sum_{\gamma''}^{N^{(o)}} \mathcal{T}^{L''L}_{\gamma''\gamma}(q_{\gamma''}, q_\gamma)(\delta_{\gamma'',\gamma}\delta_{L'',L} + i\pi q^{(o)}_{\gamma''} \mathcal{K}^{L''L}_{\gamma''\gamma}(q^{(o)}_{\gamma'}, q_\gamma)). \tag{2.87}$$

With this definition Eq. (2.84) transforms to the following system of equations for the K-matrix amplitudes

$$\begin{aligned}\mathcal{K}^{L'L}_{\gamma'\gamma}(q_{\gamma'}, q_\gamma) =& \mathcal{V}^{L'L}_{\gamma'\gamma}(q_{\gamma'}, q_\gamma) + \sum_{L''} \sum_{\gamma''}^{N_{\rm T}+N_{\rm Ps}} \mathcal{P} \int \frac{dq_{\gamma''} q^2_{\gamma''}}{(2\pi)^3} \mathcal{V}^{L'L''}_{\gamma'\gamma''}(q_{\gamma'}, q_{\gamma''}) \mathcal{G}_{\gamma''\gamma}(q^2_{\gamma''}) \\ & \times \mathcal{K}^{L''L}_{\gamma''\gamma}(q_{\gamma''}, q_\gamma).\end{aligned} \tag{2.88}$$

This is solved using real arithmetic, and then the T matrix is obtained by solving the much smaller set of equations. Note that both the K and V matrix elements have the potential to be complex for certain solutions of Eq. (2.21). For positron scattering on neutral targets the solutions were always plane waves so this additional complexity never arose. For positron scattering on He^+, solutions for α channels contain Coulomb waves which have a complex phase factor $e^{i\sigma_L}$. Fortunately, for the integrand in Eq. (2.88) the inner products are complex conjugates. Therefore the complex phase factor may be trivially factored out the same way it is for direct scattering [122].

The numerical solution for the set of equations (2.88) is obtained using standard quadrature rules. The kernel of the equations containing the principal value integrals is discretised using a Gauss-Legendre quadrature. The problem

of channel-dependent singularities is overcome by using a unique quadrature in each channel containing the singularity. The accuracy of the integral in the sense of the principal value was ensured by using a subquadrature consisting of an even number of Gauss-Legendre points, symmetrically distributed in the immediate vicinity of the singular point. The procedure is similar to the widely used subtraction method with the subtraction being numerically zero. An analytic treatment of the Green's function has been very successful in allowing these sets of equations to be solved without singularities for e^+-H and $e^--\mathrm{He}^+$ scattering [126, 127]. Similar treatment should be equally applicable to $e^+-\mathrm{He}^+$ scattering, but this is for further investigation. For now, $e^+-\mathrm{He}^+$ scattering makes use of the numerical technique.

Due to the nonorthogonal nature of the two-centre expansion, the system of equations (2.88) is highly ill-conditioned. This makes the use of arbitrarily high basis sizes impossible.

Calculations of the effective potentials for the direct transitions, Eq. (2.53), require evaluation of the integrals in Eqs. (2.52) (2.54) (with β in place of α). These integrals can effectively be represented as a product of two one-dimensional integrals, which can be calculated to a desired accuracy by integrating out to 100 a.u. on a sufficiently fine radial mesh. For direct transitions, these matrix elements are relatively quick.

As shown in the preceding section, the positronium-formation matrix elements have the same coupling of 12 angular momenta as seen in e^++H scattering, leading to finite angular momentum sums and two-dimensional integrals. Compact analytical expressions for the momentum-space pseudostates and corresponding pseudo-form-factors derived in Ref. [109] are used in this approach as well. The main difference was the inclusion of the momentum-space Coulomb

wave function and its corresponding form factor. Both have compact analytical forms. For the wave function we make use of the Fortran code developed by Eremenko *et al.* [125]. However, the code was slightly altered to suit our needs, the most notable change being the removal of the complex phase factor. As it was the case in the previous Ps-formation calculations, this integral has a singularity at $q = q_\alpha$. However, unlike the logarithmic singularity from Q_L, this singularity is complex and arises from $\widetilde{\psi}^{\mathrm{C}}_{q_\alpha,\eta,L}$ and $\widetilde{u}^{\mathrm{C}}_{q_\alpha,\eta,L}$. Instead of having two separate integrals for the Coulomb wave function and form factor, it is preferable to relate the two together under one function as

$$\widetilde{\psi}^{\mathrm{C}}_{q_\alpha,\eta,L}(q) = -\frac{4\pi e^{\pi\eta/2}}{qq_\alpha}\lim_{\gamma\to+0}\frac{d}{d\gamma}\left[\left[\frac{q^2-(q_\alpha+i\gamma)^2}{2qq_\alpha}\right]^{i\eta}(\zeta^2-1)^{-i\eta/2}Q_L^{i\eta}(\zeta)\right], \tag{2.89}$$

$$\widetilde{u}^{\mathrm{C}}_{q_\alpha,\eta,L}(q) = \frac{4\pi e^{\pi\eta/2}}{qq_\alpha}\lim_{\gamma\to+0}\left[\left[\frac{q^2-(q_\alpha+i\gamma)^2}{2qq_\alpha}\right]^{i\eta}(\zeta^2-1)^{-i\eta/2}Q_L^{i\eta}(\zeta)\right]. \tag{2.90}$$

We can expand the derivative as follows

$$\begin{aligned}
&\frac{d}{d\gamma}\left[\left[\frac{q^2-(q_\alpha+i\gamma)^2}{2qq_\alpha}\right]^{i\eta}(\zeta^2-1)^{-i\eta/2}Q_L^{i\eta}(\zeta)\right] \\
&\quad= \left[\frac{q^2-(q_\alpha+i\gamma)^2}{2qq_\alpha}\right]^{i\eta}(\zeta^2-1)^{-i\eta/2} \\
&\qquad\times\left(\frac{2\eta q_\alpha}{q^2-(q_\alpha+i\gamma)^2}Q_L^{i\eta}(\zeta)+\gamma\left[\frac{i2\eta Q_L^{i\eta}(\zeta)}{q^2-(q_\alpha+i\gamma)^2}+\frac{Q_L^{i\eta+1}(\zeta)}{qq_\alpha(\zeta^2-1)^{1/2}}\right]\right).
\end{aligned} \tag{2.91}$$

The first term and the remaining terms have broadly similar behaviour, so when the limit $\gamma \to 0$ is taken only the first term survives. Therefore, we get

$$\widetilde{\psi}^{\mathrm{C}}_{q_\alpha,\eta,L}(q) = -\frac{4\pi e^{\pi\eta/2}}{qq_\alpha}\frac{2\eta q_\alpha}{q^2-q_\alpha^2}\left[\frac{q^2-(q_\alpha+i0)^2}{2qq_\alpha}\right]^{i\eta}(\zeta^2-1)^{-i\eta/2}Q_L^{i\eta}(\zeta) \tag{2.92}$$

$$\begin{aligned}
\widetilde{u}^{\mathrm{C}}_{q_\alpha,\eta,L}(q) &= \frac{4\pi e^{\pi\eta/2}}{qq_\alpha}\left[\frac{q^2-(q_\alpha+i0)^2}{2qq_\alpha}\right]^{i\eta}(\zeta^2-1)^{-i\eta/2}Q_L^{i\eta}(\zeta) \\
&= \frac{q_\alpha^2-q^2}{2\eta q_\alpha}\widetilde{\psi}^{\mathrm{C}}_{q_\alpha,\eta,L}(q).
\end{aligned} \tag{2.93}$$

Accordingly, Eq. (2.79) reduces to

$$I^{\lambda}_{\beta,\alpha}(q_\beta,q_\alpha) = \frac{1}{(2\pi)^2}\int_0^\infty dq q^{l_2'+l_2+2}\widetilde{\psi}^{\rm C}_{q_\alpha,\eta,L}(q)\left[\mathcal{F}^I_\lambda(q_\beta,q)+\frac{q_\alpha^2-q^2}{2\eta q_\alpha}\mathcal{F}^{II}_\lambda(q_\beta,q)\right], \tag{2.94}$$

leaving the function in a more compact form with the singularity in one part and the regular functions in the other. For handling the singularities we use a subtraction method similar to the one used by Mitroy [76]. Near the singularity the momentum-space Coulomb wave functions have the following form

$$\widetilde{\psi}^{\rm C}_{q_\alpha,\eta,L}(q) = -\frac{8\pi e^{-\pi\eta/2}}{q}\left[\frac{(q+q_\alpha)^2}{4qq_\alpha}\right]^L {\rm Im}(\mathcal{D}), \tag{2.95}$$

where

$$\mathcal{D} = \Gamma(1+i\eta)e^{-i\sigma_L}\frac{(q+q_\alpha)^{i\eta-1}}{(q-q_\alpha)^{i\eta+1}}{}_2F_1\left[-L,-i\eta-L,1-i\eta,\frac{(q-q_\alpha)^2}{(q+q_\alpha)^2}\right]. \tag{2.96}$$

The singular behaviour is contained within the term

$$\frac{(q+q_\alpha)^{i\eta-1}}{(q-q_\alpha)^{i\eta+1}}, \tag{2.97}$$

with the complex exponents introducing oscillations. As $q\to q_\alpha$ the hypergeometric and the $[(q+q_\alpha)^2/4qq_\alpha]^L$ terms tend to 1. Therefore ignoring these terms would make for a good subtracting function. E.g., the latter can be chosen to be

$$\widetilde{\psi}^{\rm Sub}_{q_\alpha,\eta,L}(q) = -\frac{8\pi e^{-\pi\eta/2}}{q}{\rm Im}\left[\Gamma(1+i\eta)e^{-i\sigma_L}\frac{(q+q_\alpha)^{i\eta-1}}{(q-q_\alpha)^{i\eta+1}}\right]. \tag{2.98}$$

Using this in Eq. (2.94) within some range from q_1 to q_2, where q_1 and q_2 are points in the vicinity just below and above the singularity q_α, we have

$$\begin{aligned} I^{\lambda}_{\beta,\alpha}(q_\beta,q_\alpha) =& \frac{1}{(2\pi)^2}\int_{q_1}^{q_2} dq\left[q^{l_2'+l_2+2}\widetilde{\psi}^{\rm C}_{q_\alpha,\eta,L}(q)\left[\mathcal{F}^I_\lambda(q_\beta,q)+\frac{q_\alpha^2-q^2}{2\eta q_\alpha}\mathcal{F}^{II}_\lambda(q_\beta,q)\right]\right. \\ & \left. -q_\alpha^{l_2'+l_2+1}q\widetilde{\psi}^{\rm Sub}_{q_\alpha,\eta,L}(q)\mathcal{F}^I_\lambda(q_\beta,q_\alpha)\right]+\mathcal{F}^I_\lambda(q_\beta,q_\alpha)\frac{q_\alpha^{l_2'+l_2+1}}{(2\pi)^2} \\ & \times\int_{q_1}^{q_2} dqq\widetilde{\psi}^{\rm Sub}_{q_\alpha,\eta,L}(q), \end{aligned} \tag{2.99}$$

where we can make use of

$$\begin{aligned}\int dqq\widetilde{\psi}^{\text{Sub}}_{q_\alpha,\eta,L}(q) =& -8\pi e^{-\pi\eta/2}\text{Im}\left[\Gamma(1+i\eta)e^{-i\sigma_L}\int dq\frac{(q+q_\alpha)^{i\eta-1}}{(q-q_\alpha)^{i\eta+1}}\right]\\ =& -8\pi e^{-\pi\eta/2}\text{Re}\left[\Gamma(1+i\eta)e^{-i\sigma_L}\frac{1}{2\eta q_\alpha}\left(\frac{q+q_\alpha}{q-q_\alpha}\right)^{i\eta}\right]. \quad (2.100)\end{aligned}$$

Due to the oscillatory nature of this function and how its phase depends on η, as the momentum of the incoming positron q_α decreases and η increases, the integrand becomes more oscillatory and harder to manage. It is also possible to further increase the accuracy of the subtraction for lower q_α values by including the 2nd term of the Taylor expansion for $\mathcal{F}^I_\lambda(q_\beta, q)$:

$$\begin{aligned}f_l(q) &\approx f_l(q_\alpha) + \frac{df_l(q)}{dq}\Delta q\\ &\approx f_l(q_\alpha) + \frac{f_l(q_2)-f_l(q_1)}{q_2-q_1}(q-q_\alpha), \quad (2.101)\end{aligned}$$

and making use of

$$\begin{aligned}\int dqq(q-q_\alpha)\widetilde{\psi}^{\text{Sub}}_{q_\alpha,\eta,L}(q) =& -8\pi e^{-\pi\eta/2}\text{Im}\left[\Gamma(1+i\eta)e^{-i\sigma_L}\int dq\frac{(q+q_\alpha)^{i\eta-1}}{(q-q_\alpha)^{i\eta}}\right]\\ =& -8\pi e^{-\pi\eta/2}\text{Im}\left[\Gamma(1+i\eta)e^{-i\sigma_L}\frac{1}{1-i\eta}\left(\frac{q+q_\alpha}{q-q_\alpha}\right)^{i\eta-1}\right.\\ &\left.\times\ {}_2F_1\left(1,1-i\eta,2-i\eta,\frac{q-q_\alpha}{q+q_\alpha}\right)\right]. \quad (2.102)\end{aligned}$$

However, even this extension starts to break down for sufficiently low values of q_α. Further expansions have the potential to introduce more numerical errors. Fortunately, for $\eta > 0$ as $\eta \to \infty$ the Coulomb wave function tends to zero at an exponential rate, so the contribution from these calculations become negligible and can, therefore, be ignored. Conversely, for $\eta < 0$, the subtraction method can generate more accurate results for higher $|\eta|$ values, but these do not tend to zero like before. So, for positron scattering on a positive ion the method above is viable for integrating over the singularity, for negative ions more work will be required for smaller q_α values, but the latter is not required in the present work.

2.5 Experimental observables

The main observables of interest for positron scattering experiments are angular differential cross sections (DCS) and integrated cross sections for various transitions. This includes elastic scattering, target excitation, ionisation and Ps-formation. All of these physical observables can be calculated from the scattering amplitudes, denoted as $f_{\gamma'\gamma}$.

The scattering amplitude for a particular transition is related to on-shell value of the corresponding T-matrix element. We obtain reduced $\mathcal{T}^{L'LJ}_{\gamma'\gamma}$-matrix elements, which depend on partial waves of total orbital angular momentum J, by solving equations (2.87-2.88) for various transitions of interest. In the collision frame, where the quantization axis is taken along the incident projectile direction, the relation between the scattering amplitude (from state γ to state γ' with magnetic sublevels m and m', respectively) and the reduced on-shell T-matrix element can be written as

$$\begin{aligned} f_{\gamma' m', \gamma m}(\theta, \phi) = & \frac{1}{\sqrt{4\pi}} \frac{1}{\sqrt{2l+1}} \sqrt{\frac{q_{\gamma'}}{q_\gamma}} \sum_{L', L, J} \sqrt{(2L+1)} C^{Jm}_{L' m - m' l' m'} C^{Jm}_{L0lm} \\ & \times \mathcal{T}^{L'LJ}_{\gamma'\gamma}(q_\gamma, q_{\gamma'}) Y_{L' m - m'}(\theta, \phi), \end{aligned} \tag{2.103}$$

where l, m and l', m' are the orbital momentum and its projection of the initial and final states, respectively. The initial and final linear momenta of the projectile are denoted by q_γ and $q_{\gamma'}$ with the corresponding orbital angular momenta given by L and L', respectively. Considering positron measurements performed in the scattering plane, we set $\phi = 0$.

Assuming that the initial target is not polarised, the angle-differential cross section is obtained by averaging over magnetic sublevels of the initial state orbital angular momentum l and summing over the magnetic sublevels of the

final-state orbital angular momentum

$$\sigma_{\gamma'\gamma}(\theta) = \frac{d\sigma}{d\Omega} = \sum_{mm'} |f_{\gamma' m', \gamma m}(\theta, 0)|^2. \tag{2.104}$$

From this the integrated cross section is calculated by integrating the corresponding angle-differential cross section over all scattering angles, i.e.,

$$\sigma_{\gamma'\gamma} = \int_0^\pi \sigma_{\gamma'\gamma}(\theta) \sin(\theta) d\theta. \tag{2.105}$$

By substituting Eq. (2.103) and (2.104) into Eq. (2.105) the above integral can be taken analytically and the integrated cross section can be directly calculated from the on-shell value of the reduced T-matrix element

$$\sigma_{\gamma'\gamma} = \frac{1}{4\pi(2l+1)} \frac{q_{\gamma'}}{q_\gamma} \sum_{J,L',L} (2J+1) |\mathcal{T}^{L'L}_{\gamma'\gamma}(q_\gamma, q_{\gamma'})|^2. \tag{2.106}$$

The grand total cross section σ_t is obtained by summing over the individual integrated cross sections for states included in the close-coupling expansion. The total ionisation cross section is calculated as a sum of the integrated cross sections for positive energy states (of both atom and Ps). The total Ps-formation cross section is calculated as a sum of cross sections for electron capture into Ps bound states.

2.6 Chapter summary

In this chapter we have presented the basic formalism of the two-centre CCC method applied to positron scattering on the singly-charged helium ion. The Schrödinger equation has been transformed into Lippmann-Schwinger integral equations in momentum-space for positron scattering on an arbitrary charged target. The effective potentials for these equations have been derived for He^+ as a target. They have been written in such a way that they can also be used

to calculate the effective potentials for H as a target. The calculation of the effective potentials for the direct transitions is relatively easy. The effective potentials for the rearrangement (Ps-formation) channels are more complicated to calculate but follow a similar structure to the positron-hydrogen case. The most significant change comes in the form of the momentum-space Coulomb wave function, the treatment of which has been given in detail. Numerical methods used in the formalism have been discussed.

Chapter 3

Antihydrogen formation

A potential process for the production of antihydrogen ($\bar{\mathrm{H}}$) involves the scattering of antiprotons ($\bar{p}$) on positronium (Ps)

$$\mathrm{Ps}(n_{\mathrm{Ps}}, l_{\mathrm{Ps}}) + \bar{p} \rightarrow \bar{\mathrm{H}}(n_{\bar{\mathrm{H}}}, l_{\bar{\mathrm{H}}}) + e^{-}. \tag{3.1}$$

This reaction lends itself to producing $\bar{\mathrm{H}}$ in a beam-like geometry. Also, the energy levels for the Ps and $\bar{\mathrm{H}}$ bound states are $-1/4n_{\mathrm{Ps}}^2$ and $-1/2n_{\bar{\mathrm{H}}}^2$ respectively, meaning that there will always be an exothermic channel available for $\bar{\mathrm{H}}$ production. This would imply that $\bar{\mathrm{H}}$ formation cross sections for this mechanism would increase as the Ps energy is lowered. Therefore, if near-zero energy Ps could be used for scattering on cold, trapped antiprotons, then the yield of cold $\bar{\mathrm{H}}$ would be enhanced. However, this kind of set-up poses significant technical challenges. It would be useful to have accurate scattering cross sections available for reaction (3.1) over a wide energy range, and for as many initial Ps and final $\bar{\mathrm{H}}$ states, as possible.

According to Wigner [111] the cross sections for such a process behave as $1/\sqrt{\varepsilon}$ as $\varepsilon \rightarrow 0$, where ε is the energy of the Ps projectile. However, owing to the degeneracy of the excited Ps and $\bar{\mathrm{H}}$ states this changes to a $1/\varepsilon$ behaviour near the reaction threshold [128, 129]. It would therefore be useful to be able

to express the cross sections for $\bar{\mathrm{H}}$ formation via reaction (3.1) as a simple algebraic function in terms of energy. For this the two-centre convergent close-coupling (CCC) method was used [109]. This method was originally developed for positron scattering on H. However, e^++H scattering is the time-reversed, charge conjugate equivalent of Ps-$\bar{p}$ scattering, so the method can be readily applied to $\bar{\mathrm{H}}$ formation. The equations presented in the previous chapter can be simplified to those in [109].

The results of the $\bar{\mathrm{H}}$-formation calculations are presented in two parts, the first considers Ps in the $n_{\mathrm{Ps}} = 1 - 3$ states [130, 131] and the second extending to include Ps in the $n_{\mathrm{Ps}} = 4 - 5$ states [132, 133]. The separation of these sets of results represents a slight change in the methodology, the details of which will be given in the proceeding sections.

3.1 $\mathbf{Ps}(n = 1 - 3) - \bar{p}$ results

A key feature of the CCC method is that as the size of the basis N is increased the solution of the underlying Lippmann-Schwinger equations should converge. However, the two-centre case is ill-conditioned, meaning that arbitrarily increasing the basis size on both centres is impossible without encountering numerical instabilities. Therefore, the convergence of the results must be checked for increasing N. The size of the basis for orbital angular momentum l is given by $N_l = N_0 - l$. This allows the basis size to be given in terms of two variables, N_0 and l_{max}.

When examining Ps($1s$)-H($1s$) for the zeroth partial wave convergence was found with $N_0 = 4$ and $l_{\mathrm{max}} = 2$ on both centres[110]. We have taken $l^{\mathrm{H}}_{\mathrm{max}} = 3$ and $l^{\mathrm{Ps}}_{\mathrm{max}} = 2$. This allows for the inclusion of all Ps($n \leq 3$) states and H($n \leq 4$) states. For the Laguerre-based pseudostates the fall-off parameters were fixed

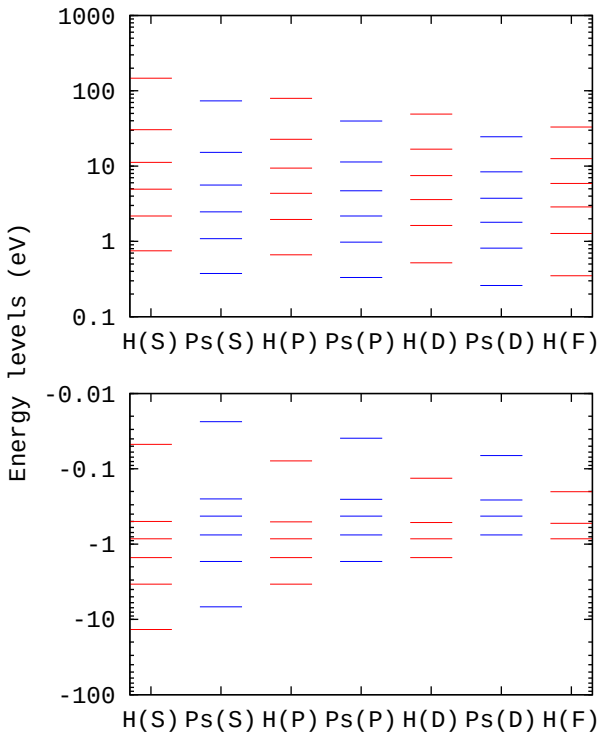

Figure 3.1: Energy levels of the positronium and hydrogen states used in the two-centre CCC calculations.

at $\lambda_l^{\mathrm{H}} = 1$ and $\lambda_l^{\mathrm{Ps}} = 0.5$ for all l. Results were found to be converged to within 5% across all energies for $N_0 = 12$, with the H and Ps states being accurate for $n \leq 5$. This level of convergence is verified in Section 3.2 where a different basis is used and excellent agreement is found between the two sets of results. The energies for these states are shown in Fig. 3.1. From the figure our choice of generating accurate H($n \leq 4$) states becomes more apparent. Due to the interplay between the Ps and H energy levels, for Ps($n = 3$) the H($n = 4$) states are open at zero energy.

The use of excited-state Ps scattering on protons opens up more H-formation channels. This results in many possible transitions, particularly at higher energies. To make the results more accessible we start by summing the H-formation cross sections and present them for each Ps initial state, as shown in Fig. 3.2.

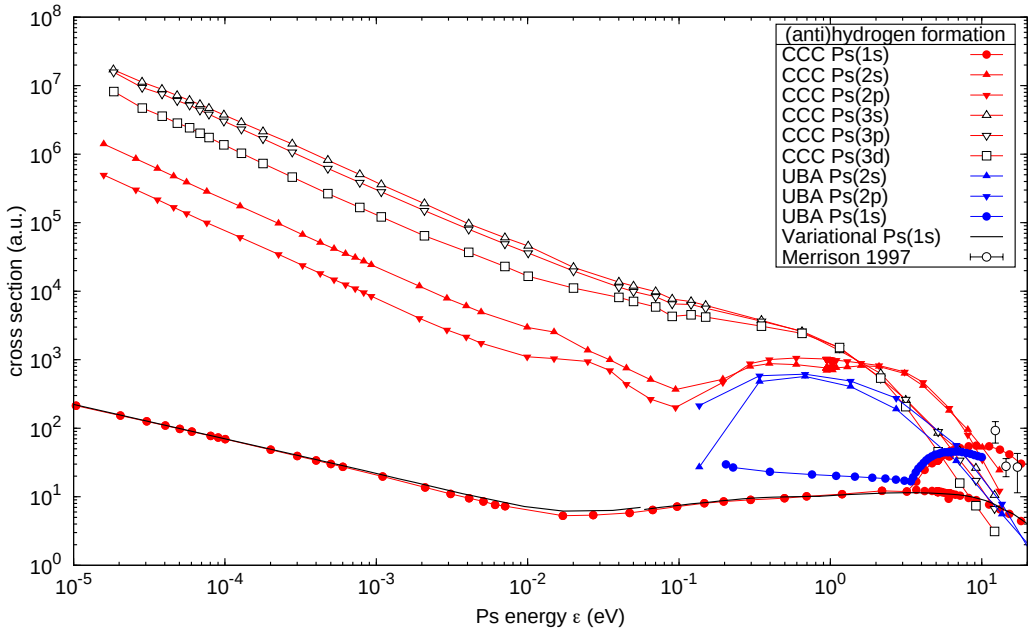

Figure 3.2: Total cross sections for positronium atoms, in the specified initial state nl, scattering on protons to form hydrogen calculated by using the CCC method; see the text. For Ps($1s$), the variational calculations [36, 38, 134] are for hydrogen formation in the $1s$ state only (CCC-calculated unconnected points presented for comparison above 3.4 eV), while the UBA calculations of Mitroy [87] and Mitroy and Stelbovics [86], and the CCC calculations generally, are for hydrogen formation in all open states. The three experimental points are due to Merrison *et al.* [135].

We also give comparison with some previous calculations and the only available experiment of Merrison *et al.* [135].

Beginning with the Ps($1s$) initial-state cross sections, one can see that this produces a relatively small amount of H. Here the only H state open at zero energy is H($1s$), with H($n = 2$) formation channels opening at 3.4 eV which can be seen from the sudden increase in the cross section at this point. For comparison across a wide range of energies we have the variational calculations of Humberston *et al.* [134]. These superseded those of Humberston *et al.* [36], though they had not be previously been published but kindly provided to us [38]. They only include formation of H($1s$). The unconnected points above 3.4

eV are the ground state H-formation cross sections for Ps($1s$) obtained using the CCC method. Agreement between the variational and the CCC results is excellent across the 6 orders of magnitude of incident energy. The connected points above 3.4 eV are the cross sections summed across all possible H states, including excited states, shown along with the unitarized Born approximation (UBA) results of Mitroy [87]. Inclusion of these states are necessary to achieve agreement with experiment. The UBA is a high energy approximation so it is unable to produce accurate results. However, the cross sections do exhibit similar structures to the CCC results, in particular, the rise associated with H($n = 2$) states being available for Ps($1s$) around 3.4 eV. The results are generally in good agreement with the experimental points of Merrison *et al.* [135], with better agreement being found for the higher energies, but with only 3 points available it is difficult to draw quantitative conclusions between experiment and theory.

When moving from Ps($1s$) to Ps($n = 2$) initial states we observe a several orders of magnitude increase in the cross sections. This indicates that the use of excited states of Ps with relatively slow antiprotons is a very promising proposition for antihydrogen formation. There are few calculations involving Ps($n > 1$) as projectiles[61, 69, 95], and none as far as we are aware extend to low energies of interest here. Mitroy and Stelbovics [86] and Mitroy [87] performed a large number of UBA calculations involving Ps($n \geq 4$) initial states to within 0.1 eV of threshold. This high-energy approximation is unable to yield accurate quantitative results but appears to yield some qualitative behaviour similar to the CCC results. In particular, a sharp increase in cross sections above 0.1 eV Ps energy, which is due to the opening up of $n_{\mathrm{H}} = 3$ states.

A further order-of-magnitude increase is observed when moving from Ps($n = 2$) to Ps($n = 3$). While not as big as the jump from Ps($1s$) to Ps($n = 2$), it does further validate the proposition for using excited Ps initial states as projectiles.

There are a few sources for the enhancement of the increase in the cross sections for increasing n_{Ps}. One source is the increased size and polarisability of the excited Ps states. A larger target means an interaction is more likely to occur and the decreased binding energy means the electron is more likely to break from the positron and bind with the proton. From Fig. 3.1, it can be seen that as n_{Ps} increases, excited states of H begin to open up. In addition, the energy differences between initial and final states decrease, making these transitions energetically more favourable. Along with these sources of enhancement, we can also observe a difference between the near-threshold behaviour for Ps in the ground state and in excited states. Ps($1s$) cross sections are expected to behave as $1/\sqrt{\varepsilon}$ as predicted by Wigner [111]. This was observed for the zeroth partial wave for Ps($1s$) scattering to form H($1s$) in Kadyrov *et al.* [110]. However, the excited states do not follow the same threshold behaviour. Due to the degeneracy of the excited states they behave as $1/\varepsilon$ as predicted by Fabrikant [128].

For both Ps($n = 2$) and Ps($n = 3$), the angular momentum of Ps appears to alter the magnitude of the cross sections, with cross sections increasing for decreasing l_{Ps}. Whether this effects the formation for specific H states formed is quite complex and will require a more detailed consideration.

The agreement between other calculations and the CCC results summed over the hydrogen states has been established. Now we present the cross sections for the H final states for each Ps initial state. When analysing the individual contributions of each final state we will focus on establishing simple formulas for low-energy data.

The data for (anti)hydrogen formation in the scattering of Ps($1s$) on (anti)-protons are presented in Fig. 3.3. In this case the only rearrangement channel open at threshold is the formation of H($1s$). The excited states of hydrogen do

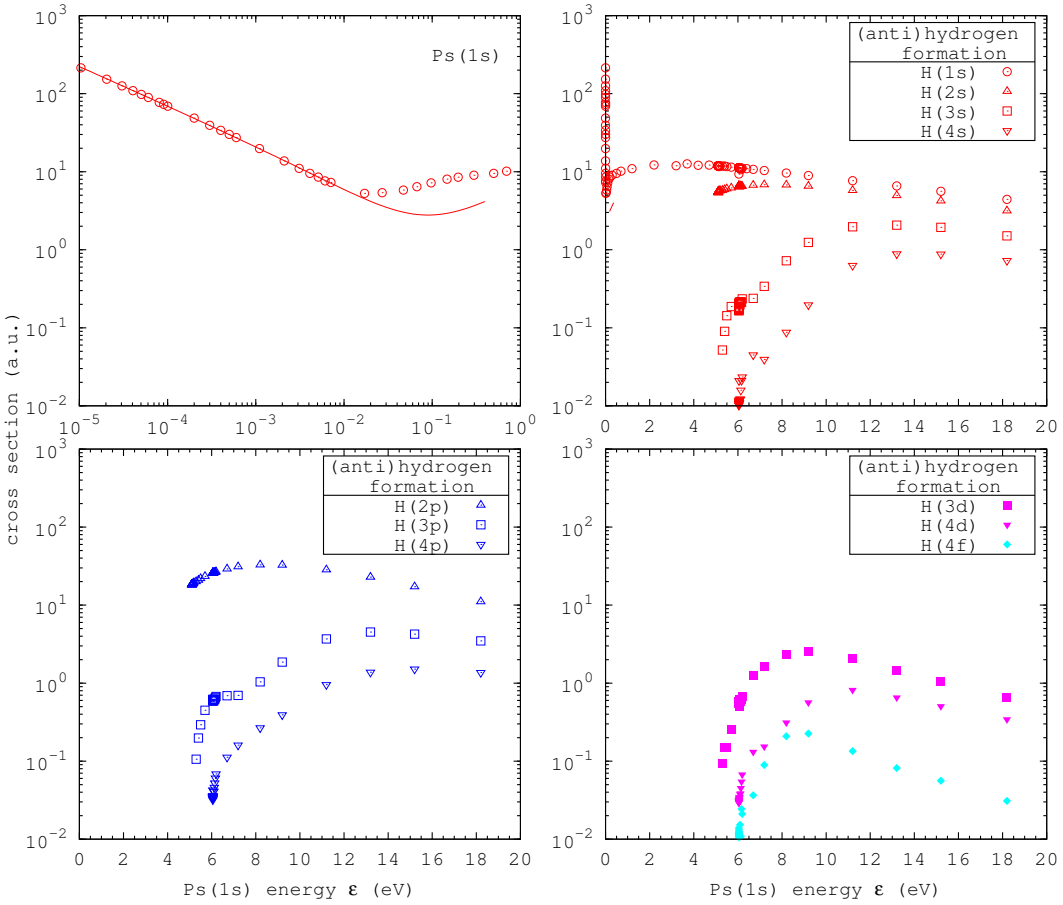

Figure 3.3: The cross sections for positronium in the $1s$ state scattering on (anti)protons to form (anti)hydrogen. The data presented are for transitions open at near-zero energies (top left), and then transitions across the full energy range of the calculation into s-states (top right), p-states (bottom left) and d- and f-states (bottom right). The solid line for the near-zero energy results is a least- squares fit of the data up to 0.01 eV (see text) with the fitting parameters given in table 3.1.

Table 3.1: Cross sections $\sigma_{\mathrm{H}(nl)} = \varepsilon^{-1/2}(a + b\varepsilon^{1/2} + c\varepsilon)$ (a.u.) for near-zero energy ε (eV) Ps($1s$) incident on (anti)protons, as shown by the solid line in figure 3.3. These values were obtained by a least-squares fit of the data up to 0.01 eV. The numbers in the square brackets indicates the power of 10.

	a	b	c
$\sigma_{\mathrm{H}(1s)}$	(7.087±0.034)[−1]	(−1.958±0.259)[+0]	(7.926±3.105)[+0]

not open up until around 3.4 eV Ps energy. According to Wigner [111], the cross sections for a reaction like this behave as $1/\sqrt{\varepsilon}$ where ε is the Ps energy. It may

be observed that the cross sections follow a noticeable trend up until around 0.01 eV where they start to rise again. Therefore we apply a least-squares fit to the function $\sigma_{\mathrm{H}(nl)} = \varepsilon^{-1/2}(a + b\varepsilon^{1/2} + c\varepsilon)$ from 0 to 0.01 eV, with the values a, b and c given in table 3.1 along with their related errors. From the table it can observed that the coefficients and their relative error increases from left to right, implying that this approximation is valid strictly at very low energies. This fitted function is represented by the solid line over the data points in Fig. 3.3.

Whereas the formation of H($1s$) is exothermic, the formation of any excited states of H using Ps($1s$) is endothermic. Therefore, these cross sections start at zero, rapidly growing to a maximum value and then slowly begin to drop off. These values are expected to smoothly vary as a function of energy, however some outlying points do appear around the 6-8 eV region (where the H($n = 4$) formation channel becomes open). This is a manifestation of the ill-conditioned nature of the problem and not a representation of a physical process. Using smaller values of N_0 produces data with fewer examples of this behaviour but exhibit somewhat greater pseudoresonance structure.

The data for Ps($2s$) scattering is presented in Fig. 3.4. For Ps($n = 2$) the channels for H($n \leq 2$) are open at threshold. For H($1s$) formation it can be seen that by changing from Ps($1s$) to Ps($2s$) has increased the cross sections by over an order of magnitude. Although this process is overtaken by H($n = 2$) formation which is 2 orders of magnitude larger for both H($2s$) and H($2p$). The immense enhancement may be attributed to a few sources: (i) the increased size and polarizability of the Ps and H states, (ii) the reduced energy difference between the initial Ps and final H state, and (iii) the emergence of the $1/\varepsilon$ threshold behaviour. Accordingly, the solid lines in Fig. 3.4 are the least-squares fit of the function $\sigma_{\mathrm{H}(nl)} = \varepsilon^{-1}(a + b\varepsilon + c\varepsilon^2)$ to the data from zero to 0.1 eV,

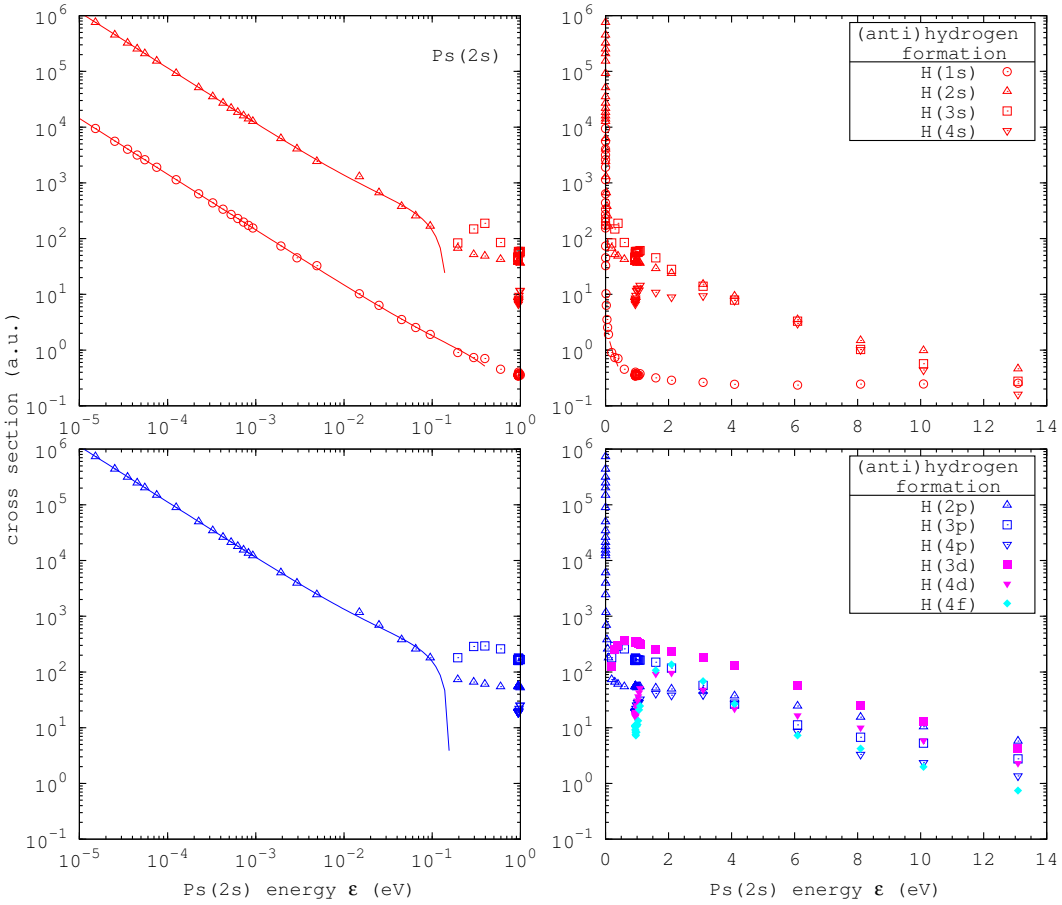

Figure 3.4: The cross sections for positronium in the $2s$ state scattering on (anti)protons to form (anti)hydrogen. The left-side data are for scattering at near-zero energies for formation of hydrogen in an s (top) or p state (bottom). The right-side data are across a larger energy range for formation in s (top) or p, d or f states (bottom). The solid lines for the near-zero energy results are the least-squares fits of the data up to 0.1 eV with the fitting parameters given in table 3.2.

with the fitting coefficients and their related errors given in Table. 3.2. From the table it can observed that the coefficients and their relative error increases from left to right, implying that this approximation is valid strictly at very low energies.

The data for Ps($2p$) scattering is shown in Fig. 3.5. The differences between the Ps($2s$) and Ps($2p$) results are mainly quantitative, with the Ps($2s$) cross sections being around 3 times larger than the Ps($2p$) cross sections. The overall

Table 3.2: Cross sections $\sigma_{\mathrm{H}(nl)} = \varepsilon^{-1}(a + b\varepsilon + c\varepsilon^2)$ (a.u.) for near-zero energy ε (eV) Ps($2s$) incident on (anti)protons, as shown by the solid lines in figure 3.4. These values were obtained by a least-squares fit of the data up to 0.1 eV. The numbers in the square brackets indicates the power of 10.

	a	b	c
$\sigma_{\mathrm{H}(1s)}$	(1.429±0.012)[−1]	(4.528±1.476)[−1]	(−7.623±17.660)[−1]
$\sigma_{\mathrm{H}(2s)}$	(1.154±0.028)[+1]	(2.452±0.347)[+2]	(−2.197±0.416)[+3]
$\sigma_{\mathrm{H}(2p)}$	(1.120±0.022)[+1]	(2.417±0.277)[+2]	(−1.992±0.331)[+3]

Table 3.3: Cross sections $\sigma_{\mathrm{H}(nl)} = \varepsilon^{-1}(a + b\varepsilon + c\varepsilon^2)$ (a.u.) for near-zero energy ε (eV) Ps($2p$) incident on (anti)protons, as shown by the solid lines in figure 3.5. These values were obtained by a least-squares fit of the data up to 0.1 eV. The numbers in the square brackets indicates the power of 10.

	a	b	c
$\sigma_{\mathrm{H}(1s)}$	(4.927±0.041)[−2]	(6.586±0.514)[−1]	(−3.663±0.616)[+0]
$\sigma_{\mathrm{H}(2s)}$	(3.849±0.242)[+0]	(2.215±0.304)[+2]	(−1.953±0.363)[+3]
$\sigma_{\mathrm{H}(2p)}$	(3.772±0.207)[+0]	(2.672±0.260)[+2]	(−2.188±0.311)[+3]

cross sections are somewhat smaller for Ps($2p$) in the low-energy region, as can be seen when the coefficients from tables 3.2 and 3.3 are compared. Thus, the overall qualitative behaviour for the Ps($n = 2$) initial states appear quite similar, with the newly available degenerate $n = 2$ states being the dominating factor.

The results for Ps($n = 3$) are considerably more complicated, with the potential for formation of H($n \leq 4$) open at threshold. In all cases the behaviour of the cross sections at the threshold follow the $1/\varepsilon$ relationship as found in Ps($n = 2$) scattering. We begin with Ps($3s$) given in Fig. 3.6 with the coefficients for the fitting functions and their related errors shown in Table. 3.4. From the table it can observed that the coefficients and their relative error increases from left to right, implying that this approximation is valid strictly at very low energies. We see that the largest contribution is due to H($n = 4$) formation, being an order-of-magnitude larger than the largest cross sections for Ps($n = 2$). This is to be expected since the difference between the Ps($n = 3$) and H($n = 4$)

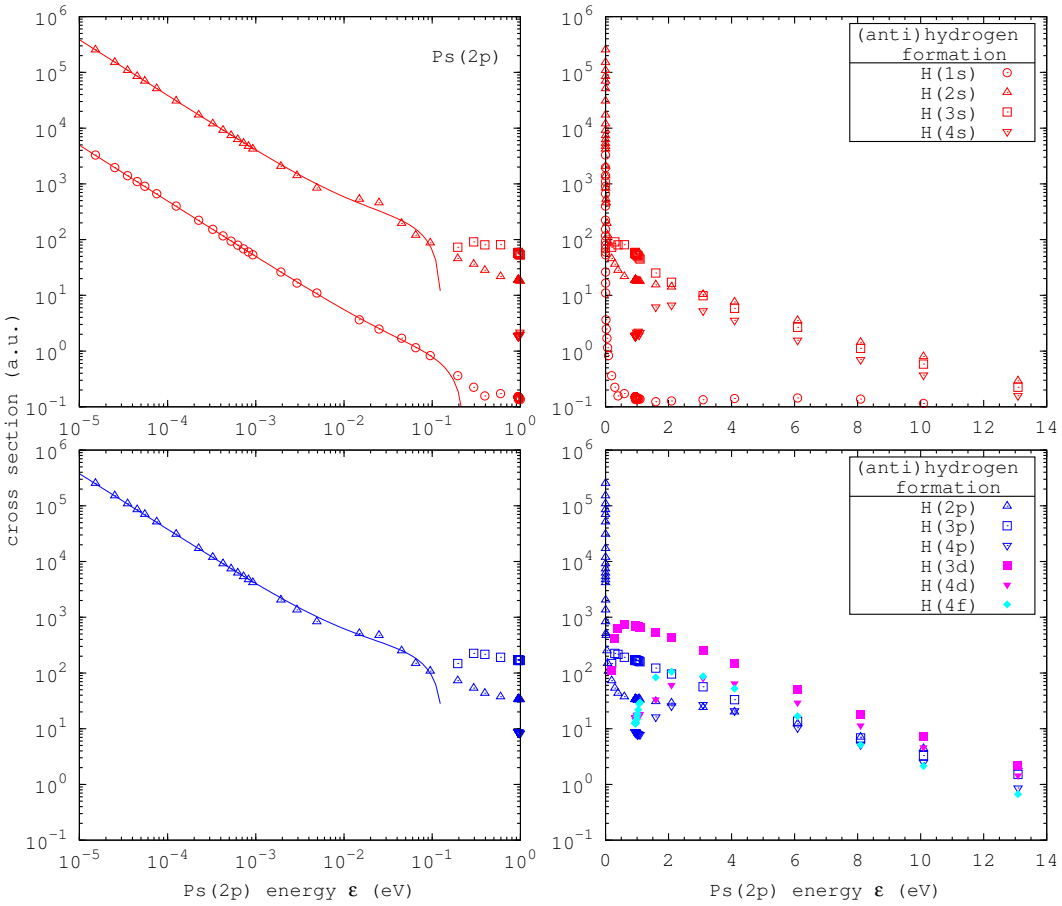

Figure 3.5: The cross sections for positronium in the $2p$ state scattering on (anti)protons to form (anti)hydrogen. The left-side data are for scattering at near-zero energies for formation of hydrogen in an s (top) or p state (bottom). The right-side data are across a larger energy range for formation in s (top) or p, d or f states (bottom). The solid lines for the near-zero energy results are the least-squares fits of the data up to 0.1 eV with the fitting parameters given in table 3.3.

energy levels is marginal. This small difference contributes to the enhancement of the cross sections and so do the increased size and polarizability of the incident Ps. The differences between the H($n = 4$) states are mostly quantitative, with the H($4s$) cross sections being slightly lower than the others. Interestingly, the other three H($n = 4$) states are almost indistinguishable, as can be seen in Table. 3.4. For each orbital angular momentum of H, the cross sections appear to drop an order of magnitude for decreasing values of n_{H}. In each case the formulas

Table 3.4: Cross sections $\sigma_{\mathrm{H}(nl)} = \varepsilon^{-1}(a + b\varepsilon + c\varepsilon^2)$ (a.u.) for near-zero energy ε (eV) Ps($3s$) incident on (anti)protons, as shown by the solid lines in figure 3.6. These values were obtained by a least-squares fit of the data up to 0.1 eV. The numbers in the square brackets indicates the power of 10.

	a	b	c
$\sigma_{\mathrm{H}(1s)}$	(7.724±0.236)[−3]	(−4.788±2.904)[−2]	(7.442±3.703)[−1]
$\sigma_{\mathrm{H}(2s)}$	(3.218±0.136)[−1]	(3.566±1.669)[+0]	(−2.728±2.129)[+1]
$\sigma_{\mathrm{H}(2p)}$	(4.437±0.121)[−1]	(1.026±1.485)[+0]	(1.584±1.894)[+1]
$\sigma_{\mathrm{H}(3s)}$	(5.220±0.201)[+0]	(4.519±2.468)[+1]	(−4.769±3.148)[+2]
$\sigma_{\mathrm{H}(3p)}$	(8.626±0.253)[+0]	(1.066±0.312)[+2]	(−1.310±0.398)[+3]
$\sigma_{\mathrm{H}(3d)}$	(3.664±0.125)[+0]	(4.252±1.539)[+1]	(−2.182±1.962)[+2]
$\sigma_{\mathrm{H}(4s)}$	(3.892±0.107)[+1]	(−2.019±1.314)[+2]	(4.573±1.675)[+3]
$\sigma_{\mathrm{H}(4p)}$	(1.178±0.012)[+2]	(−7.584±1.499)[+2]	(1.164±0.191)[+4]
$\sigma_{\mathrm{H}(4d)}$	(1.097±0.019)[+2]	(1.235±0.232)[+3]	(−1.174±0.296)[+4]
$\sigma_{\mathrm{H}(4f)}$	(8.713±0.256)[+1]	(1.650±0.315)[+3]	(1.167±0.401)[+4]

were fitted to the data up to 0.1 eV and are valid strictly at the threshold.

For Ps($3p$) scattering the results are given in Fig. 3.7 with the coefficients for the fitting functions and their related errors given in Table. 3.5. Qualitatively, the results are much the same as for Ps($3s$). Quantitatively, we can find that there is a slight drop in cross sections, which can be readily observed when comparing the a coefficients from the corresponding tables.

Finally, for Ps($3d$) initial state the results are presented in Fig. 3.8 with the corresponding formulas from least-squares fits given in Table. 3.6. Again, the results are qualitatively similar to the other $n_{\mathrm{Ps}} = 3$ cross sections. Although, quantitatively the results are somewhat lower in magnitude, as can be seen when comparing the a coefficients from the corresponding tables.

This completes the presentation of Ps($n \leq 3$) scattering on protons to form H($n \leq 4$) for low energies of interest to experiment. It is clear that initial Ps and final H states of nearly matching energies yielded the largest cross sections. It would be beneficial to examine this trend for larger values of n_{Ps}, in particular

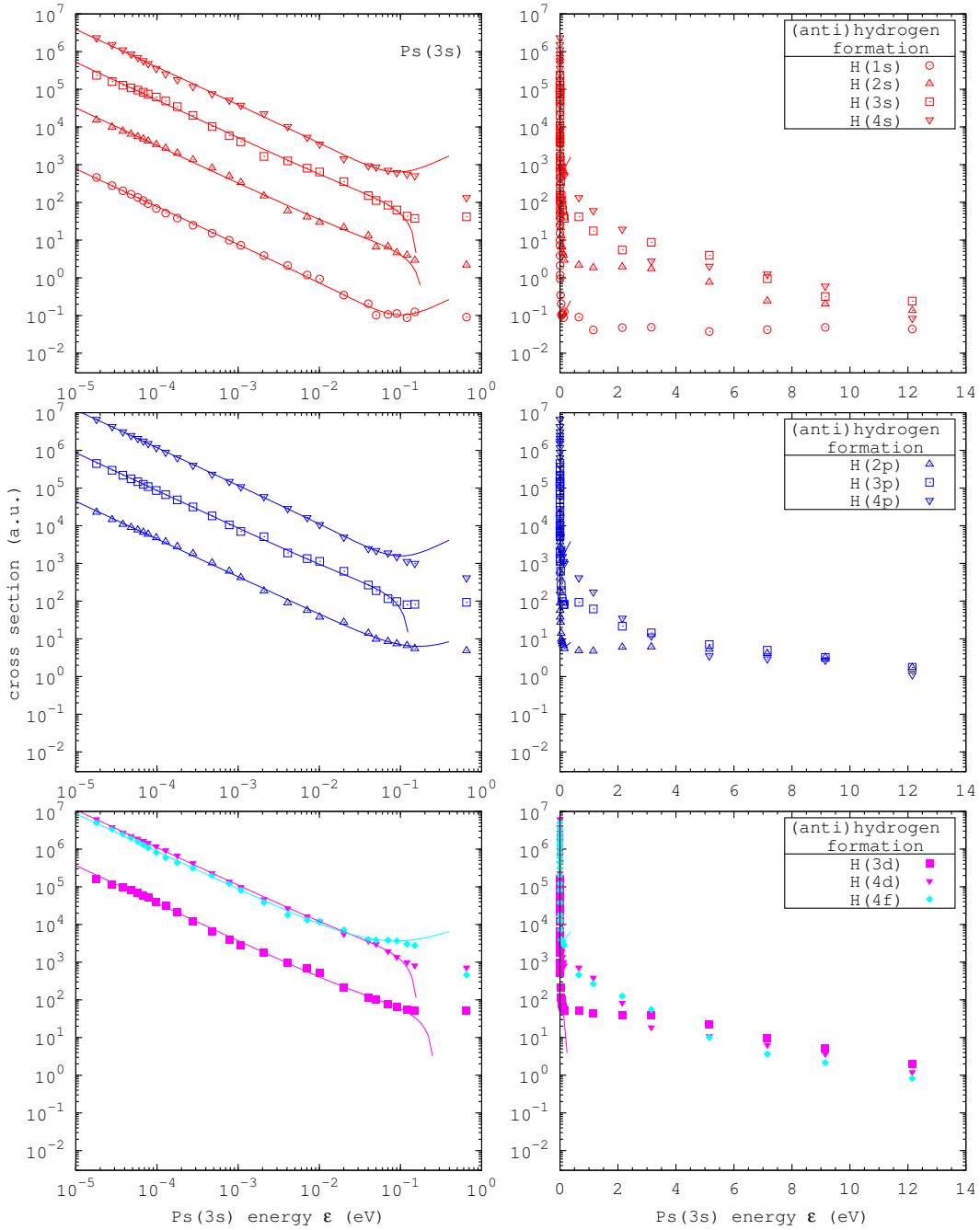

Figure 3.6: The cross sections for positronium in the $3s$ state scattering on (anti)protons to form (anti)hydrogen. The left-side data are for scattering at near-zero energies for formation of hydrogen in s (top), p (middle) d or f states (bottom). The right-side data are across a larger energy range. The solid lines for the near zero-energy results are the least-squares fits to the data up to 0.1 eV with the fitting parameters given in table 3.4.

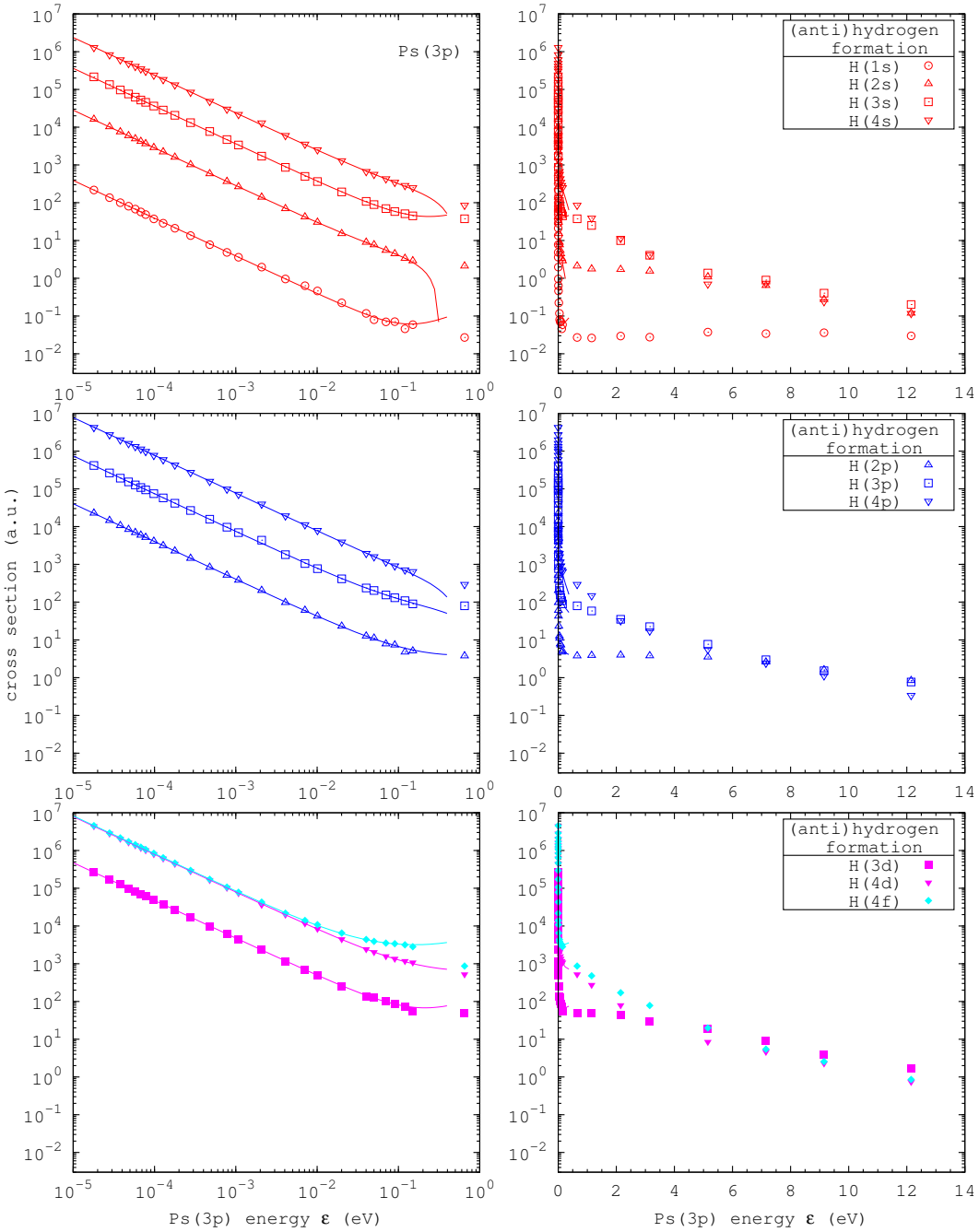

Figure 3.7: The cross sections for positronium in the $3p$ state scattering on (anti)protons to form (anti)hydrogen. The left-side data are for scattering at near-zero energies for formation of hydrogen in s (top), p (middle) d or f states (bottom). The right-side data are across a larger energy range. The solid lines for the near zero-energy results are the least-squares fits to the data up to 0.1 eV with the fitting parameters given in table 3.5.

Table 3.5: Cross sections $\sigma_{\mathrm{H}(nl)} = \varepsilon^{-1}(a + b\varepsilon + c\varepsilon^2)$ (a.u.) for near-zero energy ε (eV) Ps($3p$) incident on (anti)protons, as shown by the solid lines in figure 3.7. These values were obtained by a least-squares fit of the data up to 0.1 eV. The numbers in the square brackets indicates the power of 10.

	a	b	c
$\sigma_{\mathrm{H}(1s)}$	(3.892±0.078)[−3]	(5.562±9.596)[−3]	(1.994±1.224)[−1]
$\sigma_{\mathrm{H}(2s)}$	(2.829±0.016)[−1]	(2.184±0.202)[+0]	(−9.661±2.570)[+0]
$\sigma_{\mathrm{H}(2p)}$	(4.027±0.031)[−1]	(2.522±0.378)[+0]	(1.377±4.825)[+0]
$\sigma_{\mathrm{H}(3s)}$	(3.628±0.025)[+0]	(1.289±0.304)[+1]	(6.323±3.882)[+1]
$\sigma_{\mathrm{H}(3p)}$	(7.433±0.092)[+0]	(5.333±1.134)[+1]	(−5.490±14.460)[+1]
$\sigma_{\mathrm{H}(3d)}$	(4.759±0.030)[+0]	(2.311±0.365)[+1]	(1.052±0.466)[+2]
$\sigma_{\mathrm{H}(4s)}$	(2.382±0.021)[+1]	(1.104±0.253)[+2]	(−3.021±3.225)[+2]
$\sigma_{\mathrm{H}(4p)}$	(7.705±0.039)[+1]	(8.548±4.748)[+1]	(−3.670±6.055)[+2]
$\sigma_{\mathrm{H}(4d)}$	(7.906±0.031)[+1]	(4.618±0.386)[+2]	(1.262±4.925)[+2]
$\sigma_{\mathrm{H}(4f)}$	(8.257±0.050)[+1]	(2.160±0.061)[+3]	(3.257±0.781)[+3]

$n_{\mathrm{Ps}} = 5$. For these states, H($n = 7$) formation channels are open at zero Ps energy with the energy difference between the initial and final states being very small, and should therefore yield particularly large cross sections. However, increasing the number of states to include higher $l_{\max}$ on both centres makes the calculations difficult to manage. The presented results have minimal outliers, but the ill-conditioning is expected to get worse for increasing $l_{\max}$ and N_0 on both centres. For this reason a different approach is used for higher values of n_{Ps} as described in the next subsection.

While these results by themselves seem very promising, we have not taken into account the other processes open for these energy values. For this Fabrikant *et al.* [136] has examined elastic and quasi-elastic scattering of Ps on p and observed some interesting features, such as how the cross sections for these interactions are substantially larger than those predicted by the classical CTMC simulations [137]. Potential heating effects due to these elastic and quasi-elastic scattering have been explored by Charlton *et al.* [138].

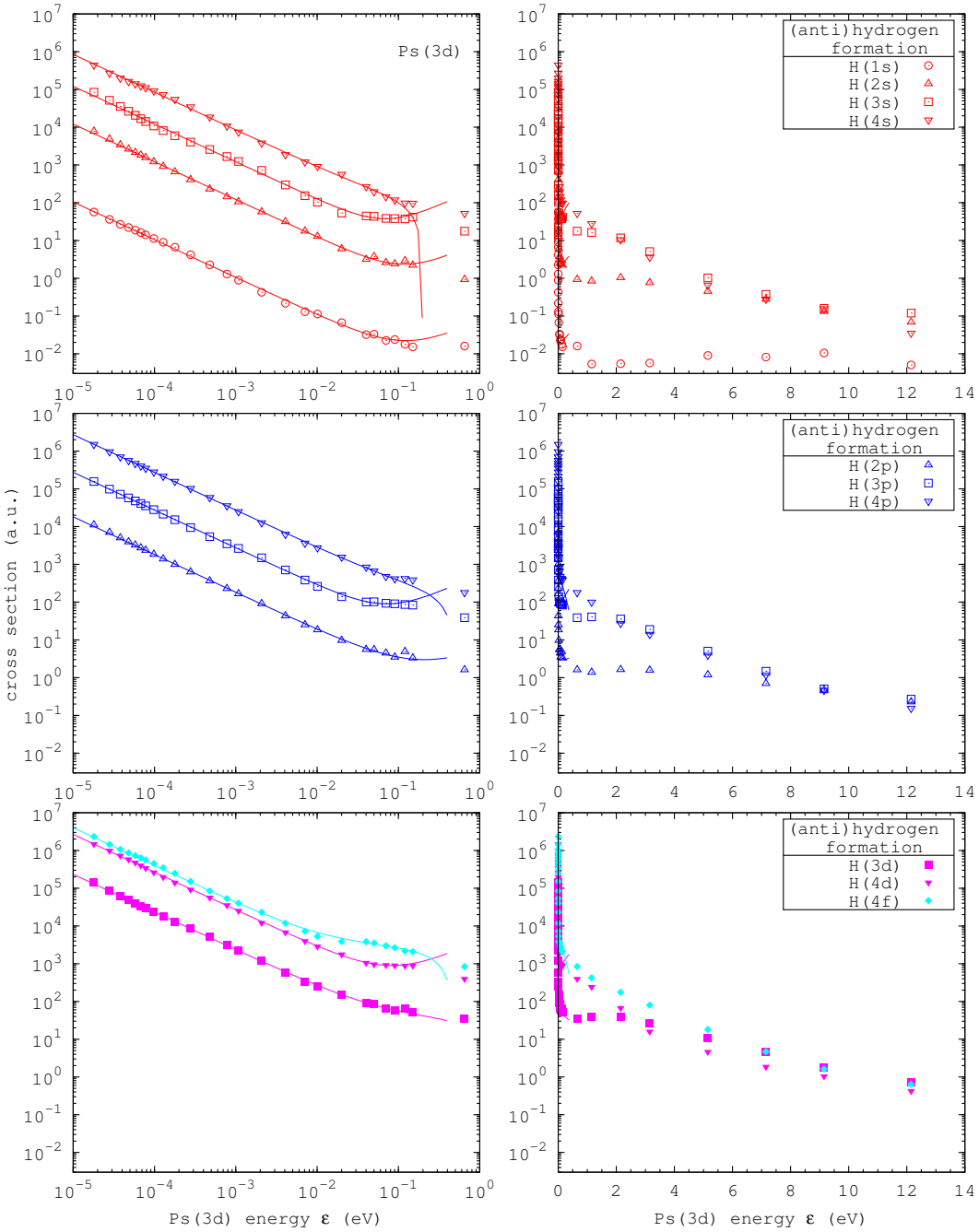

Figure 3.8: The cross sections for positronium in the $3d$ state scattering on (anti)protons to form (anti)hydrogen. The left-side data are for scattering at near-zero energies for formation of hydrogen in s (top), p (middle) d or f states (bottom). The right-side data are across a larger energy range. The solid lines for the near zero-energy results are the least-squares fits to the data up to 0.1 eV with the fitting parameters and their related errors given in table 3.6.

Table 3.6: Cross sections $\sigma_{\mathrm{H}(nl)} = \varepsilon^{-1}(a + b\varepsilon + c\varepsilon^2)$ (a.u.) for near-zero energy ε (eV) Ps($3d$) incident on (anti)protons, as shown by the solid lines in figure 3.8. These values were obtained by a least-squares fit of the data up to 0.1 eV. The numbers in the square brackets indicates the power of 10.

	a	b	c
$\sigma_{\mathrm{H}(1s)}$	(1.048±0.028)[−3]	(5.107±3.424)[−3]	(7.025±4.366)[−2]
$\sigma_{\mathrm{H}(2s)}$	(1.214±0.028)[−1]	(2.821±3.454)[−1]	(8.805±4.404)[+0]
$\sigma_{\mathrm{H}(2p)}$	(1.813±0.030)[−1]	(1.274±0.371)[+0]	(4.103±4.724)[+0]
$\sigma_{\mathrm{H}(3s)}$	(1.213±0.043)[+0]	(2.412±5.265)[+0]	(2.570±0.671)[+2]
$\sigma_{\mathrm{H}(3p)}$	(2.733±0.046)[+0]	(1.364±0.565)[+1]	(5.353±0.721)[+2]
$\sigma_{\mathrm{H}(3d)}$	(2.343±0.032)[+0]	(3.535±0.390)[+1]	(−2.597±4.971)[+1]
$\sigma_{\mathrm{H}(4s)}$	(8.463±0.199)[+0]	(7.395±2.456)[+1]	(−5.959±3.132)[+2]
$\sigma_{\mathrm{H}(4p)}$	(2.722±0.028)[+1]	(1.443±0.344)[+2]	(−4.255±4.381)[+2]
$\sigma_{\mathrm{H}(4d)}$	(2.662±0.028)[+1]	(2.549±0.343)[+2]	(3.892±0.438)[+3]
$\sigma_{\mathrm{H}(4f)}$	(3.996±0.163)[+1]	(2.852±0.201)[+3]	(−6.547±2.559)[+3]

3.2 Ps$(n = 4 - 5) - \bar{p}$ results

In order to extend the calculations to include Ps states with $n_{\mathrm{Ps}} \geq 3$ we have to consider the total number of channels required. Due to the degeneracy of the Ps energy levels we would have to set $l^{\mathrm{Ps}}_{\mathrm{max}} \leq n_{\mathrm{Ps}} - 1$. Also, due to the interplay between the initial Ps and final H states we would require $n_{\mathrm{H}} \geq n_{\mathrm{Ps}}$ and therefore $l^{\mathrm{H}}_{\mathrm{max}} \geq l^{\mathrm{Ps}}_{\mathrm{max}}$. The next desirable n_{Ps} value after 3 is $n_{\mathrm{Ps}} = 5$ since for this the channel for formation of H($n_{\mathrm{H}} \leq 7$) is open at zero Ps energy, with the energy difference between the initial and final states being very small (5.6 meV). Therefore, including all open channels at zero Ps energy would require $l^{\mathrm{Ps}}_{\mathrm{max}} = 4$ and $l^{\mathrm{H}}_{\mathrm{max}} = 6$. Using two complete expansions on both sides as for $n_{\mathrm{Ps}} \leq 3$ would be impractical for such large orbital angular momentum values. The number of channels generated in the close-coupling formalism would be too large to manage accurately for the energies of interest. When the amount of states open at zero energy is high, the numbers of singularities in Eq. 2.88 close to zero becomes high too. Numerically integrating over these singularities

was manageable for Ps($n_{\rm Ps} < 4$), but it would be too difficult to use the same method for higher $n_{\rm Ps}$. However, we can take advantage of the fact that the cross sections of interest are dominated by the interactions between the degenerate Ps states [136]. For our purposes we performed the calculations using only the $n_{\rm Ps} \leq 5$ and $n_{\rm H} \leq 7$ eigenstates of the respective Hamiltonians. The validity of this approach was tested by comparing the $n_{\rm Ps} = 2, 3$ results with those from the previous section and excellent agreement was found. This implies that the Ps static polarisability from its continuum has little impact on these results.

As before we have summed the results over the final H states formed for each initial Ps state. The results are presented in Fig. 3.9. The results from Fig. 3.2 are included for comparison. Due to the number of initial Ps states the data have been separated by $l_{\rm Ps}$ for $l_{\rm Ps} = 0, 1$ and 2 with 3 and 4 shown together. For ease of comparison a least-squares fit has been applied up to 0.1 eV for each Ps state. Accordingly, the solid lines in Fig. 3.9 are fits of the function $\sigma_{{\rm Ps}(nl)} = \varepsilon^{-1}(a + b\varepsilon + c\varepsilon^2)$, with the coefficients and their related errors given in Table 3.7. The a, b and c coefficients for Ps($n = 2$) are equal to the sum of the corresponding coefficients in Tables 3.2 to 3.3 within the given errors. For Ps($n = 3$) the same idea nearly applies but falls short. This is likely due to the nature of the least-squares fit for multiple functions rather than the change in approach. While the a parameters do not agree within the uncertainties, they typically agree within 5%, which is the level of convergence for the data these parameters are extracted from. For the b and c parameters very little agreement can be seen between the two methods, but for low energies these typically contribute very little. Like before, it can observed that the coefficients and their relative error increases from left to right, implying that this approximation is valid strictly at very low energies.

One can see that for each $l_{\rm Ps}$ value, as $n_{\rm Ps}$ increases the total H-formation

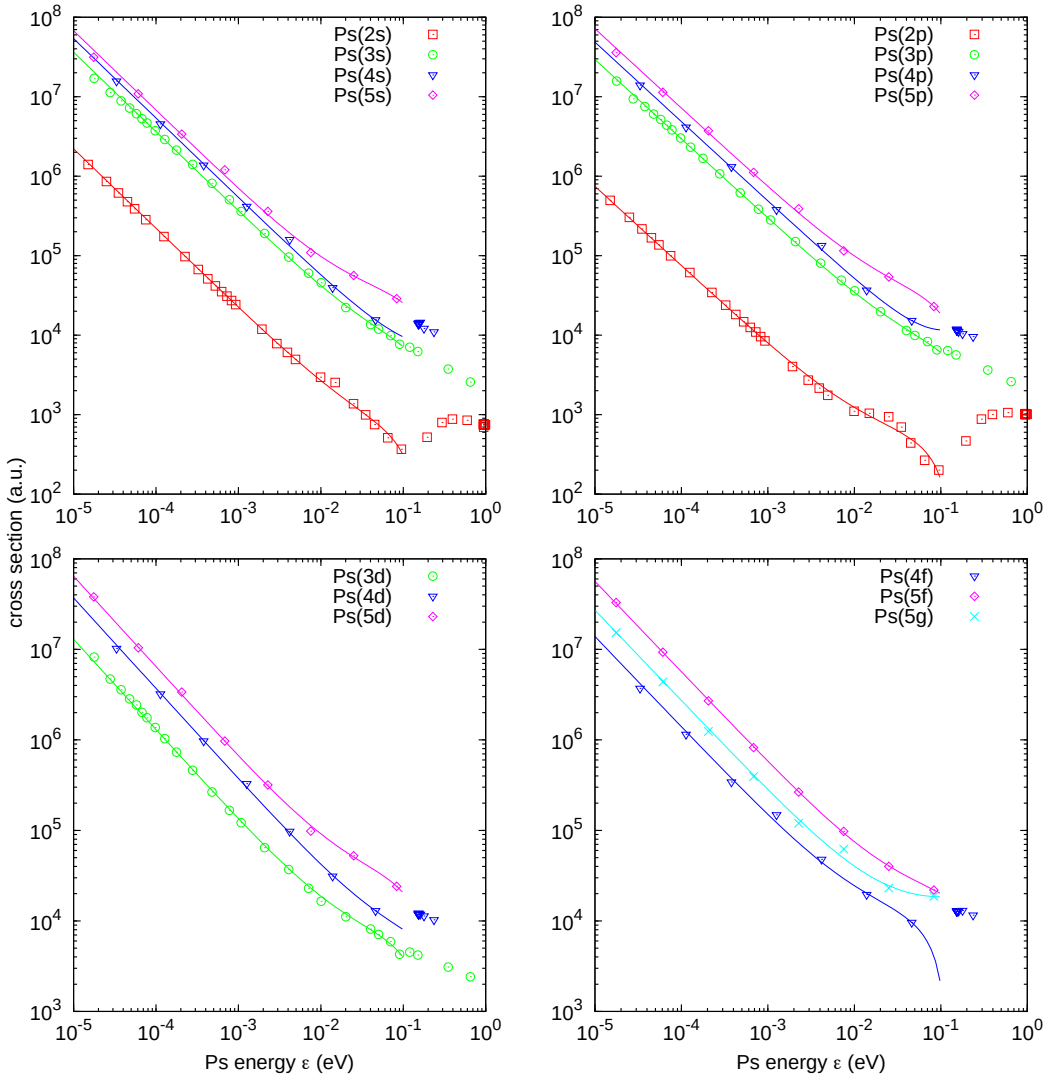

Figure 3.9: The cross sections for positronium scattering on (anti)protons to form (anti)hydrogen summed across all H final states. Results from Figure 3.2 are included for comparison. The solid lines for the near-zero energy results are the least-squares fits to the data up to 0.1 eV with the fitting parameters given in table 3.7.

cross section increases. However, the rate of increase drops for each n_{Ps}, in particular from $n_{\mathrm{Ps}} = 2$ to 3 there is over an order-of-magnitude increase, but after that the enhancement is less noticeable. Classically, these cross sections would be proportional to the square of the radius of the Ps atom, which is in

Table 3.7: Cross sections $\sigma_{\sum_{nl} \mathrm{H}(nl)} = \varepsilon^{-1}(a + b\varepsilon + c\varepsilon^2)$ (a.u.) for near-zero energy ε (eV) Ps incident on (anti)protons. These values were obtained by a least-squares fit of the data up to 0.1 eV. The numbers in the square brackets indicates the power of 10.

	a	b	c
Ps(2s)	(2.208±0.056)[+1]	(5.195±0.634)[+2]	(−4.323±0.772)[+3]
Ps(2p)	(7.453±0.477)[+0]	(5.358±0.541)[+2]	(−4.604±0.658)[+3]
Ps(3s)	(3.626±0.067)[+2]	(6.095±0.822)[+3]	(−2.577±1.048)[+4]
Ps(3p)	(2.940±0.031)[+2]	(5.510±0.382)[+3]	(−2.425±0.488)[+4]
Ps(3d)	(1.293±0.027)[+2]	(6.202±0.332)[+3]	(−3.531±0.424)[+4]
Ps(4s)	(5.382±0.317)[+2]	(3.567±7.301)[+3]	(5.607±155.700)[+3]
Ps(4p)	(4.859±0.186)[+2]	(2.927±4.282)[+3]	(3.838±9.131)[+4]
Ps(4d)	(3.702±0.130)[+2]	(5.442±2.982)[+3]	(−1.128±6.359)[+4]
Ps(4f)	(1.387±0.111)[+2]	(1.180±0.256)[+4]	(−1.130±0.545)[+5]
Ps(5s)	(6.758±0.420)[+2]	(3.196±0.581)[+4]	(−1.349±0.693)[+5]
Ps(5p)	(7.166±0.316)[+2]	(2.966±0.437)[+4]	(−1.847±0.521)[+5]
Ps(5d)	(6.429±0.261)[+2]	(2.892±0.360)[+4]	(−1.503±0.430)[+5]
Ps(5f)	(5.643±0.083)[+2]	(1.920±0.115)[+4]	(−4.844±1.367)[+4]
Ps(5g)	(2.712±0.225)[+2]	(1.295±0.311)[+4]	(2.859±3.706)[+4]

turn proportional to the square of the principle quantum number n. Therefore, these cross sections are expected to scale as n_{Ps}^4[15, 66, 139]. Instead they scale by n_{Ps}^2, as observed in Fig. 3.10 where the cross sections have been multiplied by n_{Ps}^{-2}. It is apparent that, excluding $n_{\mathrm{Ps}} = 2$, the results do scale according to n_{Ps}^2. This agrees with the quantum threshold theory prediction as determined in Kadyrov *et al.* [132].

For each n_{Ps} value it can be observed that for increasing l_{Ps} the cross sections decrease. This is easiest to notice by examining the a coefficients from Table 3.7. We can also observe that as n_{Ps} increases, the relative contributions to H formation across l_{Ps} starts to become more uniform. For Ps($n = 2$), nearly 75% of the contribution is from Ps($2s$). Ps($n = 3$) this drops to around 46% contribution from Ps($3s$), then 35% of Ps($n = 4$) from Ps($4s$) and finally 23% of Ps($n = 5$) from Ps($5s$). If the cross sections were independent of l_{Ps} then the

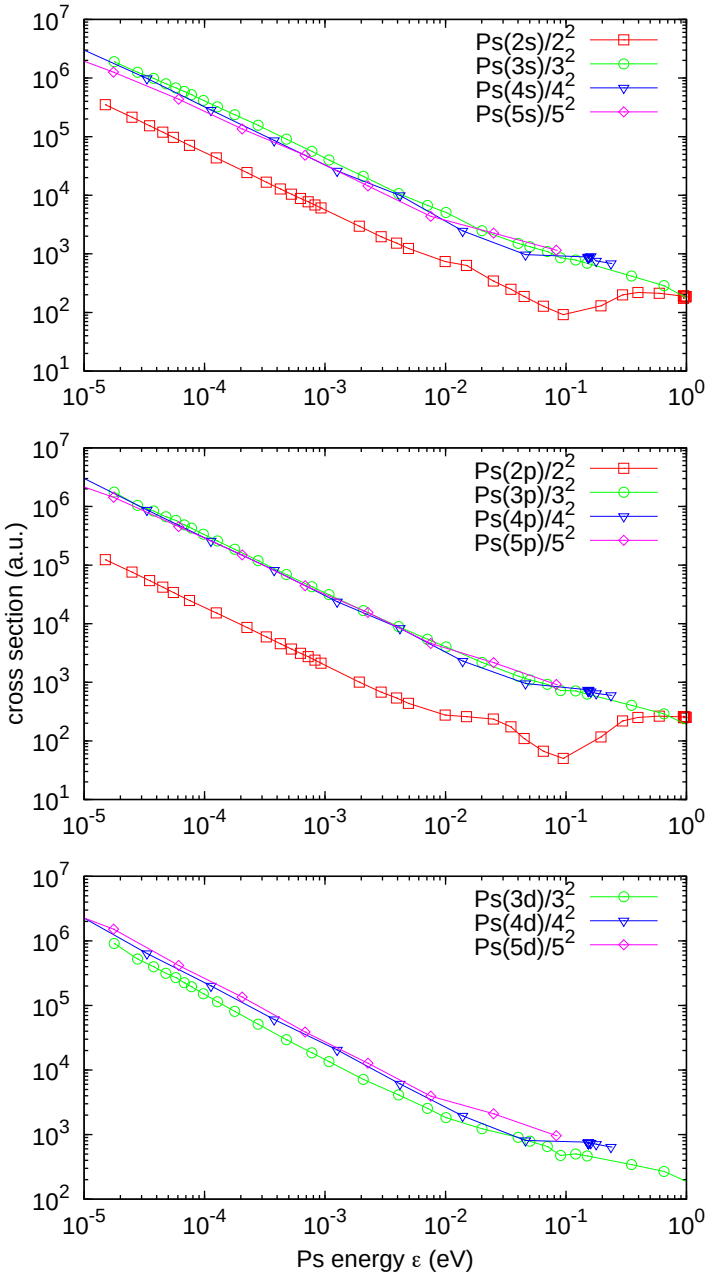

Figure 3.10: The cross sections for positronium scattering on (anti)protons to form (anti)hydrogen summed across all H final states scaled by $n_{\rm Ps}^{-2}$ for $l_{\rm Ps} = 0, 1$ and 2.

contributions would be expected to be 50% for $n_{\rm Ps} = 2$, 33.3% for $n_{\rm Ps} = 3$, 25% for $n_{\rm Ps} = 4$ and 20% for $n_{\rm Ps} = 5$. While this is only a rough approximation it indicates that as $n_{\rm Ps}$ increases, the contribution across $l_{\rm Ps}$ starts to become

equal. However, the highest $l_{\rm Ps}$ state for each $n_{\rm Ps}$ energy, i.e. Ps($2p$), Ps($3d$), Ps($4f$) and Ps($5g$), is always significantly lower than the other states. Whether this trend continues for higher $n_{\rm Ps}$ may be of interest.

An in-depth analysis for the production of specific H states has not been undertaken, mostly due to the large number of involved states. Qualitatively, similar trends observed for $n_{\rm Ps} = 2$ and 3 would be expected for higher $n_{\rm Ps}$. For instance, the formation of excited states of H is likely to be dominant. The distribution of these states may be of interest in future but currently we are concerned with total H formation aggregated over all final states. For $\bar{\rm H}$ experiments the goal is to make as many atoms as possible. By the time they are used in subsequent experiments it is expected that they will be in the ground state, or possibly the $2s$ state, irrespective of the state they were initially created.

3.3 Chapter summary

The results for Ps scattering on protons to form H have been presented for very low Ps energies across multiple initial states of Ps. This is equivalent to Ps scattering on antiprotons to form $\bar{\rm H}$. For ground-state Ps scattering we found excellent agreement with available theories [38, 86, 87, 134] and experiment [135]. For excited-state Ps scattering we found good qualitative agreement with the UBA results. The cross sections for near-zero energy Ps behave as predicted by threshold theories. This allows for the cross sections to be expressed in simple algebraic form. The use of excited states of Ps instead of ground state Ps resulted in a notable increase in total H-formation cross sections. However, the large increase in cross sections is not maintained with increasing $n_{\rm Ps}$. From $n_{\rm Ps} = 3$ the cross sections rise as $n_{\rm Ps}^2$, which is suppressed when compared to the classical expectation of $n_{\rm Ps}^4$.

These findings are of relevance for $\bar{\mathrm{H}}$ experiments planning to use reaction (3.1) [24, 25, 28, 29]. Some of these initiatives plan to use Rydberg Ps ($n_{\mathrm{Ps}} > 10$), intending to make use of the classical n_{Ps}^4 scaling prediction. However, the presented work casts doubts on the current estimates when Ps energy is low (< 0.1 eV)[69]. The current work predicts that the scaling in this low-energy region is in fact better described as n_{Ps}^2, at least up to $n_{\mathrm{Ps}} \leq 5$. Extending the CCC calculations to states Ps($n > 5$) is under consideration.

Chapter 4

Positron scattering on He^+

The singly-charged helium ion (He^+) is the simplest ionic target. This makes it an ideal target atom for testing the recent developments for positron scattering on an ionic target. However, due to difficulties associated with He^+ production there are currently no experimental results available for the e^+-He^+ collision system. The absence of experimental measurements means that little attention has been paid to this problem on the theoretical side too.

In this chapter we present the theoretical results for e^+-He^+ scattering as calculated using the CCC method. A convergence study will be presented to show the stability of our results. Internal-consistency checks will be used to validate the Ps-formation matrix elements as derived in section 2.3.3. And finally, the results will be compared with those from other methods.

4.1 Convergence studies

Systematically increasing the size of the basis N should produce results which converge to the solution of the underlying Lippmann-Schwinger equations. However, for two-centre problems it is not as straightforward due to potential double counting of the continuum. Therefore, more care has to be taken when increasing

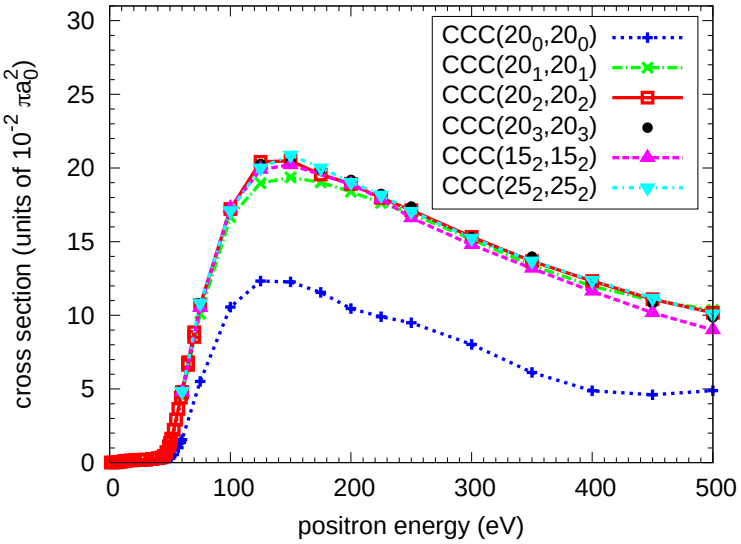

Figure 4.1: Total cross section, without the Rutherford term, for e^+-He^+ scattering. Different basis sizes are represented with the label CCC($N_{0l_{\max}}^{\mathrm{T}}, N_{0l_{\max}}^{\mathrm{Ps}}$), see text.

the basis size on both centres.

For convergence studies, calculations are performed with basis sizes $N = \sum_{l=0}^{l_{\max}} N_l$, where N_l is the size of the basis for each angular momentum l on both centres. Typically, we set $N_l = N_0 - l$ so that only N_0 and $l_{\max}$ need to be varied to test for convergence. The corresponding calculations for these tests are denoted as CCC($N_{0l_{\max}}^{\mathrm{T}}, N_{0l_{\max}}^{\mathrm{Ps}}$). For all states, the fall-off parameter λ_l is set to 2.0 for He^+ and 0.5 for Ps independent of l. With $N_0 = 1$ these choices lead to exact $He^+(1s)$ and $Ps(1s)$ states, respectively.

In what follows we do not incorporate the second term in Eq. (2.37), otherwise known as the Rutherford term. This ensures that the elastic, and hence total, cross section remain finite allowing for convergence checking for each partial wave of the total orbital angular momentum.

The convergence study for the total cross section is shown in Fig. 4.1. To test convergence in the orbital angular momentum (l) of the included states,

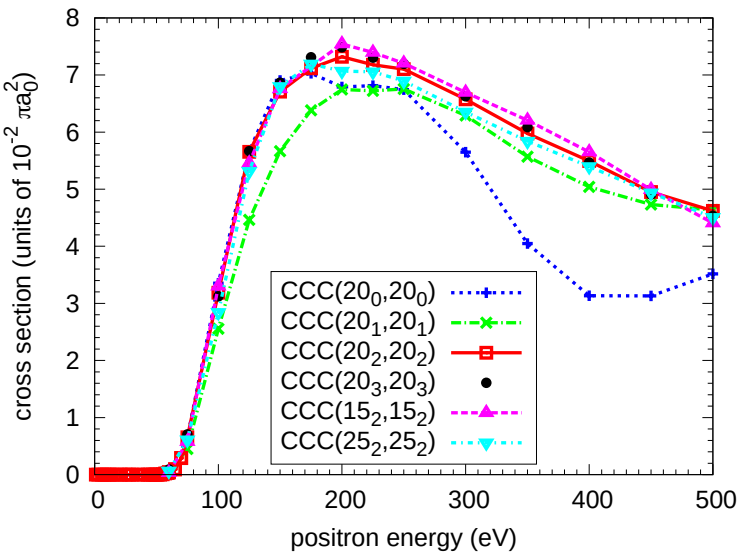

Figure 4.2: Total breakup cross section for e^+-He^+ scattering. Theory is the same as for Fig. 4.1.

there are sets of calculations with $N_0 = 20$ with $l_{\max} = 0, 1, 2, 3$. For the total cross section the inclusion of p in addition to the s states has made a significant change to the results, nearly doubling it at higher energies. Inclusion of d states was less substantial but contributed an additional 5-10% to the maximum cross section. The inclusion of f states had practically no effect, less than 1% increase across the energy range This is very similar to calculations for e^+ scattering on H [109] and He [113]. Additional tests were performed for $l_{\max} = 2$ and $N_0 = 15$ and 25 to check convergence with N_l. For the total cross section the $N_l = 25$ data was nearly indistinguishable from the $N_l = 20$ data, within 1% across all energies. The same could be said for the $N_l = 15$ results except for energies greater than 400 eV. Here the smaller basis size appears to underestimate the results of the larger basis which is to be expected. It is possible that the number of positive-energy pseudostates is insufficient for these energies.

The convergence study for the total breakup cross sections is presented in Fig. 4.2 using the same procedure as for the total cross sections. For the total

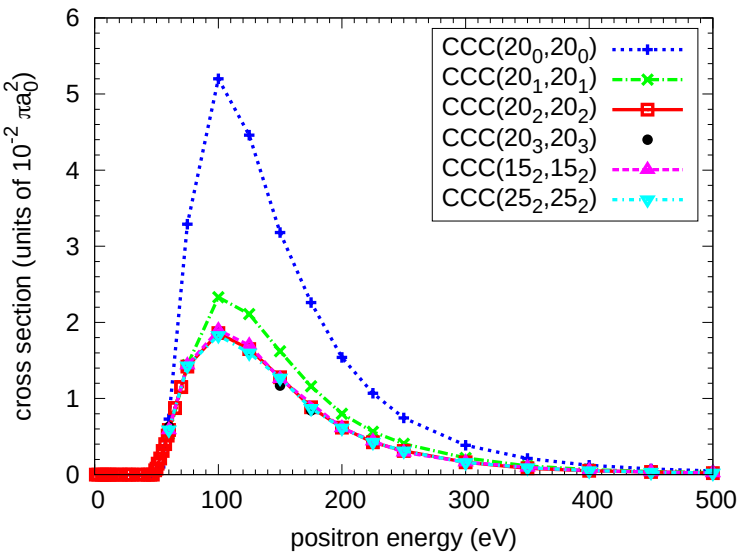

Figure 4.3: Total Ps-formation cross section for e^+-He^+ scattering.

breakup cross section the inclusion of p states has given the results a smoother appearance when compared to just s states. Addition of the d states was more significant for breakup than it was for the total cross sections, contributing an additional 20% at the maximum. The inclusion of f states had little affect on the cross sections ($< 2\%$). When changing from $N_0 = 15$ to $N_0 = 20$ the cross sections decrease by around 5% up to 250 eV. For energies higher than this there is a larger difference, most likely due to a lack of states in the energy region. When changing from $N_0 = 20$ to $N_0 = 25$ the results have very little change.

The convergence study for the total positronium formation cross sections is presented in Fig. 4.3 using the same procedure as for the total cross sections. For the total Ps-formation cross section we instead see a significant drop in the cross section when p states are included and a further drop when d states are included. When f states are included the change is very small, around 5% across all energies. When changing from $N_0 = 15$ to $N_0 = 20$ the cross sections decrease by around 1% up to 200 eV. For energies higher than this there is a larger difference, most likely due to a lack of states in the energy region. When

changing from $N_0 = 20$ to $N_0 = 25$ the results have very little change.

It can be observed that the basis CCC$(20_2, 20_2)$ is large enough to generate accurate e^+-He^+ scattering cross sections at all energies considered.

4.2 Internal-consistency checks

Internal consistency makes use of the completeness of the Laguerre basis to compare single-centre CCC calculations with two-centre CCC calculations [140]. A large enough single-centre expansion can be used to account for Ps formation indirectly using positive energy states. Below the Ps-formation and above the ionisation thresholds of the target, both a single- and two-centre expansion should yield the same results for the grand total and electron-loss cross sections. This is an ideal test for the two-centre CCC method as the newly developed Ps-formation matrix elements could be validated against the direct scattering matrix elements which have been used in the CCC method since its inception [108, 121, 122, 141]. Between the Ps$(1s)$ formation and the ionisation thresholds (the extended Ore gap) this idea breaks down due to electron-loss not being possible for the single-centre approach since in the extended Ore gap Ps formation is explicitly required.

For the internal-consistency checks we compare a set of two-centre calculations CCC$(20_2, 20_2)$ with a set of single-centre calculations CCC$(30_9, 0)$. For both sets of calculations we compare the grand total and electron-loss cross sections in Figs. 4.4 and 4.5 respectively. The inserts for both figures highlight the region from 40 to 60 eV to further examine the extended Ore gap. For the total cross section very little difference can be observed between the two expansions. The same could be said of the electron-loss cross section until we examine the extended Ore gap more closely. Here we find that the threshold

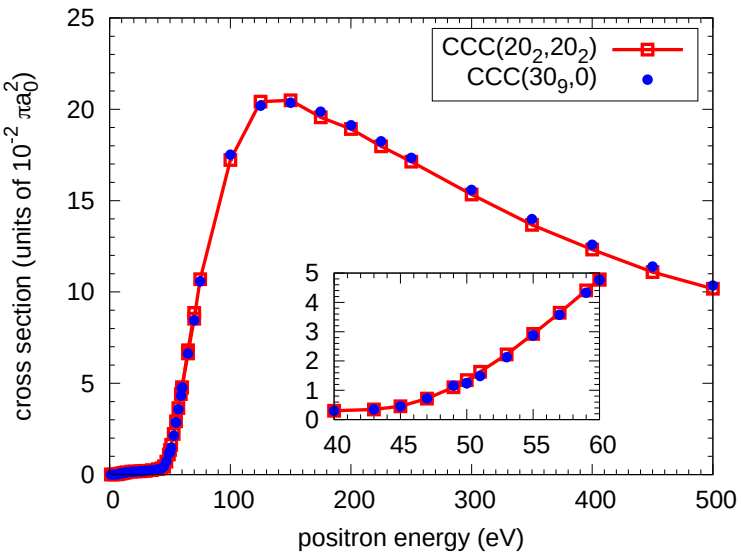

Figure 4.4: Total cross section without the Rutherford term for e^+-He^+ scattering. The insert highlights the region around the ionisation threshold.

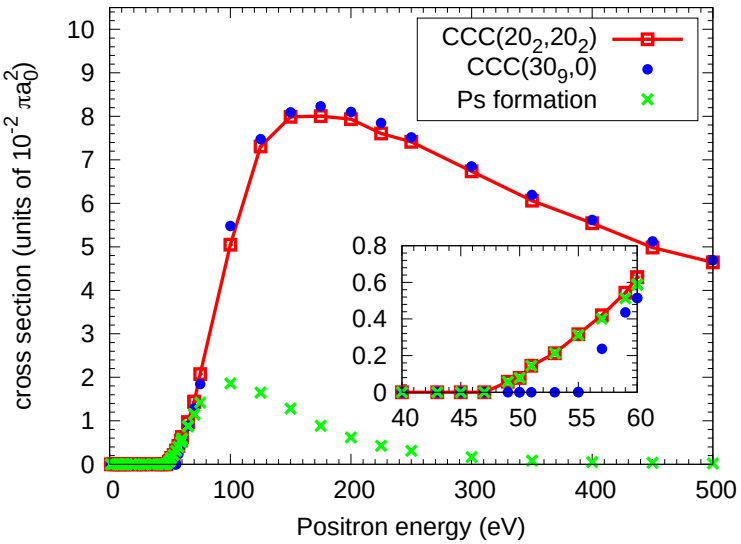

Figure 4.5: Electron-loss cross section for e^+-He^+ scattering. The insert highlights the region around the ionisation threshold.

for the electron-loss cross section are around 47 and 55 eV for the two- and single-centre calculations, respectively. This lines up with the Ps($1s$) formation and ionisation thresholds of 47.6 eV and 54.4 eV, respectively. This is to be expected since with a single-centre expansion there is no possibility for Ps for-

mation, meaning the only way for the target to lose its electron is via ionisation. This is further validated when we include the Ps-formation cross section and see that within this region electron-loss is entirely due to Ps formation.

These two checks show that the inclusion of the new Ps-formation matrix elements conserves the unitarity of the close-coupling formalism. This is clear for a single-centre calculation which utilizes a complete basis, but less clear when a two-centre expansion is utilised using two independently-complete bases. The agreement between the two calculations indicates no double counting problems.

4.3 Comparison with other theories

There are currently no experimental results available for this system, and due to the difficulties associated with rearrangement including a residual long-range Coulomb interaction, little theoretical work is available.

Much work has been done for the region where only elastic scattering is possible. Figure 4.6 compares the total cross section for $J = 0 - 2$ from the CCC$(20_2, 20_2)$ calculations with those generated from phase shifts of previous calculations [142]. In particular, the close-coupling (CC) calculations from Bransden *et al.* [89], enlarged six-pseudostate (E6PS) Harris-Nesbit variational method by Gien [49] and configuration-interaction Kohn (CI-KOHN) variational method by Novikov *et al.* [39]. The CI-KOHN results were only made available for $J = 0, 1$. For these partial waves they show very good agreement with the corresponding CCC results. The same can be said for the E6PS results but for all values of J. The CC results appear to deviate slightly from the other results as energy increases. A possible source of the deviation is the size of the basis used in the CC calculations being too small. The CC calculations used 26 He^+ states and 1 Ps state compared to the 57 He^+ states and the 57 Ps states used

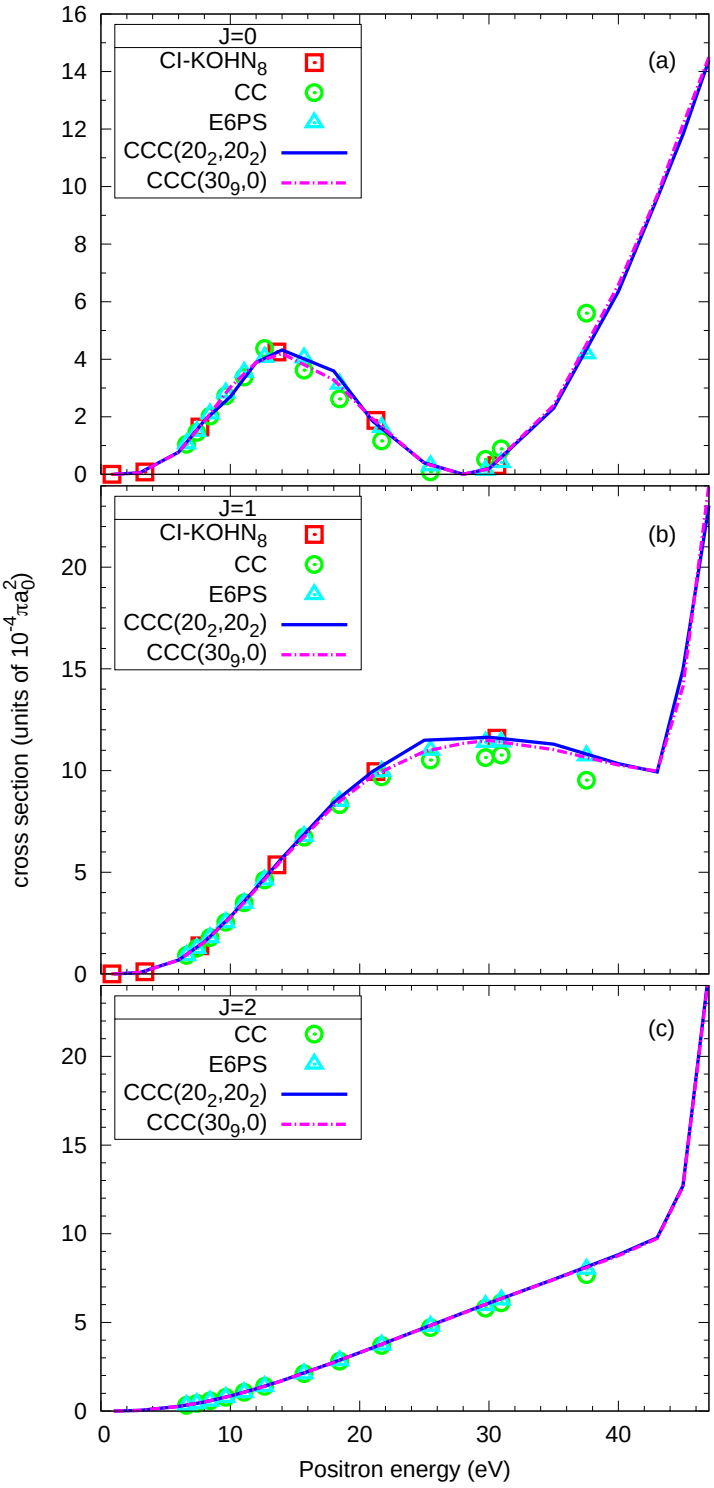

Figure 4.6: Total cross section in partial waves for (a) J=0, (b) J=1 and (c) J=2. Solid line represents the two-centre CCC results, the dotted line represents the single-centre CCC results, square, circle and triangular points are generated using the phase shifts from the CI-KOHN calculations of Novikov *et al.* [39], CC calculations of Bransden *et al.* [89] and E6PS calculations of Gien [49], respectively.

in the CCC($20_2, 20_2$) calculations.

The CC calculations from Bransden *et al.* [89] also include results above the ionisation threshold for various processes. In this case two sets of bases were used to test for convergence, one with 19 He^+ and 1 Ps state (CC(19,1)) and the other with 26 He^+ states and 3 Ps states (CC(26,3)). Additionally, Ps formation for e^+-He^+ was investigated using a two-centre eikonal-final-state continuum-initial-distorted-wave (EFS-CDW) method [61, 62].

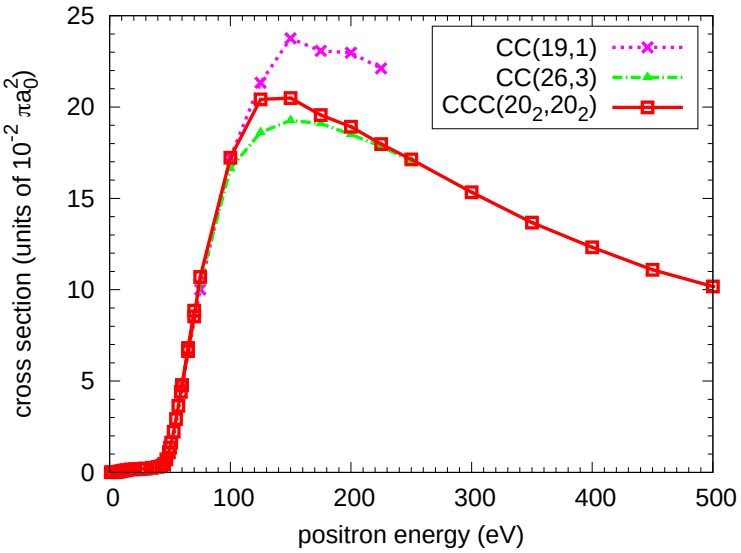

Figure 4.7: Total cross section without Rutherford term for e^+-He^+ scattering. Close-coupling results are from Bransden *et al.* [89].

Figure 4.7 shows the total cross section from CCC calculations compared to the CC calculations from Bransden *et al.* [89]. Excellent agreement between the three sets of data can be observed up until around 100 eV where the results of the smaller CC(19,1) calculations begin to overestimate the CCC results and the CC(26,3) results begin to underestimate. The larger of the CC calculationss appears the most stable out of the CC data and starts to agree with the CCC results starting from 200 eV. If the CC calculations were performed for higher energies then the agreement between CC(26,3) and CCC could be tested.

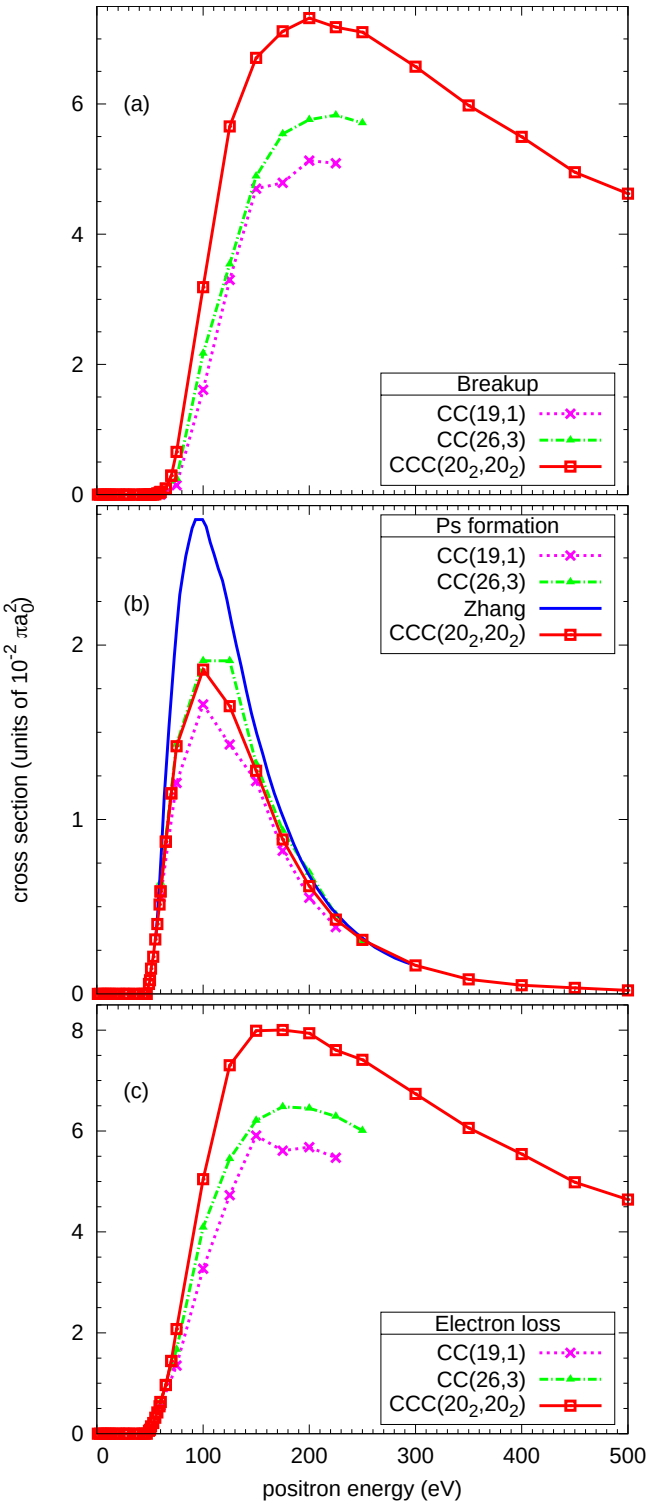

Figure 4.8: Breakup (a), Ps-formation (b) and electron-loss (c) cross sections for e^+-He^+ scattering. Close-coupling results are from Bransden *et al.* [89] and Ps-formation results are from Zhang *et al.* [62].

Figures 4.8(a)-(c) show the total breakup, Ps-formation and electron-loss cross sections (the sum of the first two), respectively. There is some discrepancy between the CC and CCC results with both sets of CC results being visibly smaller than the CCC results for the breakup cross section. This is likely due to the insufficient number of the positive-energy states in the CC calculations. Good agreement for Ps formation implies that this component is largely dominated by Ps in the ground state since that is the only state available for CC(19,1). The EFS-CDW results of Zhang *et al.* [62] are considerably larger than the CC and CCC results. In these calculations Ps($n = 1 - 4$) were used to approximate the total Ps-formation cross section so it is possible that the cross section for Ps($n > 2$) are higher than expected; however, these were not presented by Zhang *et al.* [62].

Figure 4.9 shows the elastic-scattering, 2s and 2p excitation cross sections. For each process the single-centre CCC($30_9, 0$) results are presented with the two-centre CCC($20_2, 20_2$) results. Excellent agreement for each case acts as further validation via internal-consistency checks. For elastic scattering, as the CC basis gets larger the results appear to be approaching the CCC results. Whether this continues for larger CC bases is yet to be seen, but the CC and CCC results have very good agreement up until around 100 eV. For the smallest cross section, which is for $2s$ excitation, the CC(26,3) results overlap with the CCC results. For the largest cross section, which is for $2p$ excitation, the CC results are marginally larger than the CCC results for increasing energy.

Figure 4.10 shows the cross sections for Ps formation in the $1s, 2s$ and $2p$ states. For the formation of Ps($1s$) the CCC results show good agreement with the two sets of CC results, with the larger basis having better agreement as expected. The EPS-CDW results, however, are nearly 50% higher at the maximum. For Ps($2s$) formation the CC results fluctuates between the EPS-CDW

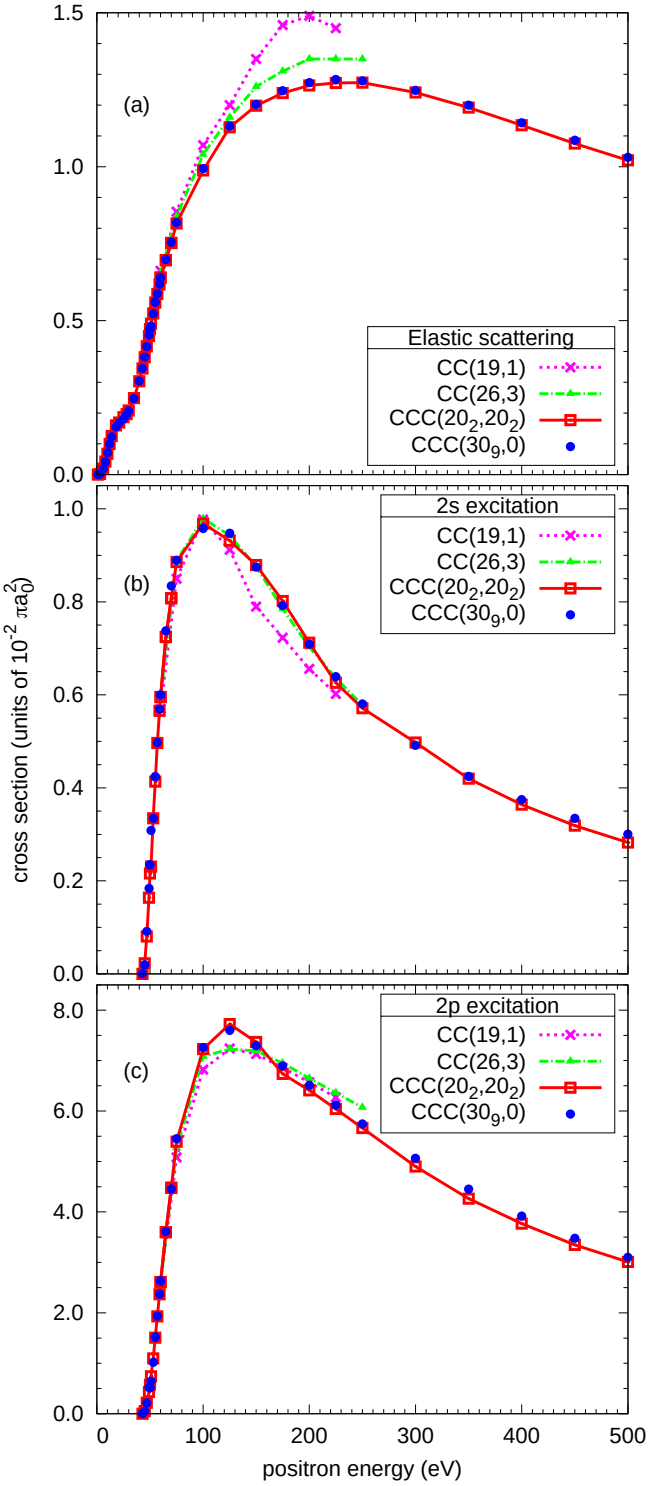

Figure 4.9: Cross sections for elastic-scattering without Rutherford term (a), 2s (b) and 2p (c) excitation in e^+-He^+ scattering. Close-coupling results are from Bransden *et al.* [89].

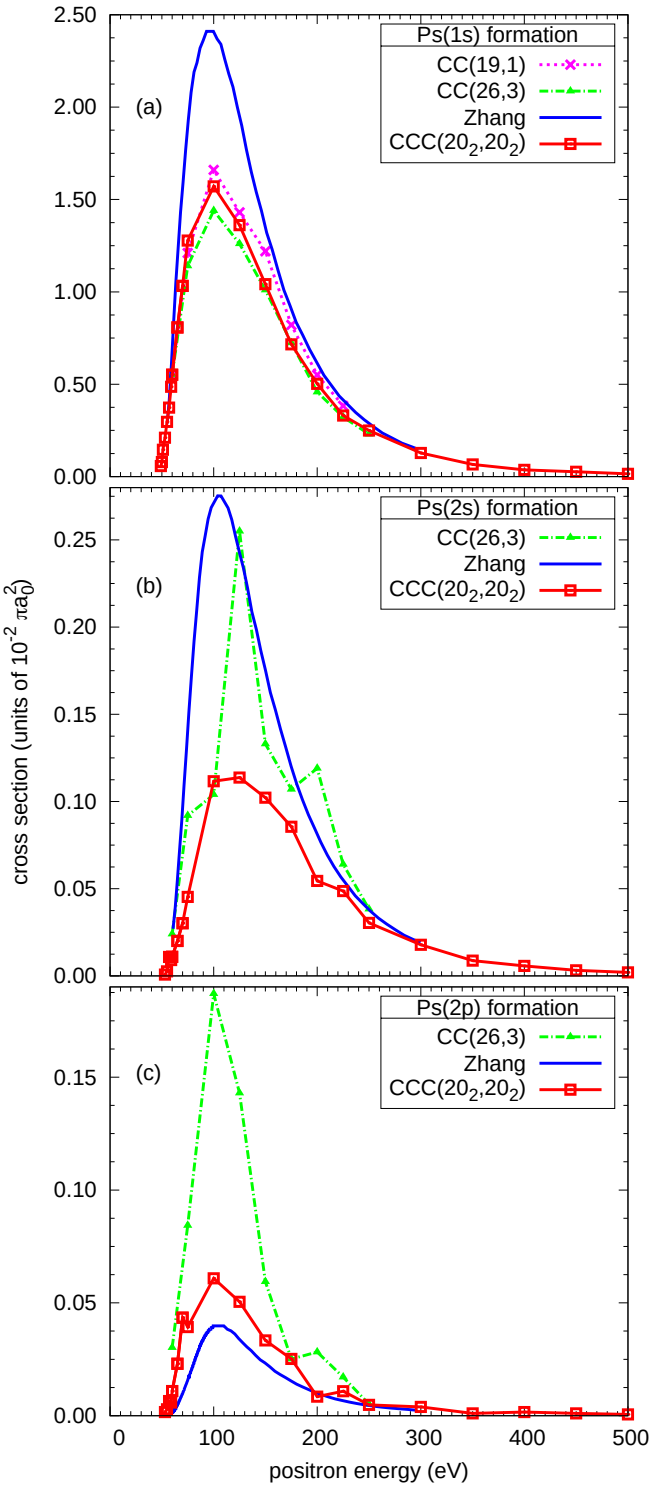

Figure 4.10: Cross sections for positronium formation in the 1s (a), 2s (b) and 2p (c) states in e^+-He^+ scattering. Close-coupling results are from Bransden *et al.* [89] and Ps-formation results are from Zhang *et al.* [62].

and the CCC results, which differ by more than a factor of 2 at the maximum. For Ps($2p$) formation the CC results are much larger than the CCC results for most energies and the EPS-CDW results are smaller. In all cases there is typically good agreement near the threshold and above 200 eV. Whether this continues for higher energies is yet to be seen. Some non-physical deviations can be observed for the CCC-calculated Ps($2s$) and Ps($2p$) cross sections. Though not as significant as the deviations observed in the CC-calculated results, it is evidence of numerical instabilities. These arise due to the system being highly ill-conditioned, and are difficult to remove for small cross sections. While Ps($1s$) formation cross sections are converged to $\pm 3\%$, Ps($2s$) is more around 10% converged, and Ps($2p$) has points which are nearly 50% away from the observed trend line.

The analytic treatment of the Green's function in the CCC method [126, 127] has proven to be very successful in smoothing these points for e^+-H and $e^--\mathrm{He}^+$ scattering. Similar improvements would be expected for $e^+-\mathrm{He}^+$ scattering but this is for further investigation. For now, however, due to the overall small size of the Ps($2s$) and Ps($2p$) cross sections when compared to the grand total and electron-loss cross sections, these deviations do not affect the internal-consistency checks presented in section 4.2.

4.4 Chapter summary

The cross sections for positron scattering on He^+ have been presented in this chapter for various processes across a wide range of energies. Convergence has been achieved by carefully increasing N_0 and $l_{\max}$ on both centres. Internal-consistency checks have been used to validate the newly developed Ps-formation matrix elements for the CCC method. The results are consistent with other the-

oretical methods, with the notable exceptions of total breakup and Ps formation in excited states. Without experimental validation it is difficult to confirm the accuracy of the calculations, but the internal consistency gives us confidence in the CCC results.

Chapter 5

Conclusion

Investigations into the properties of antihydrogen ($\bar{\mathrm{H}}$) have been an area of great interest for decades. A promising mechanism for $\bar{\mathrm{H}}$ production involves the scattering of positronium (Ps) on antiprotons ($\bar{p}$). In order to aid with experiments, the calculation of the cross sections for this process is required, in particular for the formation of low energy $\bar{\mathrm{H}}$. Several methods use the charge-conjugate, time-reversed process of positron scattering on H as a starting point. However, these methods are typically only reliable for intermediate or high energies (CDW-FS[54],EFS-CDW[60], UBA[81, 86, 87], TDCC[104, 107]), for Rydberg level Ps (Monte Carlo[70, 71]) or Ps($n = 1, 2$) (Variational [36, 48], HSCC[95],CC[85]). These methods have also been applied to the problem of positron scattering on the singly charged helium ion (He^+).

This thesis presented the application of the two-centre convergent close-coupling method to $\bar{\mathrm{H}}$ formation for Ps($n = 1 - 5$). Cross sections for this process were calculated for Ps energies low enough to observe predicted threshold behaviour. This allowed for the cross sections to be expressed in terms of simple algebraic formulas. In general it was observed that the use of excited states of Ps produced larger cross sections. The hydrogen produced using these excited states were more likely to also be in excited states, typically in states which had

energy levels close to those of the initial Ps state. It was also observed that for increasing n_{Ps} the total hydrogen formed rise as n_{Ps}^2 for $n_{\mathrm{Ps}} \geq 3$, contrary to the classical scaling law of n_{Ps}^4. It would be of interest to perform the same calculations for $n_{\mathrm{Ps}} > 5$ to observe the range of validity of this scaling law and for what n_{Ps} value the classical scaling law comes into play.

In order to apply a similar analysis to the formation of the antihydrogen ion, changes had to be applied to the CCC method. Therefore, the two-centre convergent close-coupling method was developed for positron scattering on charged targets and applied to a singly-charged helium ion. Cross sections for several processes including elastic scattering, excitation, grand total and total Ps formation cross sections are found to be in good agreement with other calculations[89]. The cross sections for breakup and formation of excited Ps states however are not in good agreement with previous calculations. Convergence testing, internal-consistency checks and the smooth appearance of the cross sections gives us confidence in our results. Experimental validation would assist in confirming the accuracy of the calculations, however due to lack of interest and difficulties associated with e^++He^+ scattering experiments, this is unlikely to occur. The method can also be applied to Ps-He^{+2} collisions.

The computer code developed in this project was constructed on top of the existing CCC code used for electron scattering on atoms and ions and for positron scattering on neutral targets. It would be of interest to apply this approach to position scattering on ions like Li^{2+}, Be^{3+} and B^{4+}. Results for elastic scattering phase shifts of these systems are available in [39, 50]. Ground state for Ps($1s$) formation for H-like ions ($Z = 1 - 9$) are also available [61] for comparison. This would require incorporating short-ranged Coulomb interactions for the positronium formation matrix elements, similar to the work for positron scattering on alkalis [116–118].

Another important development is to incorporate a similar approach to He-like targets, in particular the negative hydrogen ion. This would allow us to perform calculations relating to $\bar{H}^+$ formation via reaction 1.3. While a lot of the required alterations to the He-like matrix elements are very similar to the alterations made to the H-like matrix elements, there are some additional numerical challenges which require investigation, such as the treatment of the complex singularity when $n < 0$.

Appendix A

Signed Statements of Others

To Whom It May Concern I, Charlie Michael Rawlins, contributed the development of research ideas and methodology to the paper/publication entitled **Antihydrogen formation via antiproton scattering with excited positronium**. Phys. Rev. Lett., **114**, 183201 (2015).

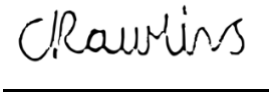

I, as a Co-Author, endorse that this level of contribution by the candidate indicated above is appropriate.

Alisher Kadyrov 

Igor Bray 

Andris Stelbovics 

Michael Charlton 

To Whom It May Concern I, Charlie Michael Rawlins, contributed the data analysis and preparation of the manuscript to the paper/publication entitled **Calculation of antihydrogen formation via antiproton scattering with excited positronium**. Phys. Rev. A, **93**, 012709 (2016).

C.Rawlins

I, as a Co-Author, endorse that this level of contribution by the candidate indicated above is appropriate.

Alisher Kadyrov

Igor Bray

Andris Stelbovics

Michael Charlton

To Whom It May Concern I, Charlie Michael Rawlins, contributed to the development of research ideas, methodology, data analysis and the preparation of the manuscript to the paper/publication entitled **Two-center convergent close-coupling approach to positron–helium-ion collisions**. Phys. Rev. A, **97**, 012707 (2018).

C.Rawlins

I, as a Co-Author, endorse that this level of contribution by the candidate indicated above is appropriate.

Alisher Kadyrov

Igor Bray

To Whom It May Concern I, Charlie Michael Rawlins, contributed to the development of research ideas, methodology, data analysis and the preparation of the manuscript to the paper/publication entitled **Convergent close-coupling approach to positron scattering on He^+.** Eur. Phys. J. D, **72**, 77 (2018).

C.Rawlins

I, as a Co-Author, endorse that this level of contribution by the candidate indicated above is appropriate.

Alisher Kadyrov

Igor Bray

To Whom It May Concern I, Charlie Michael Rawlins, contributed to the review of the final manuscript for the paper/publication entitled **Antihydrogen formation in low-energy antiproton collisions with excited-state positronium atoms**. Hyperfine Interact., **239**, 42 (2018).

C.Rawlins

I, as a Co-Author, endorse that this level of contribution by the candidate indicated above is appropriate.

Alisher Kadyrov

Igor Bray

Ilya Fabrikant

Michael Charlton

List of Figures

List of Tables

Bibliography

[1] P. Dirac, Proc. Roy. Soc. (London) **A117**, 610 (1928).

[2] M. Charlton, J. Eades, D. Horváth, R. Hughes, and C. Zimmermann, Phys. Rep. **241**, 65 (1994).

[3] M. H. Holzscheiter, M. Charlton, and M. M. Nieto, Physics Reports **402**, 1 (2004).

[4] M. Hori and J. Walz, Prog. Part. Nucl. Phys. **72**, 206 (2013).

[5] W. A. Bertsche, E. Butler, M. Charlton, and N. Madsen, J. Phys. B: At. Mol. Opt. Phys. **48**, 232001 (2015).

[6] G. Chardin *et al.* (GBAR Collaboration), *Proposal to measure the Gravitational Behaviour of Antihydrogen at Rest*, Tech. Rep. CERN-SPSC-2011-029. SPSC-P-342 (CERN, Geneva, 2011).

[7] M. Amoretti *et al.* (ATHENA Collaboration), Nature **419**, 456 (2002).

[8] G. B. Andresen *et al.* (ALPHA Collaboration), Nature **468**, 673 (2010).

[9] G. B. Andresen *et al.*, Nature Phys. **7**, 558 (2011).

[10] M. Ahmadi *et al.* (ALPHA Collaboration), Nature **541**, 506 (2017).

[11] Y. Enomoto *et al.*, Phys. Rev. Lett. **105**, 243401 (2010).

[12] N. Kuroda *et al.*, Nature Commun. **5**, 3089 (2014).

[13] B. I. Deutch, A. S. Jensen, A. Miranda, and G. C. Oades, *1st Workshop on Antimatter Physics at Low-energy Batavia, Illinois*, eConf **C860410**, 371 (1986).

[14] B. I. Deutch, F. M. Jacobsen, L. H. Andersen, P. Hvelplund, H. Knudsen, M. H. Holzscheiter, M. Charlton, and G. Laricchia, Phys. Scr. **T22**, 248 (1988).

[15] M. Charlton, Phys. Lett. A **143**, 143 (1990).

[16] B. I. Deutch, M. Charlton, M. H. Holzscheiter, P. Hvelplund, L. V. Jørgensen, H. Knudsen, G. Laricchia, J. P. Merrison, and M. R. Poulsen, Hyperfine Interactions **76**, 151 (1993).

[17] C. H. Storry *et al.* (ATRAP Collaboration), Phys. Rev. Lett. **93**, 263401 (2004).

[18] S. Cialdi, I. Boscolo, F. Castelli, F. Villa, G. Ferrari, and M. G. Giammarchi, Nuc. Instrum. Meth. B **269**, 1527 (2011).

[19] D. B. Cassidy, T. H. Hisakado, H. W. K. Tom, and A. P. Mills Jr, Phys. Rev. Lett. **108**, 043401 (2012).

[20] A. Deller, D. Edwards, T. Mortensen, C. A. Isaac, D. P. van der Werf, H. H. Telle, and M. Charlton, J. Phys. B: At. Mol. Opt. Phys. **48**, 175001 (2015).

[21] T. E. Wall, A. M. Alonso, B. S. Cooper, A. Deller, S. D. Hogan, and D. B. Cassidy, Phys. Rev. Lett. **114**, 173001 (2015).

[22] C. J. Baker *et al.*, J. Phys. B: At. Mol. Opt. Phys. **51**, 035006 (2018).

[23] S. Aghion *et al.* (AEgIS Collaboration), Phys. Rev. A **94**, 012507 (2016).

[24] M. Doser *et al.* (AEgIS Collaboration), Class. Quant. Grav. **29**, 184009 (2012).

[25] D. Krasnický *et al.* (AEgIS Collaboration), Int. J. Mod. Phys. Conf. Ser. **30**, 1460262 (2014).

[26] P. Debu for the GBAR Collaboration, Hyperfine Interactions **212**, 51 (2012).

[27] P. Pérez and Y. Sacquin, Class. Quant. Grav. **29**, 184008 (2012).

[28] D. P. van der Werf, Int. J. Mod. Phys. Conf. Ser. **30**, 1460263 (2014).

[29] P. Pérez *et al.* (GBAR Collaboration), Hyperfine Interact. **233**, 21 (2015).

[30] J. Walz and T. W. Hänsch, Gen. Relat. Gravit. **36**, 561 (2004).

[31] Charlton, Michael, Eur. Phys. J. D **71**, 307 (2017).

[32] W. Kohn, Phys. Rev. **74**, 1763 (1948).

[33] J. W. Humberston, J. Phys. B: At. Mol. Phys. **17**, 2353 (1984).

[34] C. J. Brown and J. W. Humberston, J. Phys. B: At. Mol. Phys. **17**, L423 (1984).

[35] C. J. Brown and J. W. Humberston, J. Phys. B: At. Mol. Phys. **18**, L401 (1985).

[36] J. W. Humberston, M. Charlton, F. M. Jacobson, and B. I. Deutch, J. Phys. B: At. Mol. Phys. **20**, L25 (1987).

[37] J. W. Humberston, P. V. Reeth, M. S. T. Watts, and W. E. Meyerhof, J. Phys. B: At. Mol. Opt. Phys. **30**, 2477 (1997).

[38] J. W. Humberston and P. Van Reeth, (2015), private communication.

[39] S. A. Novikov, M. W. J. Bromley, and J. Mitroy, Phys. Rev. A **69**, 052702 (2004).

[40] F. E. Harris, Phys. Rev. Lett. **19**, 173 (1967).

[41] R. K. Nesbet, Phys. Rev. **175**, 134 (1968).

[42] R. K. Nesbet, Phys. Rev. **179**, 60 (1969).

[43] R. K. Nesbet, *Variational Method in Electron-Atom Scattering Theory*, Physics of Atoms and Molecules (Springer US, 1980).

[44] G. Liu and T. T. Gien, Phys. Rev. A **46**, 3918 (1992).

[45] T. T. Gien and G. G. Liu, Phys. Rev. A **48**, 3386 (1993).

[46] T. T. Gien, J. Phys. B: At. Mol. Opt. Phys. **30**, L23 (1997).

[47] Y. R. Kuang and T. T. Gien, Phys. Rev. A **55**, 256 (1997).

[48] T. T. Gien, Phys. Rev. A **56**, 1332 (1997).

[49] T. T. Gien, J. Phys. B: At. Mol. Opt. Phys. **34**, L535 (2001).

[50] T. T. Gien, J. Phys. B: At. Mol. Opt. Phys. **34**, 5103 (2001).

[51] I. M. Cheshire, Proc. Phys. Soc. **84**, 89 (1964).

[52] O. A. Fojón, R. D. Rivarola, R. Gayet, J. Hanssen, and P. A. Hervieux, Phys. Rev. A **54**, 4923 (1996).

[53] J. Hanssen, P. A. Hervieux, O. A. Fojón, and R. D. Rivarola, Phys. Rev. A **63**, 012705 (2000).

[54] P. Comini and P.-A. Hervieux, New J. Phys. **15**, 095022 (2013).

[55] P. Comini, P.-A. Hervieux, and F. Biraben, Hyperfine Interact. **228**, 159 (2014).

[56] O. A. Fojón, R. D. Rivarola, R. Gayet, J. Hanssen, and P. A. Hervieux, J. Phys. B: At. Mol. Opt. Phys. **30**, 2199 (1997).

[57] H. F. Busnengo, A. E. Martínez, and R. D. Rivarola, Phys. Scr. **51**, 190 (1995).

[58] P. A. Macri, J. E. Miraglia, J. Hanssen, O. A. Fojn, and R. D. Rivarola, J. Phys. B: At. Mol. Opt. Phys. **37**, L111 (2004).

[59] P. Macri, Nucl. Instr. and Meth. B **247**, 75 (2006).

[60] L. Jiao, Y. Wang, and Y. Zhou, Phys. Rev. A **84**, 052711 (2011).

[61] L. Jiao, Y. Wang, and Y. Zhou, J. Phys. B: At. Mol. Opt. Phys. **45**, 085204 (2012).

[62] Y. Z. Zhang, R. M. Yu, S. X. Li, X. D. Song, and L. G. Jiao, J. Phys. B: At. Mol. Opt. Phys. **48**, 175206 (2015).

[63] R. Abrines and I. C. Percival, Proc. Cambridge Philos. Soc. **88**, 861 (1966).

[64] R. E. Olson, Phys. Rev. A **24**, 1726 (1981).

[65] E. A. Hessels, D. M. Homan, and M. J. Cavagnero, Phys. Rev. A **57**, 1668 (1998).

[66] I. C. Percival and D. R. Richards, Adv. Atom. Mol. Phys. **11**, 1 (1975).

[67] J. Lu, E. Y. Sidky, Z. Roller-Lutz, and H. O. Lutz, Phys. Rev. A **68**, 024702 (2003).

[68] M. L. Wall, C. S. Norton, and F. Robicheaux, Phys. Rev. A **72**, 052702 (2005).

[69] D. Krasnický, R. Caravita, C. Canali, and G. Testera, Phys. Rev. A **94**, 022714 (2016).

[70] T. C. Naginey, B. B. Pollock, E. W. Stacy, H. R. J. Walters, and C. T. Whelan, Phys. Rev. A **89**, 012708 (2014).

[71] T. C. Naginey, E. W. Stacy, B. B. Pollock, H. R. J. Walters, and C. T. Whelan, Phys. Rev. A **89**, 062704 (2014).

[72] K. Higgins and P. G. Burke, J. Phys. B: At. Mol. Opt. Phys. **24**, L343 (1991).

[73] A. A. Kernoghan, M. T. McAlinden, and H. R. J. Walters, J. Phys. B: At. Mol. Opt. Phys. **28**, 1079 (1995).

[74] K. Ratnavelu, J. Mitroy, and A. T. Stelbovics, J. Phys. B: At. Mol. Opt. Phys. **29**, 2775 (1996).

[75] A. A. Kernoghan, D. J. R. Robinson, M. T. McAlinden, and H. R. J. Walters, J. Phys. B: At. Mol. Opt. Phys. **29**, 2089 (1996).

[76] J. Mitroy, Aust. J. Phys. **46**, 751 (1993).

[77] J. Mitroy and A. T. Stelbovics, Phys. Rev. Lett. **72**, 3495 (1994).

[78] J. Mitroy and A. T. Stelbovics, J. Phys. B: At. Mol. Opt. Phys. **27**, 3257 (1994).

[79] J. Mitroy and K. Ratnavelu, J. Phys. B: At. Mol. Opt. Phys. **28**, 287 (1995).

[80] J. Mitroy, L. Berge, and A. T. Stelbovics, Phys. Rev. Lett. **73**, 2966 (1994).

[81] J. Mitroy, Aust. J. Phys. **48**, 645 (1995).

[82] J. Mitroy, Aust. J. Phys. **48**, 893 (1995).

[83] J. Mitroy, J. Phys. B: At. Mol. Opt. Phys. **29**, L263 (1996).

[84] J. Mitroy, Aust. J. Phys. **49**, 919 (1996).

[85] J. Mitroy and G. Ryzhikh, J. Phys. B: At. Mol. Opt. Phys. **30**, L371 (1997).

[86] J. Mitroy and A. T. Stelbovics, J. Phys. B: At. Mol. Opt. Phys. **27**, L79 (1994).

[87] J. Mitroy, Phys. Rev. A **52**, 2859 (1995).

[88] B. H. Bransden and C. J. Noble, J. Phys. B: At. Mol. Opt. Phys. **32**, 1305 (1999).

[89] B. H. Bransden, C. J. Noble, and R. J. Whitehead, J. Phys. B: At. Mol. Opt. Phys. **34**, 2267 (2001).

[90] J. Macek, J. Phys. B: At. Mol. Opt. Phys. **1**, 831 (1968).

[91] B. J. Archer, G. A. Parker, and R. T. Pack, Phys. Rev. A **41**, 1303 (1990).

[92] A. Igarashi and N. Toshima, Phys. Rev. A **50**, 232 (1994).

[93] Y. Zhou and C. D. Lin, J. Phys. B: At. Mol. Opt. Phys. **27**, 5065 (1994).

[94] Y. Zhou and C. D. Lin, J. Phys. B: At. Mol. Opt. Phys. **28**, 4907 (1995).

[95] A. Igarashi, N. Toshima, and T. Shirai, J. Phys. B: At. Mol. Opt. Phys. **27**, L497 (1994).

[96] A. Igarashi and I. Shimamura, Phys. Rev. A **56**, 4733 (1997).

[97] A. Igarashi and I. Shimamura, Phys. Rev. A **70**, 012706 (2004).

[98] L. D. Faddeev and S. P. Merkuriev, *Quantum Scattering Theory for Several Particle Systems* (Kluwer Academic Publishers, Dordrecht, 1993).

[99] A. A. Kvitsinsky, A. Wu, and C. Y. Hu, J. Phys. B: At. Mol. Opt. Phys. **28**, 275 (1995).

[100] C.-Y. Hu, J. Phys. B: At. Mol. Opt. Phys. **32**, 3077 (1999).

[101] C.-Y. Hu, D. Caballero, and Z. Hlousek, J. Phys. B: At. Mol. Opt. Phys. **34**, 331 (2001).

[102] C.-Y. Hu and D. Caballero, J. Phys. B: At. Mol. Opt. Phys. **35**, 3879 (2002).

[103] C. Bottcher, J. Phys. B: At. Mol. Phys. **14**, L349 (1981).

[104] N. Yamanaka and Y. Kino, Phys. Rev. A **64**, 042715 (2001).

[105] D. R. Plante and M. S. Pindzola, Phys. Rev. A **57**, 1038 (1998).

[106] N. Yamanaka and Y. Kino, Phys. Rev. A **65**, 062709 (2002).

[107] N. Yamanaka and Y. Kino, Nucl. Instr. and Meth. B **214**, 40 (2004).

[108] I. Bray and A. T. Stelbovics, Phys. Rev. A **46**, 6995 (1992).

[109] A. S. Kadyrov and I. Bray, Phys. Rev. A **66**, 012710 (2002).

[110] A. S. Kadyrov, A. V. Lugovskoy, R. Utamuratov, and I. Bray, Phys. Rev. A **87**, 060701 (2013).

[111] E. P. Wigner, Phys. Rev. **73**, 1002 (1948).

[112] R. Utamuratov, A. S. Kadyrov, D. V. Fursa, and I. Bray, J. Phys. B: At. Mol. Opt. Phys. **43**, 031001 (2010).

[113] R. Utamuratov, A. S. Kadyrov, D. V. Fursa, I. Bray, and A. T. Stelbovics, J. Phys. B: At. Mol. Opt. Phys. **43**, 125203 (2010).

[114] R. Utamuratov, A. S. Kadyrov, D. V. Fursa, I. Bray, and A. T. Stelbovics, Phys. Rev. A **82**, 042705 (2010).

[115] R. Utamuratov, D. V. Fursa, A. S. Kadyrov, A. V. Lugovskoy, J. S. Savage, and I. Bray, Phys. Rev. A **86**, 062702 (2012).

[116] A. V. Lugovskoy, A. S. Kadyrov, I. Bray, and A. T. Stelbovics, Phys. Rev. A **82**, 062708 (2010).

[117] A. V. Lugovskoy, A. S. Kadyrov, I. Bray, and A. T. Stelbovics, Phys. Rev. A **85**, 034701 (2012).

[118] A. V. Lugovskoy, R. Utamuratov, A. S. Kadyrov, A. T. Stelbovics, and I. Bray, Phys. Rev. A **87**, 042708 (2013).

[119] R. Utamuratov, A. S. Kadyrov, D. V. Fursa, M. C. Zammit, and I. Bray, Phys. Rev. A **92**, 032707 (2015).

[120] A. S. Kadyrov and I. Bray, J. Phys. B: At. Mol. Opt. Phys. **49**, 222002 (2016).

[121] I. Bray, I. E. McCarthy, J. Wigley, and A. T. Stelbovics, J. Phys. B: At. Mol. Opt. Phys. **26**, L831 (1993).

[122] I. Bray, Phys. Rev. A **49**, 1066 (1994).

[123] C. M. Rawlins, A. S. Kadyrov, and I. Bray, Phys. Rev. A **97**, 012707 (2018).

[124] A. S. Kadyrov, I. Bray, A. M. Mukhamedzhanov, and A. T. Stelbovics, Phys. Rev. A **72**, 032712 (2005).

[125] V. Eremenko, N. Upadhyay, I. Thompson, C. Elster, F. Nunes, G. Arbanas, J. Escher, and L. Hlophe, Comp. Phys. Comm. **187**, 195 (2015).

[126] A. W. Bray, I. B. Abdurakhmanov, A. S. Kadyrov, D. V. Fursa, and I. Bray, Comp. Phys. Comm. **203**, 147 (2016).

[127] A. W. Bray, I. B. Abdurakhmanov, A. S. Kadyrov, D. V. Fursa, and I. Bray, Comp. Phys. Comm. **212**, 55 (2017).

[128] I. I. Fabrikant, J. Phys. B: At. Mol. Phys. **7**, L259 (1974).

[129] H. R. Sadeghpour, J. L. Bohn, M. J. Cavagnero, B. D. Esry, I. I. Fabrikant, J. H. Macek, and A. R. P. Rau, J. Phys. B: At. Mol. Opt. Phys. **33**, R93 (2000).

[130] A. S. Kadyrov, C. M. Rawlins, A. T. Stelbovics, I. Bray, and M. Charlton, Phys. Rev. Lett. **114**, 183201 (2015).

[131] C. M. Rawlins, A. S. Kadyrov, A. T. Stelbovics, I. Bray, and M. Charlton, Phys. Rev. A **93**, 012709 (2016).

[132] A. S. Kadyrov, I. Bray, M. Charlton, and I. I. Fabrikant, Nature Commun. **8**, 1544 (2017).

[133] A. S. Kadyrov, C. M. Rawlins, M. Charlton, I. I. Fabrikant, and I. Bray, Hyperfine Interact. **239**, 42 (2018).

[134] J. W. Humberston, P. V. Reeth, M. S. T. Watts, and W. E. Meyerhof, J. Phys. B: At. Mol. Opt. Phys. **30**, 2477 (1997).

[135] J. P. Merrison, H. Bluhme, J. Chevallier, B. I. Deutch, P. Hvelplund, L. V. Jørgensen, H. Knudsen, M. R. Poulsen, and M. Charlton, Phys. Rev. Lett. **78**, 2728 (1997).

[136] I. I. Fabrikant, A. W. Bray, A. S. Kadyrov, and I. Bray, Phys. Rev. A **94**, 012701 (2016).

[137] A. K. Kazansky and V. N. Ostrovsky, Phys. Rev. Lett. **77**, 3094 (1996).

[138] M. Charlton, A. S. Kadyrov, and I. Bray, Phys. Rev. A **94**, 032701 (2016).

[139] E. A. Hessels, D. M. Homan, and M. J. Cavagnero, Phys. Rev. A **57**, 1668 (1998).

[140] I. Bray, J. J. Bailey, D. V. Fursa, A. S. Kadyrov, and R. Utamuratov, Eur. Phys. J. D **70**, 6 (2016).

[141] I. Bray, J. Phys. B: At. Mol. Opt. Phys. **28**, L247 (1995).

[142] C. M. Rawlins, A. S. Kadyrov, and I. Bray, Eur. Phys. J. D **72**, 77 (2018).